Dissertation

submitted to the

Combined Faculties for the Natural Sciences and for Mathematics

of the Ruperto-Carola University of Heidelberg, Germany

for the degree of

Doctor of Natural Sciences

put forward by

Ferdinand Zimmermann, M. Sc.

born in Dresden, Germany

Oral examination: June 19, 2019

Relaxation-Compensated Amide Chemical Exchange Saturation Transfer MRI of the Human Breast

Referees: Prof. Dr. Peter Bachert

Prof. Dr. Lothar Schad

Relaxation-Compensated Amide Chemical Exchange Saturation Transfer MRI of the Human Breast:

Early detection of breast cancer is associated with reduced mortality. As an adjunct to X-ray mammography, magnetic resonance imaging (MRI) is used for clarification of suspicious lesions. Beyond conventionally applied MRI modalities, chemical exchange saturation transfer (CEST) MRI has the potential to provide insights on biochemical tumor environment. Particularly the amide CEST signal originating from proteins has been shown to correlate with parameters of high clinical relevance. However, in the breast, the amide CEST signal is compromised by fat-signal-induced artifacts. Moreover, a profound interpretation requires an isolation of superimposing CEST signals and correction for water relaxation properties.
The aim of this thesis was to account for these factors and to enable relaxation-compensated amide CEST MRI of the human breast. A general theoretical description allowed the correction for fat-signal-induced artifacts by a novel post-processing algorithm. In addition, established methods for mapping of water relaxation properties were enhanced for a robust performance in the presence of fat. This enabled – for the first time – examinations of breast cancer patients using relaxation-compensated amide CEST MRI. In three patients a significant increase of the amide CEST contrast was observed compared to healthy volunteers. Hormonal-induced fluctuations in the amide CEST contrast were shown to be negligible.

Relaxationskorrigierte Amid-CEST-MRT der menschlichen Brust:

Frühzeitige Erkennung von Brustkrebs wird mit einer verringerten Mortalität in Verbindung gebracht. Zusätzlich zur Röntgenmammographie kann die Magnetresonanztomographie (MRT) zur Abklärung von verdächtigen Läsionen zu Rate gezogen werden. Neben den konventionellen MRT-Modalitäten bietet die auf chemischen Austausch (CEST) basierende MRT die Möglichkeit, Einblick in biochemische Eigenschaften der Tumore zu erhalten. Insbesondere korreliert das CEST-Signal von Amid-Protonen aus Proteinen mit klinisch wertvollen Gewebsparametern. Die Anwendung in der Brust ist jedoch von fettsignalinduzierten Störeinflüssen beeinträchtigt. Des Weiteren bedarf eine fundierte Dateninterpretation einer Isolierung von sich überlagernden CEST-Signalen sowie einer Korrektur für die Relaxationseigenschaften des Wassers.
Das Ziel dieser Arbeit war die Berücksichtigung dieser Störeinflüsse, um eine relaxationskorrigierte Amid-CEST-MR-Aufnahme der weiblichen Brust zu ermöglichen. Eine allgemeine Herleitung ermöglichte die Korrektur der fettsignalinduzierten Artefakte mittels eines eigen entwickelten Postprocessing-Algorithmus. Bereits etablierte Methoden zur Bestimmung der Wasserrelaxationseigenschaften wurden erweitert, um deren robuste Funktionsweise trotz Anwesenheit des Fetts in der Brust sicherzustellen. In Summe ermöglichte dies erstmalig die Untersuchung von Brustkrebspatientinnen mittels relaxationskorrigierter Amid-CEST-MR-Mammographie. Verglichen mit gesunden Probandinnen wies der Amid-Kontrast eine deutliche Erhöhung bei drei untersuchten Patientinnen auf. Es konnte gezeigt werden, dass hormonell bedingte Schwankungen des Amid-Kontrasts minimal und vernachlässigbar sind.

Contents

List of Abbreviations

ADC	apparent diffusion coefficient
APT	amide proton transfer
AREX	apparent exchange-dependent relaxation
BW	bandwidth
CE	chemical exchange
CEST	chemical exchange saturation transfer
cw	continuous wave
DC	duty cycle
DCE	dynamic contrast-enhanced
DICOM	Digital Imaging and Communications in Medicine
DKFZ	German Cancer Research Center
DS	direct water saturation
DWI	diffusion-weighted imaging
FF	fat fraction
FID	free induction decay
FoV	field of view
FSH	follicle stimulating hormone
FWHM	full width at half maximum
GRE	gradient echo
LH	luteinizing hormone
LS	large shift limit
MR	magnetic resonance
MRI	magnetic resonance imaging
MT	magnetization transfer
MTR	magnetization transfer ratio
NMR	nuclear magnetic resonance
NOE	nuclear Overhauser effect
nWM	normal appearing white matter
P	patient
PBS	phosphate buffered solution
PTE	proton transfer ratio
rNOE	exchange-relayed NOE
ROI	region of interest

SAR	specific absorption ratio
SNR	signal to noise ratio
SOS	sum-of-squares
T1	longitudinal relaxation time of water
TE	echo time
TMS	tetramethylsilane
TR	repetition time
TSE	turbo spin echo
V	volunteer
WASABI	water shift and B1
Z	Z-spectrum

1 | Introduction

Breast cancer is the most common cancer in women, with around 70,000 incidences each year in Germany [1]. Screening X-ray mammography has been associated with a reduced mortality due to early detection [2], but is not suitable for women with an increased cancer risk or extremely dense breasts [3]. Mammography by means of magnetic resonance imaging (MRI) presents an adjunct screening modality [3]. The soft tissue contrast of conventional MRI is insufficient for lesion detection and requires uptake dynamics by means of gadolinium-based contrast agents to be of diagnostic value. Dynamic-contrast-enhanced (DCE) MRI presents the current standard alternative to X-ray mammography and can support clarification of suspicious lesions [3, 4]. However, DCE MRI of the breast provides only modest specificity in clinical practice, despite the additional information associated with tissue perfusion properties [5]. Recently, completely non-invasive alternatives for breast MRI gained popularity. One of those is diffusion weighted imaging (DWI) which is increasingly being incorporated into clinical routine despite certain limitations [5]. DWI supports tumor detection in the breast by detecting the biophysical characteristics of tissue water and thus, yields information on the cellular environment [5–7]. Another alternative modality that probes the biochemical environment is given by chemical exchange saturation transfer (CEST) MRI [8]. CEST MRI indirectly detects protons loosely bound in endogenous low concentrated biomolecules undergoing chemical exchange with water. In particular, CEST signals originating from amide resonances of the peptide bonds in the backbone of mobile proteins are related to protein concentration and conformation, which are known to be altered in tumors [9, 10]. Additionally, amide CEST MRI has been shown to correlate with biomarkers in human brain tumors [11] and can be associated with survival in high-grade glioma patients [12]. For these reasons, the application of CEST MRI as a diagnostic tool for mamma carcinoma patients is promising.

Conventional CEST MRI of the human breast was first performed by Schmitt *et al.* [13]. Since then, several studies correlated the amide CEST signal to an early treatment response during neoadjuvant chemotherapy [14] and found correlations to tumor aggressiveness [15]. However, these studies did not account for water relaxation properties (i.e. T_1 and T_2), which were shown to influence observed CEST effects [16]. Moreover, multiple CEST signals were shown to superimpose, thus requiring the isolation and a compensation for relaxation times [17] to enable a profound interpretation. Relaxation-compensated and isolated CEST contrasts are dependent on the saturation amplitude in the CEST experiment and are for that reason affected by field inhomogeneities present in breast MRI [18, 19]. Foremost, CEST MRI of the breast is compromised by fat-signal-induced artifacts [15, 20]. These fat artifacts depend on imaging parameters, in particular the echo time (TE).

The aim of this thesis was to account for these challenges to enable relaxation-compensated amide CEST MRI of the human breast. A general theoretical description was derived explaining the interplay of water and fat signals during a CEST experiment for arbitrary TE, and thus, the

origin of these artifacts. This allowed the correction of CEST data for fat signals by a novel normalization algorithm based on data postprocessing. Established fitting routines were adapted to isolate amide CEST signals and to compensate for T_2 relaxation [16]. A self-developed fat saturation presented an improvement for field and T_1 mapping and allowed for a robust quantification. Together, this enabled — for the first time — examinations of mamma carcinoma patients using relaxation-compensated amide CEST MRI. The analysis of three patients of an ongoing clinical pilot study is included in this thesis. A significant increase of the amide CEST contrast was observed compared to healthy volunteers. Potential hormonal-induced changes of the contrast during menstrual cycle were investigated in healthy premenopausal women. The observed fluctuations were minimal and, with respect to tumor imaging, negligible.

The origin of nuclear magnetic resonance and the basics of MRI are explained in Chapter 2. Furthermore, information about the anatomy and physiology of the human female breast is provided. Chapter 3 introduces the fundamentals of chemical exchange from a physical point of view and describes the CEST experiment. In Chapter 4, a general formulation of water and fat signals during a CEST experiment is derived. Also, the novel normalization is defined and challenges of relaxation-compensated CEST MRI of the breast are outlined. Methods and methodological developments are described in Chapter 5. The advanced *in vivo* examination protocol as well as the post-processing workflow are provided. The obtained results (Ch. 6) are discussed in Chapter 7. Finally, a summary is given in Chapter 8.

2 | Physical and anatomical basics

The fundamental theory of nuclear magnetic resonance (NMR) is briefly described in the following sections as well as some principles used in magnetic resonance imaging (MRI). For more details, the reader is referred to standard literature of NMR physics, for instance textbooks [21], [22] and [23]. Subsequently, a brief overview on the anatomy of the human breast is presented.

2.1 Nuclear spins in a magnetic field

Every atomic nucleus consists of protons and neutrons. Protons and neutrons are fermions with a spin of one half. The nucleus of hydrogen consists only of one proton (^{1}H). Its nuclear spin $\vec{I}$ is therefore 1/2, obeying the algebra of quantum mechanical angular momentum. The commutator relations of the nuclear spin operator $\hat{\vec{I}} = (\hat{I}_x, \hat{I}_y, \hat{I}_z)$ are:

$$[\hat{I}_k, \hat{I}_l] = i\hbar\, \epsilon_{klm} \hat{I}_m \tag{2.1}$$

$$[\hat{\vec{I}}^{\,2},\ \hat{I}_k] = 0 \tag{2.2}$$

with the Levi-Civita symbol ϵ_{klm} and $k, l, m \in \{x, y, z\}$. The eigenstates of the commuting operator $\hat{\vec{I}}^{\,2}$ and $\hat{I}_z$ are the angular momentum quantum number I and the magnetic quantum number $m = (-I, -I+1, ..., I-1, I)$:

$$\hat{\vec{I}}^{\,2} \,|I, m\rangle = \hbar^2 I(I+1)\,|I, m\rangle \tag{2.3}$$

$$\hat{I}_z \,|I, m\rangle = \hbar m \,|I, m\rangle \tag{2.4}$$

with $\Delta m = 1$. A magnetic moment $\hat{\vec{\mu}}$ is associated with the nuclear spin:

$$\hat{\vec{\mu}} = \gamma \hat{\vec{I}} \tag{2.5}$$

where γ is nucleus specific gyromagnetic ratio. For hydrogen, the gyromagnetic ratio was experimentally determined to $\gamma = 2.675 \cdot 10^8 \,\frac{\text{rad}}{\text{s} \cdot \text{T}}$, $\frac{\gamma}{2\pi} = 42.576 \,\frac{\text{MHz}}{\text{T}}$. If an external magnetic field $\vec{B} = (0, 0, B_0)$ is applied, the magnetic moment can be described by the Hamiltonian:

$$\hat{H} = -\hat{\vec{\mu}} \cdot \vec{B} = -\hat{\mu}_z \cdot B_0 = -\gamma \hat{I}_z \cdot B_0 \tag{2.6}$$

The Hamiltonian and the angular momentum are linear, hence their commutator relations are: $\left[\hat{\vec{I}}^{\,2}, \hat{H}\right] = 0$ and $\left[\hat{I}_z, \hat{H}\right] = 0$. Therefore, the eigenstates $|I, m\rangle$ of the nuclear spin are also eigenstates of $\hat{H}$. One can formulate the *time-independent Schrödinger equation* for static magnetic fields:

$$\hat{H}\,|I, m\rangle = E_m\,|I, m\rangle = -\gamma m \hbar B_0\,|I, m\rangle \tag{2.7}$$

This leads to the Zeeman effect [24]: a discrete splitting into $2I+1$ equidistant energy levels due to the different magnetic quantum numbers m. The transition between these energy levels is accompanied by the emission or absorption of a photon of discrete energy. For the proton of spin 1/2, the energy difference of the two possible eigenstates $|\alpha\rangle = \left|\frac{1}{2}, -\frac{1}{2}\right\rangle$ and $|\beta\rangle = \left|\frac{1}{2}, +\frac{1}{2}\right\rangle$ is (Fig. 2.1):

$$\Delta E = E_\alpha - E_\beta = \hbar\gamma B_0 = \hbar\omega_0 \tag{2.8}$$

with $\omega_0 = \gamma B_0$ being the *Larmor frequency*. In case of a static magnetic field of $\mathrm{B}_0 = 7\,\mathrm{T}$, the Larmor frequency is $\omega_0/(2\pi) \approx 298\,\mathrm{MHz}$ for protons. In case of irradiation with time-varying magnetic fields of the radial frequency ω_0, the resonance causes a depopulation of $|\beta\rangle$ and a population gain of $|\alpha\rangle$.

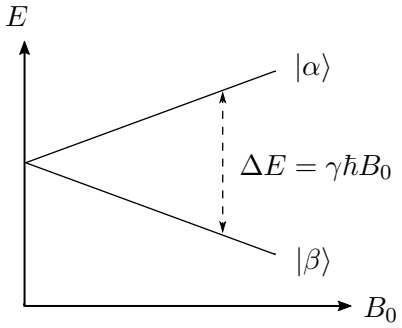

Figure 2.1: Zeeman splitting of energy levels for a nucleus of spin quantum number $I = 1/2$ as a function of B_0. The energy difference between the two states $|\alpha\rangle$ and $|\beta\rangle$ is $\Delta E = \gamma\hbar\, B_0$.

2.2 Macroscopic Magnetization

In order to perform an NMR experiment, one has to transfer the description of singular spins to a spin ensemble. In case of a macroscopic volume with a fixed number of nuclei that are in thermal equilibrium, one can describe the population probability $p(E_m)$ by the *Boltzmann statistic*:

$$p(E_m) = \frac{1}{Z} e^{-\frac{E_m}{k_B T}} \tag{2.9}$$

with the canonical number of states $Z = \sum_{m=-I}^{I} e^{-\frac{E_m}{k_B T}}$, the Boltzmann constant k_B and T being the equilibrium temperature. As shown in the previous Section 2.1, the proton with spin $I = 1/2$ only has two energy states $|\alpha\rangle$ and $|\beta\rangle$. For such a two-level system, the expectation value of the z-component of the magnetic moment is given by:

$$\langle\hat{\mu}_z\rangle = \gamma\langle\hat{I}_z\rangle = \gamma\left(p_{-\frac{1}{2}}\langle\alpha|\hat{I}_z|\alpha\rangle + p_{+\frac{1}{2}}\langle\beta|\hat{I}_z|\beta\rangle\right) \tag{2.10}$$

$$= \frac{1}{2}\gamma\hbar\cdot(p_{+\frac{1}{2}} - p_{-\frac{1}{2}}) = \frac{1}{2}\gamma\hbar\cdot P \tag{2.11}$$

where the difference between the two probabilities P, is also known as the polarization and represents the normalized difference in population:

$$P = p_{+\frac{1}{2}} - p_{-\frac{1}{2}} = \frac{\Delta N}{N} \tag{2.12}$$

By inserting the energy eigenvalues ($E_m = -\gamma\hbar m B_0$, Eq. 2.7) into the population probability (Eq. 2.9), the polarization becomes:

$$P = \frac{e^{\frac{\gamma\hbar B_0}{2k_B T}} - e^{-\frac{\gamma\hbar B_0}{2k_B T}}}{e^{\frac{\gamma\hbar B_0}{2k_B T}} + e^{-\frac{\gamma\hbar B_0}{2k_B T}}} = \tanh\left(\frac{\gamma\hbar B_0}{2k_B T}\right) \tag{2.13}$$

Since $\gamma\hbar B_0 \ll k_B T$ at room temperature, a Taylor expansion of the polarization yields $P \approx \frac{\gamma\hbar B_0}{2k_B T}$. With $k_B = 1.381 \cdot 10^{-23}\,\frac{\mathrm{J}}{\mathrm{K}}$ and $\hbar = 1.055 \cdot 10^{-34}\,\mathrm{J \cdot s}$, the polarization in an ensemble of protons is $P \approx 2.4 \cdot 10^{-5}$ for room temperature and $B_0 = 7\,\mathrm{T}$. The macroscopic magnetization of the spin ensemble is yielded by summing up all N magnetic moments in the volume V:

$$\vec{M} = \frac{N}{V}\langle\hat{\vec{\mu}}\rangle = \frac{1}{2}\gamma\hbar\frac{N}{V}\vec{P} \approx \frac{1}{4}\frac{N}{V}\frac{\gamma^2\hbar^2}{k_B T}\vec{B} \tag{2.14}$$

A detectable magnetization is only present at room temperature due to the large abundance of protons per volume (for water $\approx 6.6 \cdot 10^{19}\,\frac{1}{\mathrm{mm}^3}$).

2.2.1 Time evolution of the magnetization

The *time-dependent Schrödinger equation* can be used to describe a spin in a time-dependent magnetic field:

$$i\hbar\frac{\partial}{\partial t}|I,m\rangle = \hat{H}(t)|I,m\rangle \tag{2.15}$$

with $\hat{H}(t) = -\hat{\vec{\mu}} \cdot \vec{B}(t)$ being the time-dependent Hamiltonian. The *Ehrenfest theorem* [25] can be applied to calculate the time dependence of the expectation value of the magnetic moment $\hat{\vec{\mu}}$:

$$\frac{d}{dt}\langle\hat{\vec{\mu}}\rangle = \frac{i}{\hbar}\langle\left[\hat{H},\hat{\vec{\mu}}\right]\rangle + \langle\frac{\partial\hat{\vec{\mu}}}{\partial t}\rangle \tag{2.16}$$

Application of the commutator relations from Equation 2.2 gives:

$$\frac{d}{dt}\langle\hat{\vec{\mu}}\rangle = \langle\hat{\vec{\mu}}\rangle \times \gamma\vec{B}(t) \tag{2.17}$$

A transition from a quantum mechanical description of $\langle\hat{\vec{\mu}}\rangle$ to a classical description of the macroscopic magnetization $\vec{M}$ is justified by the *correspondence principle* [26] and the large abundance of protons per volume. The time-dependent expectation value of $\vec{M}$ becomes:

$$\frac{d}{dt}\vec{M} = \vec{M}(t) \times \gamma\vec{B}(t) \tag{2.18}$$

Without loss of generality, the static magnetic field $\vec{B}_0 = (0,0,B_0)$ in z-direction is superposed by an oscillating radio frequency (RF) field $\vec{B}_1$ in the xy-plane at frequency ω_{RF}. This leads to the time dependent magnetic field:

$$\vec{B}(t) = \vec{B}_0 + \vec{B}_1(t) = \begin{pmatrix}0\\0\\B_0\end{pmatrix} + B_1\begin{pmatrix}\cos(\omega_{RF}t)\\\sin(\omega_{RF}t)\\0\end{pmatrix} \tag{2.19}$$

A description of $\frac{d}{dt}\vec{M}$ can be simplified by a transformation into a *rotating frame* of reference $(x', y', z' = z)$. If this reference frame rotates at ω_{RF}, both $\vec{B}_0$ and $\vec{B}_1$ are static. Furthermore, $\vec{B}_1$ is aligned in x'-direction, yielding:

$$\frac{d}{dt}\vec{M}'(t) = \vec{M}'(t) \times \gamma\vec{B}_{eff} \tag{2.20}$$

with the effective magnetic field $\vec{B}_{eff}$:

$$\vec{B}_{eff} = \begin{pmatrix} B_1 \\ 0 \\ B_0 - \frac{\omega_{RF}}{\gamma} \end{pmatrix} \tag{2.21}$$

The z-component of $\vec{B}_{eff}$ vanishes, if the system is in resonance and $\omega_{RF} = \omega_0 = \gamma B_0$. Then, the external magnetic field only affects the magnetization $\vec{M}$ in x'-direction, which performs a precession in the y'-z-plane with the frequency $\omega_1 = \gamma B_1$. From the laboratory perspective, the $\vec{B}_1(t)$ field induces a spiral flip of $\vec{M}$. The *flip angle* α describing the angle between the magnetization and the z-axis depends on the duration t_p of irradiation:

$$\alpha = \int_0^{t_p} \omega_1(t)dt = \int_0^{t_p} \gamma B_1(t)dt \tag{2.22}$$

If the RF irradiation is switched off, the magnetization $\vec{M}$ precesses in the xy-plane with the Larmor frequency ω_0 and returns back to the thermal equilibrium.

2.2.2 Bloch equations

The prepared magnetization represents an excited state. Over time, the excitation decays due to the interactions of the nuclei with their environment, described by the *spin-lattice* relaxation time T_1. Additionally, the spin system gradually looses its phase coherence, which is characterized by the *spin-spin* relaxation time T_2. The equation 2.20 was expanded by Felix Bloch [27] with the following, phenomenological relaxation terms:

$$\frac{d}{dt}M_{x'} = \gamma(\vec{M} \times \vec{B})_{x'} - \frac{M_{x'}}{T_2} \tag{2.23}$$

$$\frac{d}{dt}M_{y'} = \gamma(\vec{M} \times \vec{B})_{y'} - \frac{M_{y'}}{T_2} \tag{2.24}$$

$$\frac{d}{dt}M_z = \gamma(\vec{M} \times \vec{B})_z - \frac{M_z - M_0}{T_1} \tag{2.25}$$

Next to the intrinsic T_2 relaxation, the spins are additionally dephased by local field inhomogeneities of the static field B_0. The apparent relaxation T_2^* is:

$$\frac{1}{T_2^*} = \frac{1}{T_2} + \frac{1}{T_2'} \tag{2.26}$$

with the term $T_2' = \gamma \Delta B_0$ describing the dephasing due to field inhomogeneities $\Delta \mathrm{B}_0$.

2.2.3 The NMR signal

By defining the longitudinal part of the Bloch-equations (2.23-2.25) as $M_\parallel = M_z$ and the transverse component $M_\perp = M_x + iM_y$, one can formulate the relaxation processes of the magnetization as:

$$M_\perp(t) = M_{0,\perp} \cdot e^{-\frac{t}{T_2^*}} \tag{2.27}$$

$$M_\parallel(t) = M_0 - \left(M_0 - M_\parallel(0)\right) e^{-\frac{t}{T_1}} \tag{2.28}$$

with M_0 being the magnitude of the initial magnetization $\vec{M}$ in thermal equilibrium (i.e. "fully relaxed"). The rotating perpendicular magnetization $M_\perp(t)$ creates a time-dependent magnetic

flux in the xy-plane. If a receive coil is placed around it, $M_\perp(t)$ induces a voltage $U_{ind}(t)$. This voltage is the actually measurable NMR signal. With $\rho(\vec{r})$ being the spatial distribution of nuclear spins, the NMR signal of a volume V is:

$$S(t) = U_{ind} \propto \int \rho(\vec{r}) \cdot e^{i\omega_0 t} dV \tag{2.29}$$

Due to the transversal T_2^* relaxation, the measured NMR signal decays exponentially, which is known as the *free induction decay* (FID):

$$S(t) = A_0 \cdot e^{i\omega_0 t} e^{-\frac{t}{T_2^*}} \tag{2.30}$$

The Fourier transformation (FT) of the FID yields a Lorentzian line function in the frequency domain. Its full width at half maximum (FWHM) is $\Gamma = 2/T_2^*$. The detected FID and the Fourier transform is illustrated in Figure 2.2.

As depicted in Figure 2.3, the dephasing due to local field inhomogeneities ΔB_0 can be reversed. A 180° pulse played out after the time $t = \mathrm{TE}/2$ will result in a *spin echo* reaching its maximum amplitude at $t = \mathrm{TE}$. TE is the so called *echo time*.

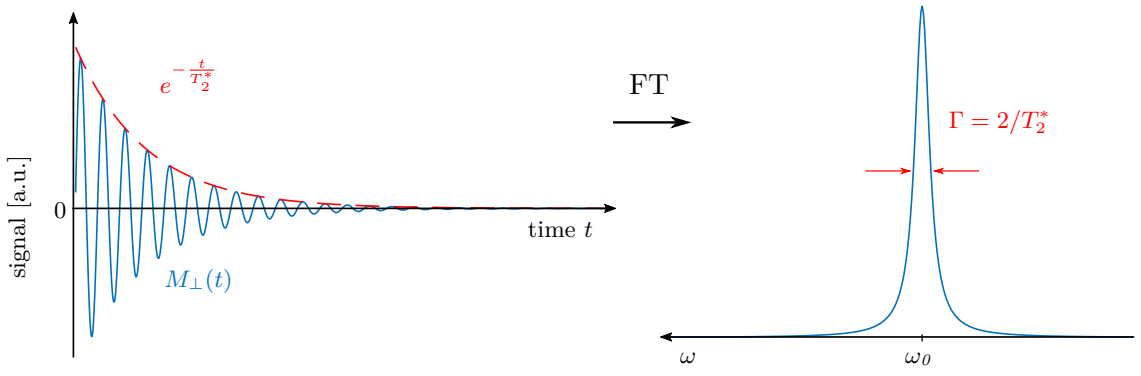

Figure 2.2: The NMR signal decays exponentially due to T_2^* relaxation. The Fourier transform (FT) of the free induction decay (FID, on the left) yields a Lorentzian lineshape at the frequency offset ω_0 (right).

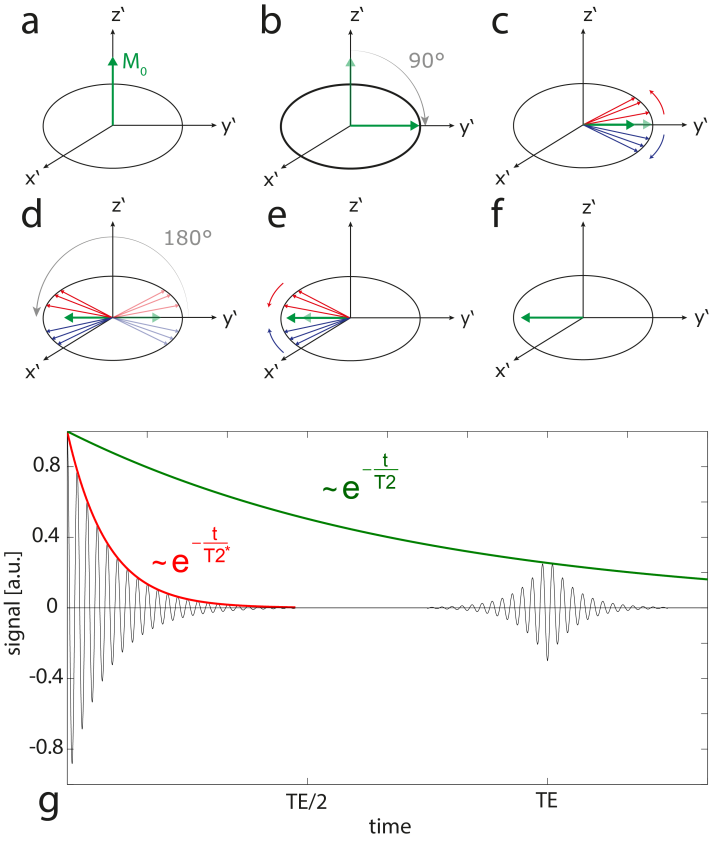

Figure 2.3: Spin echo in the rotating frame. (a) The equilibrium magnetization is aligned to z-direction. (b) A 90° pulse flips the magnetization in the xy-plane. (c) Dephasing and loss of coherence of the spin packages decreases the magnetization. (d) A 180° pulse inverts the magnetization in the xy-plane. (e) Rephasing of spin packages leads to a build up of the spin echo. (f) Spin echo reaches its maximum amplitude at t=TE. (g) Time evolution of the signal and spin echo.
Image reproduced with kind permission from Windschuh ([28, p. 7]).

2.3 Chemical shift

Each nucleus is shielded from the static magnetic field B_0 by its surrounding electron cloud. Protons bound in molecules therefore experience a local magnetic field:

$$B_{loc} = B_0 + \Delta B = B_0(1 - \sigma) \tag{2.31}$$

with the dimensionless shielding constant σ. B_{loc} results in a shift of the resonance frequency, $\omega_{loc} = \gamma B_0(1 - \sigma)$. This shift is called *chemical shift* due to its strong dependence on the chemical environment. A field strength independent representation of the chemical shift is given by a frequency ratio in parts per million (ppm):

$$\delta = \frac{\omega - \omega_{ref}}{\omega_{ref}} \cdot 10^6 \tag{2.32}$$

with the reference frequency ω_{ref}. Usually, tetramethylsilane (TMS) is used in MR spectroscopy as a reference substance for protons. However, in CEST experiments the reference frequency is set to free water, which has a chemical shift of about 4.7 ppm with respect to TMS [22] (i.e. $\delta_{water} = 0$ ppm). By convention, the direction of the frequency axis is displayed reversely (cf. Fig. 2.2). The lower frequencies are referred as *upfield*, while *downfield* refers to higher frequencies.

2.4 MR imaging

The above descriptions only allow the investigation of a small and homogeneous sample (i.e. single voxel). In order to obtain a spatial encoding, a spatially dependent magnetic field is

required. In magnetic resonance imaging (MRI), this is realized by an additional magnetic gradient field $\vec{G}$:

$$\vec{B}(\vec{x}) = B_0 \cdot \vec{e_z} + (\vec{G} \cdot \vec{x}) \cdot \vec{e_z} \tag{2.33}$$

$$\omega(\vec{r}, t) = \gamma \left(B_0 + \vec{G}(\vec{r}, t) \cdot \vec{e_z} \right) \tag{2.34}$$

where the vector $\vec{x}$ is a point in space. The spin's position, $\vec{r}$, is encoded by their effective resonance frequency (Eq. 2.8). The orientation of the gradient field is aligned parallel to the static magnetic field ($\vec{G} \| \vec{B}_0$) in order to not induce a precession of the spin packages.

2.4.1 k-Space

Due to the gradient field, the NMR signal (Eq. 2.29) in the rotating frame becomes:

$$S(\vec{r}, t) \propto \int \rho(\vec{r}) e^{i\gamma \vec{G}(t)\vec{r}t} d\vec{r} \tag{2.35}$$

The gradient field results in an additional dephasing of the NMR signal. The spatial information of the spins is thereby encoded in an accumulated phase. The zeroth gradient moment is defined as the vector $\vec{k}$:

$$\vec{k} = \frac{\gamma}{2\pi} \int_0^t \vec{G}(\tau) d\tau \tag{2.36}$$

which yields in Equation 2.35:

$$S(\vec{k}(t)) \propto \int \rho(\vec{r}) e^{i\vec{k}(t)\vec{r}} d\vec{r} \tag{2.37}$$

Thereby, the NMR signal $S(\vec{k}(t))$ is linked to the Fourier transformation of the spatial spin distribution $\rho(\vec{r})$:

$$\rho\left(\vec{r}(t)\right) \propto \int S\left(\vec{k}(t)\right) e^{i\vec{k}(t)\vec{r}} d\vec{k} \tag{2.38}$$

2.4.2 Spatial encoding

The k-space represents the spatial frequency domain of an image. The image contrast is stored at the k-space center, whereas information of sharp edges are stored in the periphery. The k-space acquisition is briefly described in the following.

Slice selection

A linear gradient in z-direction $G(z) = G_z \cdot z$ yields the Larmor frequency:

$$\omega_0 = \gamma(B_0 + G_z \cdot z) \tag{2.39}$$

An image slice can then be selected with an RF pulse of bandwidth $\Delta\omega_{RF}$. The use of a sinc pulse results in a rectangular excitation pattern in the frequency domain with a thickness:

$$\Delta z = \frac{\Delta\omega_{RF}}{2\pi\gamma G_z} \tag{2.40}$$

The center frequency of the pulse defines the slice position.

Phase Encoding

The slice selection initiates the precession of spin packages around the z-axis. The phase relation of the spins can locally be changed on the y-axis by another gradient, G_y, which is activated before the signal acquisition. The y-position is then encoded in the phase of the spin packages. Multiple phase encoding steps are required to acquire the full k-space.

Frequency Encoding

A third gradient is applied *during* the actual readout (i.e. when the signal is detected and converted from an analog to digital information). This gradient in x-direction (G_x) encodes the Larmor frequencies of the phase-encoded spin packages. Thereby, a spectrum of frequencies is recorded. These three gradients enable the acquisition of the k-space of one imaged slice.

2.4.3 Gradient echo imaging

Adequate dephasing and rephasing of spin packages by the gradients can generate *gradient echoes*. These echoes can be formed faster than spin echoes and are therefore used for a quick image acquisition. The timing of the gradients in a fast low angle shot (FLASH) sequence is schematically depicted in Figure 2.4. The magnetization is flipped to the y'-axis with short excitation pulses by the flip angle α. One k-space line is then acquired in one iteration of the phase encoding gradient. This period is called repetition time (TR). In order to minimize stimulated echoes negatively affecting the signal acquisition, spoiling gradients are used for dephasing of residual magnetization in the xy-plane.

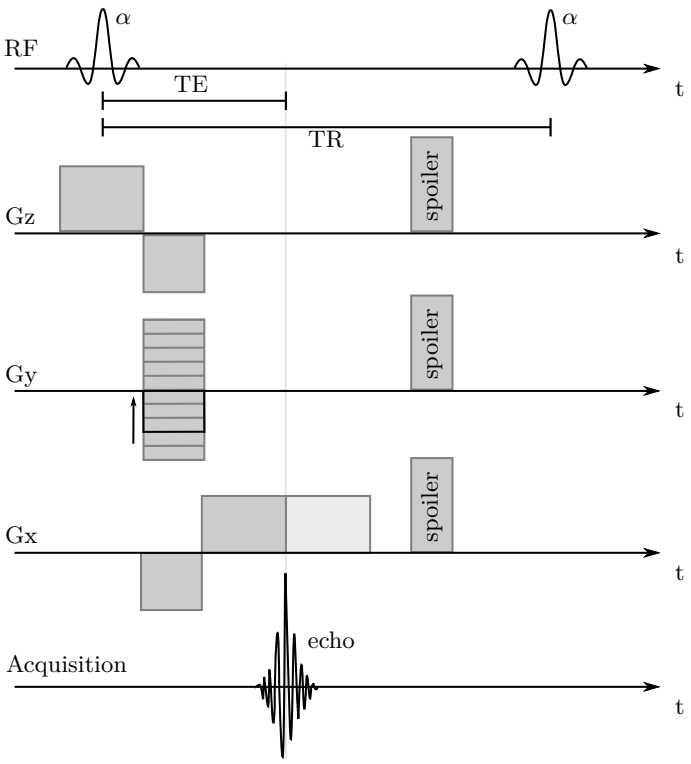

Figure 2.4: Illustration a FLASH (fast low angle shot) gradient echo sequence. Acquisition of the gradient echo at TE enables a short repetition time (TR) and a quick acquisition of the whole k-space. The gradients $G_{x,y,z}$ encode the spatial information (readout, phase encoding and slice selection, respectively).

2.5 Lipids in MRI

The word *fat* is often used for both, the adipose tissue and the chemical component itself. Chemically, fats are long-chain triglyceride molecules consisting of three fatty acid chains. Triglycerides are a subgroup of lipids, which are generally defined as a biomolecule soluble in nonpolar solvents [29]. *Adipose tissue* refers to tissues that mainly store triglycerides in the body. Hydrogen atoms in lipids are nestled within aliphatic side chains among carbon atoms. Due to their different electron shielding, they have a chemical shift with respect to water and contribute to MR signal with different frequencies. Triglycerides are the main source of the signal, while phospholipids in the cell membrane do not effectively contribute due to a very short T_2 relaxation time. Others, e.g. cholesterol esters or free fatty acids have a low abundance *in vivo* [30] .

An exemplary ^{1}H spectrum of fat tissue in the human breast acquired at 7 T is shown in Figure 2.5 [31]. Ten resonances were resolved by means of MR spectroscopy. The different lipid peaks are assigned to their corresponding chemical position in the displayed triglyceride molecule. The resonance of highest amplitude is methylene, i.e. -$(CH_2)_n$- groups, resonating at 1.3 ppm. The chemical shift between water and this main lipid peak is thereby $\delta\omega = -3.4$ ppm. In contrast to water, which is a small and thus fast rotating molecule, triglycerides move slowly. Thereby, T_1 relaxation is more efficient and much shorter than T_1 of water. Reported literature values for relaxation times of human breast tissue obtained at 7 T are listed in Table 2.1.

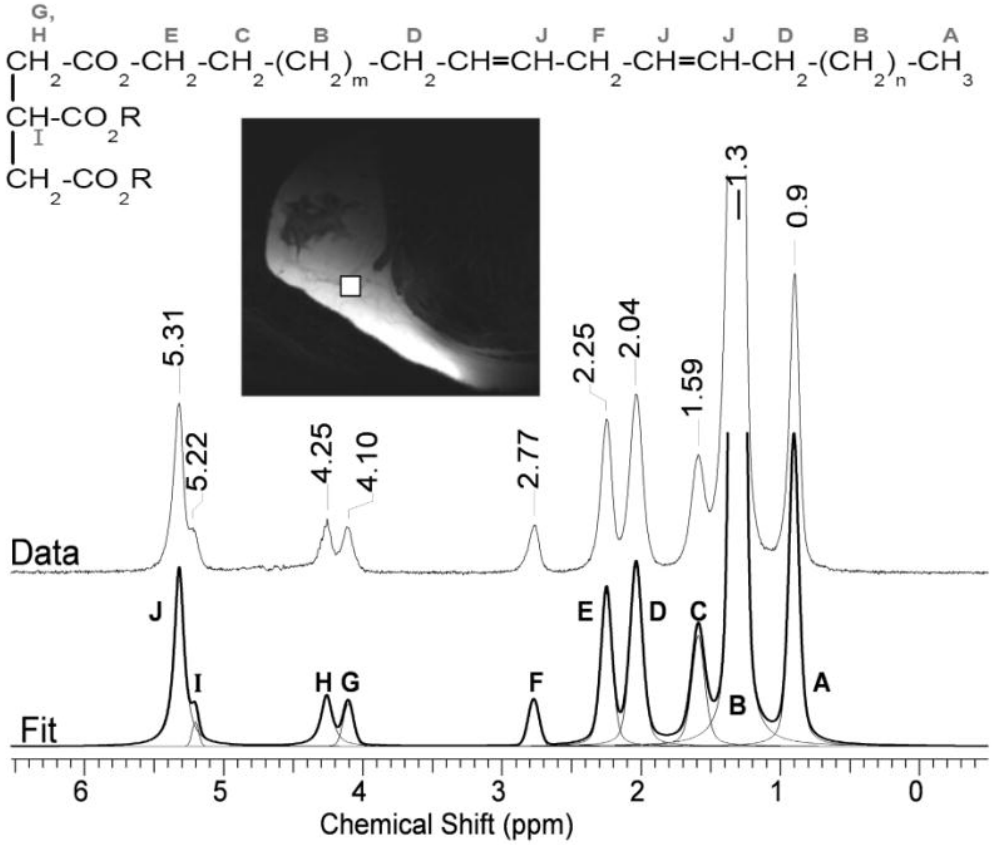

Figure 2.5: Proton spectrum acquired in adipose tissue in a young healthy woman at 7 T. The letter assignment of lipid peaks is also marked on their corresponding position in the triglyceride molecule. Methylene, i.e. -$(CH_2)_n$- groups, resonate at 1.3 ppm and present the main signal source. Image reproduced with written permission from Dimitrov *et al.*, MRM 2012; 67(1):20-26 [31].

Table 2.1: Bibliographical references for relaxation times of water and the main lipid peak (methylene) obtained at 7 T in the human breast. Methylene resonates at 1.3 ppm and contributes the most signal (cf. Fig. 2.5, peak marked with B). The apparent T_2 includes relaxations due to B_0-inhomogeneities but no J-coupling.

	T_1 [ms]	apparent T_2 [ms]	study
water	2265 ± 65	35.5 ± 5.0	Haddadin *et al.*[32]
methylene	549 ± 16	52 ± 17	Dimitrov *et al.* [31]

The effect of lipid signals on MR GRE imaging is presented in the following. Furthermore, the standard approaches to avoid or suppress fat signals in MRI are briefly described.

2.5.1 Chemical shift imaging artifact

In the presence of fat, the slice selection gradient will also act on the lipid resonances. The excitation pulse designed to excite water protons will then additionally excite protons bound in fat but at a different position. The gradient field strength of the slice selection gradient is typically in the order of $G_z \approx 10\,\frac{\mathrm{mT}}{\mathrm{m}}$. With respect to the main lipid peak (i.e. CH_2), the resulting excited slice will be shifted by $\frac{\Delta\omega}{\gamma G_z} \approx 2.4\,\mathrm{mm}$.
As described in the previous sections, all excited protons will begin to precess around the z-axis. Additionally, the frequency encoding gradient during readout causes a mismatch of the acquired fat and water image in frequency encoding direction. The readout bandwidth per pixel BW is directly correlated to the shift Δs by:

$$\Delta s = \frac{\Delta\omega \cdot \gamma B_0}{BW} \tag{2.41}$$

For a readout bandwidth of $300\,\frac{\mathrm{Hz}}{\mathrm{pix}}$ at 7 T, the shift is $\Delta s \approx 3.4\,\mathrm{pix}$.

Echo time dependency

The chemical shift imaging artifact is dependent on the chosen TE. Due to a different chemical shift, lipid signals perform a *phase cycling* of the duration $1/\Delta f$ (Δf is the frequency difference in Hz). Thus, the phase cycling period at 7 T is about 1 ms. This results in a TE-dependent phase relation of water (W) and fat (F) signal and consequently, TE-dependent image intensities. Figure 2.6 shows image intensities acquired for a range of TE in the breast of a healthy woman at 7 T. Periodic changes for over two complete phase cycling periods of water and fat were observed. The special case of a parallel alignment is referred to as *in-phase* ($S_{IP} = W + F$), while the anti-parallel is referred to as *opposed phase* ($S_{OPP} = W - F$).

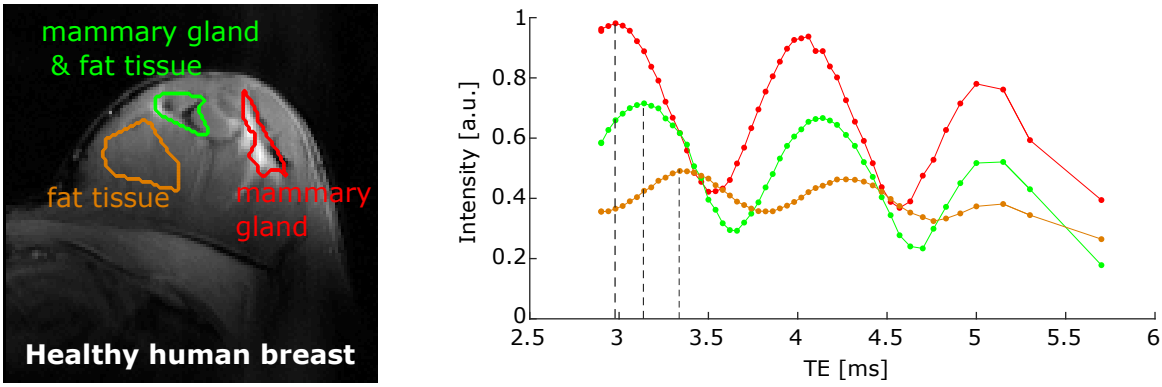

Figure 2.6: Fully relaxed M_0 images as a function of the echo-time TE acquired at B_0=7 T. The phase relation of water and fat is TE-dependent, resulting in periodic changes of the image intensities. The in-phase condition, i.e. the parallel alignment of water and fat in the xy-plane, varies in different regions of interest (marked in the left) due to field inhomogeneities in the breast.

2.5.2 Methods to deal with fat signal

Image interpretation is complicated by the superposition and mismatch of the fat and water signals. Several techniques were developed to compensate for fat signal contributions. Most of them intent to eliminate lipid signals originating from resonances around the main lipid peak, as they make up most of the fat signal. Standard approaches are briefly described in the following. The reader is however advised to consult further literature for an in-depth description.

The standard procedure is to suppress the dominant methylene group by **fat suppression** pulses. Frequency selective pulses are played out prior to the acquisition of the signal and suppress the fat signal. Spoilers are used to dephase the fat [21].

Another approach utilizing the phase cycling differences of water and fat is the **water excitation** [21, 33]. The excitation pulse is replaced by binomial pulses. For example, two appropriately timed and broadband 45° excitation pulses are used. The first one flips both, fat and water. The second pulse is played at an anti-parallel alignment of water and fat. Ideally, fat is flipped back into z-direction and water is flipped into the xy-plane. No dephasing gradients (spoilers) are required for this approach.

The **inversion recovery** approach utilizes the different T_1 relaxation times of water and fat (see Tab. 2.1). A 180° pulse inverts all the proton spins and they begin to recover (cf. Eq. 2.28). The readout is timed to the zero-crossing of the fat signal [34]. However, this method yields a reduced water signal.

The TE-dependent phase relation can be utilized in **Dixon-based water-fat-separation approaches** [35]. In a simplified description, two images have to be acquired, once at an in-phase TE (S_{IP}) and a second one at an opposed-phase TE (S_{OPP}). The water-only and fat-only images can then be calculated by:

$$F = \frac{1}{2} \cdot (S_{IP} - S_{OPP}) \tag{2.42}$$

$$W = \frac{1}{2} \cdot (S_{IP} + S_{OPP}) \tag{2.43}$$

B_0-inhomogeneities will affect the in-phase and opposed-phase condition (cf. Fig.2.6). In order to account for that, at least three echoes have to be acquired [36]. To further improve the

signal separation, lipid signals from all resonances have to be accounted for in the separation model. This multi-echo-Dixon approach (mDixon) requires the acquisition of multiple images at varying TE [37].

2.6 The human breast

In the following, the anatomy of the female human breast is briefly described. Within this thesis, a potential correlation of amide CEST MRI to the phase of the menstrual cycle was investigated. Therefore, the hormonal fluctuations during the menstrual cycle are shortly outlined. The reader is however referred to literature for deeper anatomical and physiological insights [38–40].

2.6.1 Anatomy

The female breasts (lat. *mammae*) contain the mammary gland with the main function of milk production for nurturing a baby. They overlay the pectoralis muscles and are covered by skin tissue. Breasts are part of the secondary sex characteristics and develop during puberty. The mammary gland is composed of glandular tissue and variable amounts of fat. The glandular tissue is divided into compartments, the so-called mammary lobes. Each breast consists of about 5 to 20 lobes. They secret into the mammary tubules forming the milk ducts which converge on the nipple (lat. *mammilla*) to the outside. The whole gland and the network of milk ducts is covered by subcutaneous fat and connective tissue. The anatomy of the female breast is schematically illustrated in Figure 2.7. Milk is only produced in response to hormonal signals which are initiated after giving birth [39].

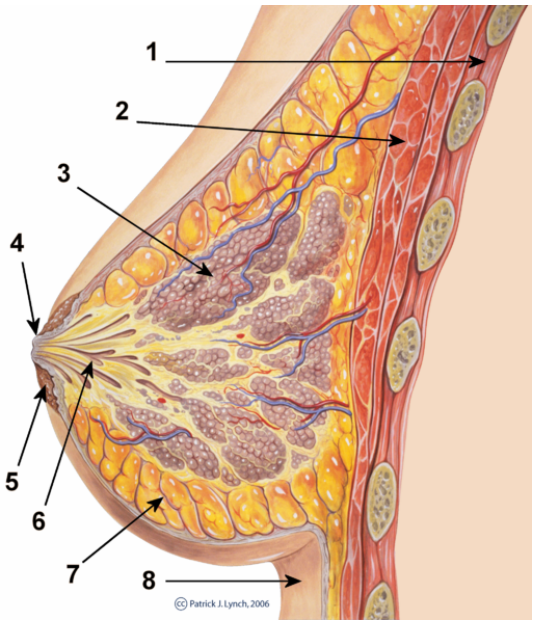

Figure 2.7: Schematic illustration of the anatomy of the female human breast. The arrows depict the following structures:
(1) Chest wall
(2) Pectoralis muscles
(3) Mammary gland (lobules)
(4) Mammilla
(5) Areola
(6) Milk duct
(7) Adipose tissue
(8) Skin
Original author: Patrick J. Lynch[1].

[1]Original author: Patrick J. Lynch. Reworked by Morgoth666 to add numbered legend arrows. (`https://commons.wikimedia.org/wiki/File:Breast_anatomy_normal_scheme.png`), „Breast anatomy normal scheme“, `https://creativecommons.org/licenses/by/3.0/legalcode`.

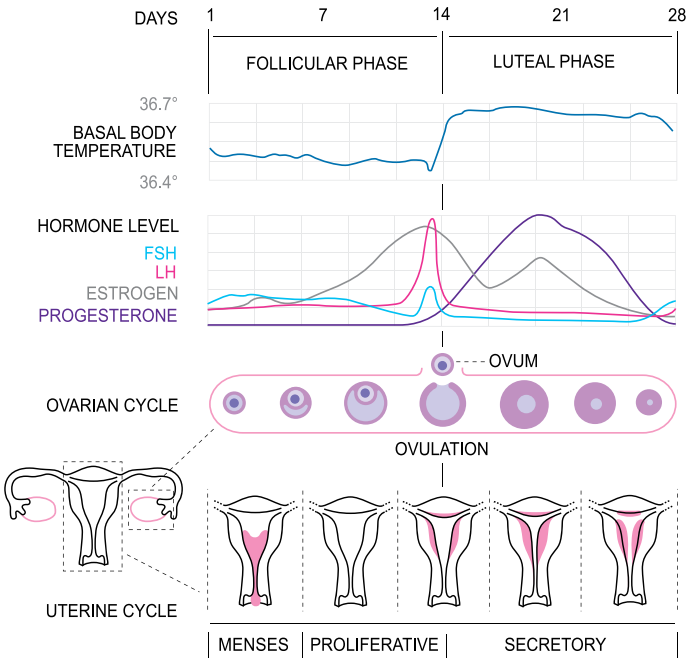

Figure 2.8: Hormonal changes during the menstrual cycle. The menstrual cycle can be divided into two phases: Follicular phase and luteal phase. Follicle stimulating hormone (FSH) affects the ovarian in the follicular phase, luteinizing hormone (LH) triggers the ovaluation which is followed by the luteal phase. Original author: Isometrik[2].

2.6.2 Hormonal changes during the menstrual cycle

Although the mammary gland lactates only during nurturing of infants, hormonal fluctuations during the menstrual cycle affect breast tissue of healthy premenopausal and non-lactating women as well. Hormonally induced changes in breast tissue vascularization were reported [41] as well as histological changes of breast tissue [42]. Fluctuations of the interstitial and intracellular water content introduce morphological changes [43].

The menstrual cycle is a regular and natural change in the uterus and ovaries that enable a potential pregnancy. It begins with the first day of menstruation and ends one day before the next cycle starts. One cycle is typically 28 ± 3 days long. The first half of the cycle is known as the *follicular phase* in which ovarian follicles are stimulated by the follicle stimulating hormone (FSH). The level of the estrogen estradiol rises to the end of the follicular phase, stimulating the production of the luteinizing hormone (LH). The LH initializes ovaluation at around the 14^{th} day of the cycle and the mature egg is released into the oviduct. The second half of the cycle is know as the *luteal phase*. LH and FSH interact with the growth of the follicle. If no fertilization occurs, progesterone levels drop and the next menstruation is triggered. Fluctuations of the different hormones and their affect on the body temperature, uterus and the ovum are given in Figure 2.8.

[2]Original author: Isometrik (`https://commons.wikimedia.org/wiki/File:MenstrualCycle2_en.svg`), „MenstrualCycle2 en“, `https://creativecommons.org/licenses/by-sa/3.0/legalcode`.

3 | Magnetization Transfer and CEST

This chapter governs the principles of magnetization transfer and chemical exchange saturation transfer (CEST) from a physical point of view. The reader is referred to review articles for more insights on magnetization transfer and CEST theory [8, 44, 45] and to dissertations for additional understanding in quantitative CEST MRI [28, 46].

3.1 Magnetization transfer processes

Additionally to the relaxation processes governed by the Bloch equations (cf. Sec. 2.2.2), interactions between different spin systems might occur. In the following, a brief description of the transfer of magnetization between two pools is given. A pool i is defined as a spin system of the same physical properties, i.e. resonance frequency δ_i, relaxation properties and identical *exchange rates* k_{ij} to other pools. Solutes (dubbed s) are less abundant than water (w), which represents the main pool. The magnetization transfer of such a two pool system is schematically illustrated in Figure 3.1. The magnetization transfer in aqueous media can in principle be attributed to three processes:

Chemical exchange
Between two pools, chemical reactions can induce a physical exchange of protons. Magnetization can be transferred since quantum mechanical properties of the spins are not affected by the exchange and the changing chemical environment. This process is known as *chemical exchange* (CE) [47].

Dipolar interaction
A coupled spin system is formed by spins in close proximity. Dipolar interactions between coupled systems result in a magnetization transfer. This can either lead to a cross relaxation or an enhancement of magnetization of one pool. This process is known as the *nuclear Overhauser effect* (NOE) [48].

Molecular interaction
Depending on the macromolecular environment, molecules can form a free or a bound motion state. A conformational transition between states of motion can alter the properties of bound protons within the molecules, which in return leads to an exchange of magnetization.

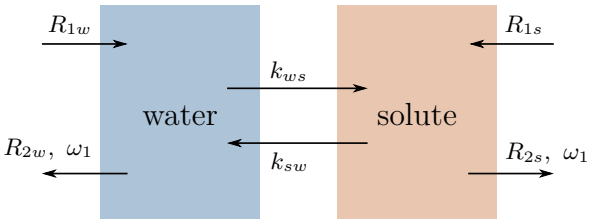

Figure 3.1: Schematic illustration of the two-pool model for water and a less abundant solute. The pools are defined by the resonance frequency δ of the spins and their relaxation rates R_1 and R_2. The exchange rate k characterizes the exchange between the two pools.

3.1.1 Bloch-McConnell equations

The *Bloch equations* (cf. Sec. 2.2.2) can be expanded with magnetization transfer terms. This yields a set of coupled differential equations, the *Bloch-McConnell equations*: [49].

$$\begin{aligned}
\frac{d}{dt}M_{xw} &= -\Delta\omega_w M_{yw} - R_{2w}M_{xw} + k_{sw}M_{xs} - k_{ws}M_{xw} \\
\frac{d}{dt}M_{yw} &= +\Delta\omega_w M_{xw} - R_{2w}M_{yw} - \omega_1 M_{zw} + k_{sw}M_{ys} - k_{ws}M_{yw} \\
\frac{d}{dt}M_{zw} &= -\omega_1 M_{yw} - R_{1w}(M_{zw} - M_{0,w}) + k_{sw}M_{zs} - k_{ws}M_{zw} \\
\frac{d}{dt}M_{xs} &= -\Delta\omega_s M_{ys} - R_{2w}M_{xs} - k_{sw}M_{xs} + k_{ws}M_{xw} \\
\frac{d}{dt}M_{ys} &= +\Delta\omega_s M_{xs} - R_{2w}M_{ys} - \omega_1 M_{zs} - k_{sw}M_{ys} + k_{ws}M_{yw} \\
\frac{d}{dt}M_{zs} &= -\omega_1 M_{ys} - R_{1s}(M_{zs} - M_{0,s}) - k_{sw}M_{zs} + k_{ws}M_{zw}
\end{aligned} \tag{3.1}$$

The Bloch-McConnell equations describe the dynamics of magnetization of the two pools w and s during RF irradiation with the frequency $\omega_1 = \gamma B_1$. The shift between the resonance frequency of the pool, δ_i and the frequency $\Delta\omega$ of the RF irradiation is $\Delta\omega_i = \Delta\omega - \delta_i$. As nomenclature, the uppercase Δ refers to the frequency shift of RF irradiation relative to a reference. The lowercase δ is assigned to a chemical shift of a pool relative to water. $R_{1,i} := \frac{1}{T_{1,i}}$ and $R_{2,i} = \frac{1}{T_{2,i}}$ represent the relaxation rates of the corresponding pools. $M_{0,i}$ is the equilibrium magnetization. The exchange rate k_{sw} describes transfer from solutes to water ($s \rightarrow w$) and k_{ws} describes the counter transfer ($s \leftarrow w$). In equilibrium, the following relation is valid:

$$k_{sw} \cdot M_{0,s} = k_{ws} \cdot M_{0,w} \tag{3.2}$$

The forward transfer rate can be formulated as $k_{ws} = f_s \cdot k_{sw}$, with the relative population fraction $f_s = \frac{M_{0,s}}{M_{0,w}}$. This is also known as the *relative concentration*. The set of equations can be expanded for the description of multiple solute pools exchanging with the water.

3.1.2 Chemical exchange

Chemical exchange of hydrogen bound in solutes, metabolites or proteins with the bulk water is regulated by acid-base reactions. The exchange rate k_{sw} is dependent on the chemical environment, namely pH, temperature T and the buffer concentration and type [50, 51]:

$$k_{sw}(pH, T) = k_{base}(T) \cdot 10^{pH - pK_w(T)} + k_{acid}(T) \cdot 10^{-pH} + k_{buffer} \tag{3.3}$$

with pK_w being the temperature dependent dissociation constant of water. k_{base}, k_{acid} and k_{buffer} are the base, acid and buffer catalyzed reaction rates, respectively. Exchange rates

of amide and amine protons are mainly base-catalyzed in *in vivo* like systems [52]. The temperature dependence of the reaction rates k in Equation 3.3 are governed by the *Arrhenius Law* [53, 54]

$$k(T) = k(298.1\,\mathrm{K}) \cdot \exp\left(\frac{E_a}{R}\left(\frac{1}{298.1\,\mathrm{K}} - \frac{1}{T}\right)\right) \tag{3.4}$$

with the activation energy E_a and the universal gas constant R. The exchange rate is therefore dependent on the chemical environment and character of the functional group.

3.1.3 Dipolar coupling

Spin systems in close proximity interact via dipolar coupling. Two coupled proton spins of $I = \frac{1}{2}$ couple to $S = 0$ or $S = 1$. Four spin states of the coupled spin system $|ws\rangle$ exist in an external magnetic field, which are depicted in Figure 3.2. Fluctuations in the local magnetic field due to molecular tumbling can induce transitions in a two-spin system of spins w and s. Each transition is associated by a probability W, which is dependent on the interaction distance r and the correlation time τ_c. The correlation time is the rotation duration of a molecule around an arbitrary axis. Magnetization is transferred in cross relaxation pathways of *flip-flip* or *flop-flop* transitions ($W_{0,ws}$) and *flip-flop* transitions ($W_{2,ws}$). In this context, the cross relaxation rate $\sigma = W_{2,ws} - W_{0,ws}$ is equivalent to a chemical exchange rate ($\sigma = -k_{sw}$) [48].

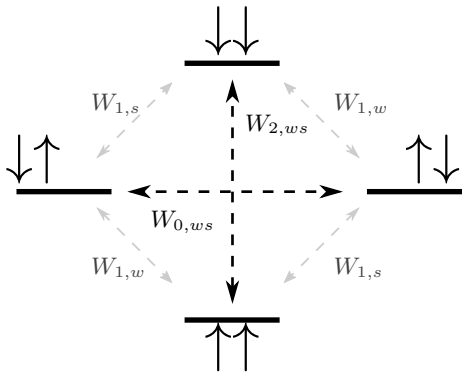

Figure 3.2: Energy levels of a dipolar coupled two-spin system in a static magnetic field. Transition between the spin states $|ws\rangle(w, s = \uparrow, \downarrow)$ is associated with the probability W. Magnetization can be transferred via the relaxation pathways $W_{0,ws}$ and $W_{2,ws}$.

3.1.4 Exchange-relayed NOE

Proteins and other larger biomolecules have a high abundance of hydrogen leading to intramolecular interactions of the proton spins. Sequences of flip-flop transitions can transfer magnetization for long distances and multiple pools, which is also known as *spin diffusion*. This also enables the magnetization transfer from non-exchanging hydrogen to other protons bound to the protein that are in chemical exchange with the water. This indirect transfer is known as the exchange-relayed NOE (rNOE) and is the dominant pathway for dipolar-coupling-based exchange with water protons [55]. The indirect magnetization transfer from non-exchanging protons to the water is illustrated in Figure 3.3.

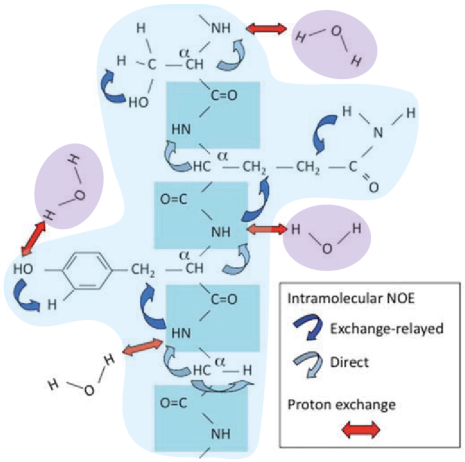

Figure 3.3: Schematic illustration showing intra- and intermolecular magnetization transfer pathways in a solute proteine. Red arrows indicate chemical exchange (CE). Dipolar coupling of bound protons with CE groups is indicated by a blue arrow. A light blue arrow shows dipolar coupling of two bound protons. Adapted from reference [55]

3.1.5 Semi-solid macromolecular magnetization transfer

Relevant for *in vivo* applications are the interactions between the macromolecular matrix and the water. The macromolecular matrix is composed of large and semi-solid components of a cell, e.g. the cell membrane or cytoskeleton. The so called semi-solid magnetization transfer is referred as MT [1]. The transversal relaxation time T_2 is in the order of microseconds due to the rigid structure of the macromolecular matrix, thus preventing a direct detection. Water molecules can bound for a short period of time at the surface of the matrix. The bound state increases the correlation time due to immobilization and enables inter-molecular NOE. Magnetization is transferred to the water pool via diffusion after unbinding. Additionally to transfer pathway via intermolecular NOE, rNOE processes contribute to the MT as well.

3.1.6 Functional exchanging groups that are abundant in human tissue

Within this thesis, particularly the amide but also amine protons were of interest. Amide protons origin in the peptide bond (i.e. -NH) and stand in CE with water protons. They resonate in the downfield at $\delta\omega_s = 3.5\,\text{ppm}$. Amine protons can be found in proteins or metabolites (-NH_2). A list of functional groups that are abundant in human tissue and exchange magnetization with the water is provided in Table 3.1. Literature values for exchange rates are given.

Table 3.1: Overview of exchanging functional groups that are abundant in human tissue. The resonance frequency and literature values for exchange rates are provided. Amine and amide protons exchange chemically with the water while aliphatic and aromatic bound protons transfer magnetization via rNOE processes. References: 1: Zhou et al. [52]; 2: Liu et al. [56]; 3: Liepinsh and Otting [47]; 4: Xu et al. [57]; 5: Friedman et al. [50]; 6: Goerke [58] 7: Jin and Kim [59].

Functional group		origin	$\delta\omega_s$ [ppm]	k_{sw}[Hz]
amide [1,2]	-NH	proteins	3.5	28.6-280
amine [3]	-NH_2	proteins/metabolites	2.0	700-10000
aliphatic [4,5]		proteins	-5 to -1	5-30
aromatic [6,7]		proteins	1 to 5	2-3

[1] Other studies used the acronym *ssMT*.

3.2 Chemical Exchange Saturation Transfer

Chemical exchange saturation transfer (CEST) enables the indirect detection of protons in solutes (e.g. metabolites, peptides or proteins) of low concentration in the millimolar range. In a CEST experiment, the signal of protons pools is enhanced via an accumulation of saturated magnetization in the water pool ($c \approx 55.5\,\mathrm{mol}$). This utilization of the magnetization transfer yields an indirect signal gain, the *proton transfer ratio* (PTE). The PTE is linearly dependent on both exchange rate and relaxation time:

$$PTE \approx k_{sw} \cdot T_{1,w} \tag{3.5}$$

3.2.1 The CEST experiment and the Z-spectrum

Two things are required to perform a CEST experiment: First, the magnetization of the solute pool is saturated by frequency selective RF saturation. During the saturation block, magnetization is transferred to the bulk water pool. Second, the subsequent readout of the modified water signal follows.
In CEST experiments performed on an MR spectrometer, saturation is achieved by a continuous wave (cw) RF irradiation.The parameters amplitude $B_1 = \omega_1/(2\gamma\pi)$, duration t_{sat} and offset to water $\Delta\omega$ define the saturation block. In order to achieve sufficient accumulation of saturation in the water, $t_{sat} \gg 1/k_{sw}$ has to be fulfilled. The duration t_{sat} is usually in the order of hundred milliseconds to several seconds. On-resonant saturation on the pool s leads to a transfer of saturated magnetization to the bulk water pool. Thereby, the equilibrium magnetization $M_{w,0}$ is decreased to $M_{z,w}(\Delta\omega)$ and detected in the subsequent water signal acquisition. This is depicted in Figure 3.4 A. Although the name *CEST* implies that magnetization transfer occurs solely due to CE, other transfer pathways with corresponding exchange rates and frequency shifts are included as well. This process of RF saturation and water signal acquisition is repeated multiple times at varying offsets $\Delta\omega$ (Fig. 3.4 B). If the saturation frequency is on-resonant on the water, the water pool w will be directly saturated. This effect is defined as *spillover* or *direct water saturation* (DS). By normalization of all $M_{z,w}(\Delta\omega)$ by $M_{w,0}$ the Z-spectrum is obtained:

$$Z(\Delta\omega) = \frac{M_{z,w}(\Delta\omega)}{M_{z,0}} \tag{3.6}$$

An exemplary Z-spectrum of a two-pool system is shown in Figure 3.4 C. Within this thesis, CEST experiments were combined with MRI (cf. Sec. 2.4). The images encode the water signal spatially and therefore allow a voxel-wise calculation of Z-spectra.

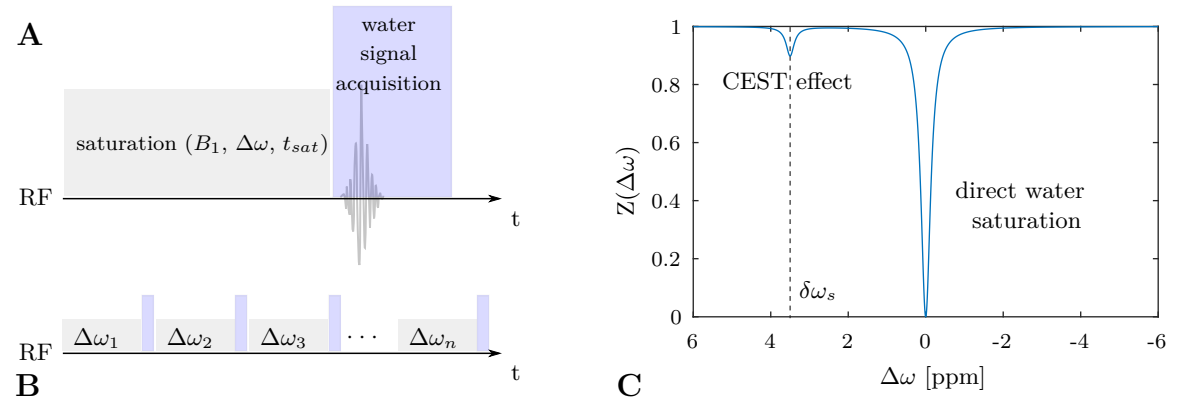

Figure 3.4: (A) Saturation block and signal acquisition in a CEST experiment. This is repeated for varying frequency offsets $\Delta\omega$ (B). The normalization by the equilibrium magnetization yields the Z-spectrum (C). The exchanging pool resonates at $\delta\omega_s = 3.5\,\text{ppm}$. Per convention, the frequency axis is plotted reversely.

3.2.2 Analytical solution of the Bloch-McConnell equations

An analytical solution of the first-order linear differential Bloch-McConnell equations can be obtained by an eigenspace approach [44, 60, 61]:

$$\vec{M}(t) = \begin{pmatrix} M_{xw} \\ M_{yw} \\ M_{zw} \\ M_{xs} \\ M_{ys} \\ M_{zs} \end{pmatrix} = \sum_{n=1}^{6} e^{\lambda_n t}\vec{\nu}_n + \vec{M}^{ss} \tag{3.7}$$

with the eigenvectors $\vec{\nu_n}$ and the eigenvalues λ_n of the two-pool magnetization vector $\vec{M}(t)$ and the steady-state solution $\vec{M}_{ss}$ [44, 61]. A sufficiently long saturation $t_{sat} \gg 1/R_{2,w}$ allows to neglect all eigenvalues except λ_1, thus presenting the relevant contribution to $\vec{M}_w$ [60]. Moreover, the eigenvector $\vec{\nu}_1$ is co-linear to $\vec{B}_{eff}$, the effective magnetic field (Eq. 2.21). The eigenvalue can be approximated by:

$$\lambda_1 = -R_{1\rho} \tag{3.8}$$

with the longitudinal relaxation rate in the rotating frame $R_{1\rho}$ [61]. Magnetization transfer can be described as an additional relaxation pathways. For a two-pool system, the exchange-dependent relaxation rate R_{ex} addresses the relaxation due to exchange and $R_{1\rho}$ is given by:

$$R_{1\rho}(\Delta\omega) = R_{eff}(\Delta\omega) + R_{ex}(\Delta\omega) \tag{3.9}$$

with the relaxation of the water pool R_{eff}. By defining $\theta = \arctan\left(\frac{\omega_1}{\Delta\omega}\right)$ the angle between $\vec{B}_{eff}$ and $\vec{B}_0$, the water proton relaxation rate in the rotating frame becomes:

$$R_{eff}(\Delta\omega) = R_{1w}\cos^2\theta + R_{2w}\sin^2\theta = R_{1w} + (R_{2w} - R_{1w}) \cdot \frac{\omega_1^2}{\omega_1^2 + \Delta\omega^2} \tag{3.10}$$

The chemical exchange or dipolar interaction can be understood as a spectrally selective relaxation pathway to the water magnetization in the rotating frame. After a cw saturation

for t_{sat}, the Z-spectrum is:

$$Z(\Delta\omega, t_{sat}) = (\cos^2\theta \cdot Z_{initial} - Z^{ss}) \cdot e^{-R_{1\rho} t_{sat}} + Z^{ss} \tag{3.11}$$

which becomes in the steady-state:

$$Z^{ss}(\Delta\omega) = \frac{\cos^2\theta R_{1,w}}{R_{1\rho}(\Delta\omega)} \tag{3.12}$$

The Z-spectrum at $\Delta\omega = 0\,\text{ppm}$ (DS) can then be calculated by $R_{ex} = 0$:

$$Z^{ss}_{DS,LS}(\Delta\omega) = \frac{\cos^2\theta R_{1,w}}{R_{\mathit{eff}}(\Delta\omega)} = 1 - \underbrace{\frac{\frac{\Gamma_w^2}{4}}{\frac{\Gamma_w^2}{4} + \Delta\omega^2}}_{\mathcal{L}_w} \tag{3.13}$$

which was transformed to a Lorentzian function $\mathcal{L}_w$ with the FWHM $\Gamma_w = 2\omega_1\sqrt{\frac{R_{2w}}{R_{1w}}}$. The exchange dependent relaxation R_{ex} can as well be transformed into a Lorentzian-shaped function.

$$R_{ex}(\Delta\omega) = R_{ex}^{max} \frac{\frac{\Gamma^2}{4}}{\frac{\Gamma^2}{4} + (\Delta\omega - \delta\omega_s)^2} \tag{3.14}$$

In the above equation, the back exchange k_{ws} was neglected due to the low abundance of the solute ($M_{0,w} \gg M_{0,s}$). Further, $R_{1s} \ll R_{2s}$ and $R_{1s} \ll k_{sw}$ was utilized [44]. The FWHM calculates to:

$$\Gamma = 2\sqrt{\frac{k_{sw} + R_{2s}}{k_{sw}}\omega_1^2 + (k_{sw} + R_{2s})^2} \tag{3.15}$$

The maximum R_{ex}^{max} is reached at $\Delta\omega = \delta\omega_s$ (cf. Fig. 3.4 C). In the *large shift limit* (LS), $|\delta\omega_s| \gg \omega_1$, it can be approximated by:

$$R_{ex}^{max} \approx f_s k_{sw} \cdot \alpha(\omega_1) \tag{3.16}$$

with the labeling efficiency $\alpha \in [0, 1]$ describing the CEST effect:

$$\alpha(\omega_1) = \frac{\omega_1^2}{\omega_1^2 + k_{sw}\,(k_{sw} + R_{2s})} \tag{3.17}$$

The LS condition holds for $B_0 = 7\,\text{T}$, $|\delta\omega_s| > 1\,\text{ppm}$ and $B_1 < 1\,\mu\text{T}$.

Multi pool system

The above equations can be expanded to describe a system of multiple pools of small size exchanging magnetization with the water, including the exchange-relayed rNOE and semi-solid magnetization transfer. The individual exchange processes $R_{ex,i}$ add up linearly:

$$R_{1\rho} = R_{\mathit{eff}} + \sum_i R_{ex,i} \tag{3.18}$$

In contrast, CEST effects add up inversely to the Z-spectrum [60]:

$$\frac{1}{Z^{ss}} = \frac{1}{Z^{ss}_{water}} + \sum_i \frac{1}{Z^{ss}_i} \tag{3.19}$$

The individual CEST effects can all be approximated by a Lorentzian-shaped function. The steady-state Z-spectrum is given by:

$$Z^{ss}(\Delta\omega) \approx 1 - \mathcal{L}_w - \sum_i \mathcal{L}_i \tag{3.20}$$

Within this thesis, the MT was fitted by a very broad Lorentzian function (cf. Sec. 5.7.1). Other fitting approaches by Gaussian-shaped or Super-Lorentzian-shaped functions can also be found in literature.

Pulsed saturation

On whole-body MRI, safety limitations prohibit the application of cw irradiation. Instead, a series of saturation pulses have to be used. Within this work, Gaussian-shaped pulses of pulse length t_p from 15 to 100 ms were used. The spectral bandwidth (BW) of the pulses can be approximated by: $BW \approx \frac{1}{t_p}$. The CEST sequence is depicted in Figure 5.2. The duty cycle (DC) is defined as:

$$DC = \frac{t_p}{t_p + t_d} \tag{3.21}$$

with the inter-pulse delay t_d. Due to the time-dependent irradiation power during the pulses, the Z-spectrum can be described by a mean $R_{1\rho}$: The time-dependent $R_{1\rho}(\Delta\omega, \omega_1(t))$ is averaged to $\overline{R_{1\rho}}(\Delta\omega)$, assuming Gaussian-shaped pulses [62]. Assuming $R_{1\rho}t_p \ll 1$ and $R_{1w}t_d \ll 1$, the steady-state solution for pulsed saturation in the LS is:

$$Z^{ss}_{pulsed,LS}(\Delta\omega) = \frac{R_{1w}}{DC \cdot \overline{R_{1\rho}}(\Delta\omega) + (1 - DC) \cdot R_{1w}} \tag{3.22}$$

3.3 Z-spectrum analysis

An exemplary Z-spectrum acquired in the human brain at 7 T is provided in Figure 3.5. Signal contributions from amide and amine resonances can be identified as well as ssMT, rNOE and a broad DS. This Z-spectrum illustrates the superposition of multiple exchanging pools and emphasizes the need of isolation of individual CEST effects for a more profound data interpretation. Isolation of CEST effects is the separation of the exchange from the pool of interest $R_{ex,s}$ from the DS R_{eff} and contributions from all other exchanging pools (pools $i, i \neq s$). The *label scan* Z_{lab} is the Z-value obtained for on-resonant saturation on pool s. For cw saturation the steady-state solution in the LS is given by:

$$Z^{ss}_{lab} = \frac{R_{1,w}}{R_{\mathit{eff}}(\Delta\omega) + \sum_i R_{ex,i}(\Delta\omega)} \tag{3.23}$$

A widespread used metric of Z-spectrum analysis is the determination of the magnetization transfer rate by an *asymmetry analysis* [52], which was as well applied in studies of CEST MRI in the human breast [13, 15, 63–65]. A label scan is simply subtracted from a reference scan Z_{ref}. The asymmetry is obtained by defining $Z_{lab} = Z(+\Delta\omega)$ and $Z_{ref} = Z(-\Delta\omega)$. The symmetrical axis is per definition at DS at $\Delta\omega = 0$ ppm. It can be shown that:

$$MTR_{asym}(\Delta\omega_s) = Z_{ref} - Z_{lab} = \frac{R_{1w}R^{max}_{ex,s}}{R_{\mathit{eff}}(R_{\mathit{eff}} + R^{max}_{ex,s})} \tag{3.24}$$

Although this metric contains a spillover correction of zeroth order, a clear isolation of a CEST effect is not given. This becomes also plausible in an actual acquired *in vivo* Z-spectrum in

Figure 3.5 in which different effects contribute differently on both sides of the spectrum.

A more robust approach for the definition of a reference spectrum is the sum of all other CEST effects than the pool of interest s:

$$Z_{ref}^{ss}(\Delta\omega) = \frac{R_{1,w}}{R_{\mathit{eff}}(\Delta\omega) + \sum_{i,i\neq s} R_{ex,i}(\Delta\omega)} \tag{3.25}$$

The pools can e.g. be identified by Lorentzian-line fitting (cf. Eq. 3.20, [66]). Zaiss *et al.* introduced the inverse metric which is linearly dependent to $R_{ex,s}^{max}$ [60]:

$$MTR_{Rex}(\Delta\omega) = \frac{1}{Z_{lab}} - \frac{1}{Z_{ref}} = \frac{R_{ex,s}}{R_{1w}\cos^2\theta} \tag{3.26}$$

A division of MTR_{Rex} by $T_{1,w}$ eliminates the scaling by R_{1w} and yields the *apparent exchange-dependent relaxation* (AREX)

$$AREX(\Delta\omega) = \frac{1}{T_{1,w}}\left(\frac{1}{Z_{lab}} - \frac{1}{Z_{ref}}\right) = \frac{R_{ex,s}}{\cos^2\theta} \tag{3.27}$$

Besides the term $\cos^2\theta = \frac{\omega_1^2}{\omega_1^2+\delta\omega_s^2}$, the AREX metric is a quantitative approach representing the relaxation rate of the chemical exchange. The longitudinal relaxation time of water $T_{1,w}$ has to be quantified in an additional measurement, e.g. by means of a saturation recover sequence.
In the large shift limit ($\delta\omega \gg \omega_1$), $\cos^2$ is approximately 1, leading to the following equation:

$$AREX(\Delta\omega) = f_s k_{sw}\frac{\omega_1^2}{\omega_1^2 + k_{sw}(k_{sw} + R_{2s})} \tag{3.28}$$

Pulsed saturation

The inverse metrics can be adapted for pulsed saturation using the DC [62]:

$$MTR_{Rex}(\Delta\omega) = DC \cdot \frac{R_{ex,s}}{R_{1w}\cos^2\theta} \tag{3.29}$$

$$AREX_{pulsed} = DC \cdot \frac{R_{ex,s}}{\cos^2\theta} \tag{3.30}$$

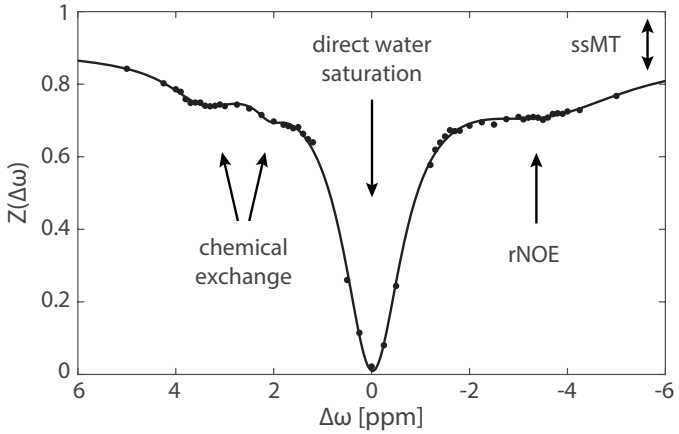

Figure 3.5: An exemplary Z-spectrum acquired at 7 T in the human brain shows multiple CEST effects. Contributions of amide and amine resonances via chemical exchange and aliphatic protons (rNOE) are small compared to the direct water saturation and and semi-solid macromolecular magnetization transfer. Reproduced with kind permission from Meissner [46].

Summary

With respect to the work presented in this thesis, the following points summarize the previous sections and the Z-spectrum analysis:

- Magnetization transfer can be understood as an additional spectrally selective relaxation pathway of the water magnetization in the rotating frame.
- Multiple CEST effects can be described using a pool model.
- The Z-spectrum can be approximated as a sum of Lorentzian-shaped functions representing the CEST effects.
- The AREX metric allows to isolate individual CEST effects and represents a full quantitative approach to determine the CEST effect.
- The steady-state assumptions requires a sufficiently long saturation.

4 A novel normalization for CEST MRI to correct for fat-signal-induced artifacts

CEST MRI can be complicated by the presence of fat, wherein lipid signals cause an incorrect normalization and thereby artifacts in the Z-spectrum [20]. The mammary gland of the human breast represents an organ of high inter-subject variability in both size and fat fraction. CEST MRI of the human breast is therefore prone to fat-signal-induced artifacts. To overcome these artifacts, other studies have applied fat saturation [14, 64], water excitation [65, 67, 68] or used a 3pt-Dixon water-fat-separation approach [15]. Within this thesis, a novel and alternative approach was developed enabling the correction of fat-signal-induced artifacts in the post-processing.

4.1 CEST MRI in the presence of fat

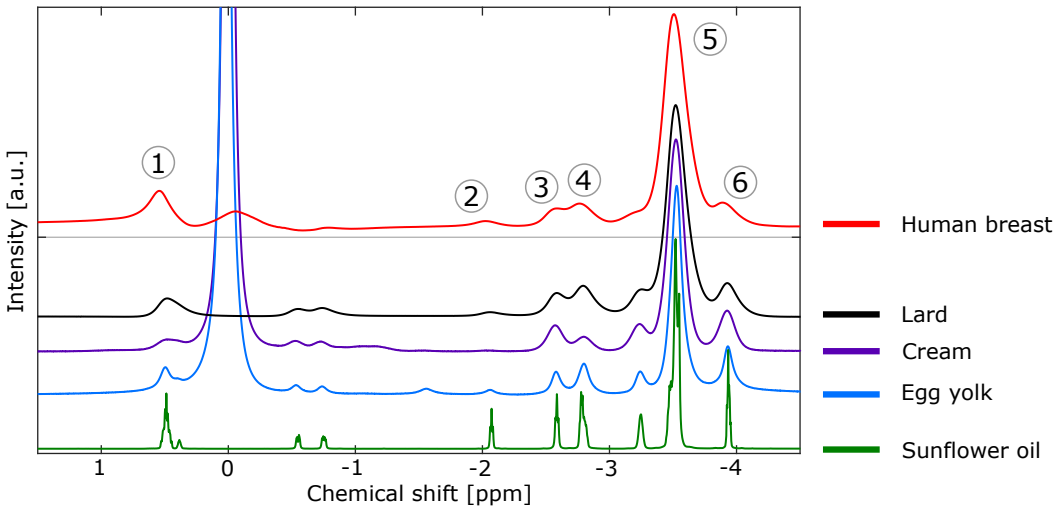

Figure 4.1: Proton spectra of various fat-containing samples (sunflower oil, egg yolk, cream, and lard) were measured at the 14.1 T spectrometer, while the upper red line shows a spectrum acquired at B_0=7 T in the breast of a healthy volunteer. The proton spectra show coinciding lipid resonances of different peak widths and amplitudes. Lipid resonances are grouped to six main signals in order to display their phase relation in the xy-plane (cf. Fig. 4.3). The dominant lipid peak (5) originates from methylene groups (CH_2). Parameters of spectra acquisition can be found in the Appendix.

Figure 4.1 shows the proton spectra of fat-containing samples, including one acquired in the breast of a healthy volunteer. Several coinciding lipid peaks of varying amplitudes and widths

can be identified. In GRE imaging of fat-containing tissue and organs, the detected MR signal is a superposition of water and lipid signals in the xy-plane. Generally formulated, the signal S in a voxel at readout time t (i.e. at echo time, TE) is [69, 70]:

$$S(t) = \left(W_0 + \sum_{n=1}^{N} F_{0,n} \cdot e^{i2\pi\Delta f_n \cdot t} \right) \cdot e^{i2\pi\Psi \cdot t} \tag{4.1}$$

with W_0 being the water signal and $F_{0,n}$ the amplitude of the n-th lipid peak. The index "0" indicates a fully relaxed signal. Ψ represents the B_0-inhomogeneities in that voxel (in Hz)[1]. The equation above can be interpreted as a dispersion of the individual lipid signals due to their different chemical shifts $\Delta f_n = \Delta\omega_n/2\pi$. The chemical shifts are given with respect to the water signal ($\Delta\omega_W = 0\,\text{ppm}$). Additionally, due to field inhomogeneities, all signals experience a phasing. This is schematically illustrated in Figure 4.2 A. Here, the lipid resonances in the proton spectrum were grouped to six signals for simplification (cf. Fig. 4.1), although ten lipid resonances can be resolved by MR spectroscopy of the human breast at B_0=7 T[31].
The phase relations of MR signals in the xy-plane become more construable when formulated in a vector notation. In general, the fully relaxed fat signal $\vec{F}_0$ is the collective sum of N signals, $\vec{F}_n$:

$$\vec{F}_0 = \sum_{n=1}^{N} \vec{F}_n \tag{4.2}$$

An unsaturated and fully relaxed image $\vec{S}_0$ is then the superposition of a water $\vec{W}_0$ and a fat $\vec{F}_0$ image:

$$\vec{S}_0 = \vec{W}_0 + \vec{F}_0 \tag{4.3}$$

As learned from Equation 4.1, the phase relation between $\vec{W}_0$ and $\vec{F}_0$ will ultimately be affected by the choice of the acquisition time t, or, with respect to GRE imaging, the parameter TE. The special case of a parallel alignment of $\vec{W}_0$ and $\vec{F}_0$ is defined as *in-phase*, while the *opposed-phase* defines an anti-parallel orientation.

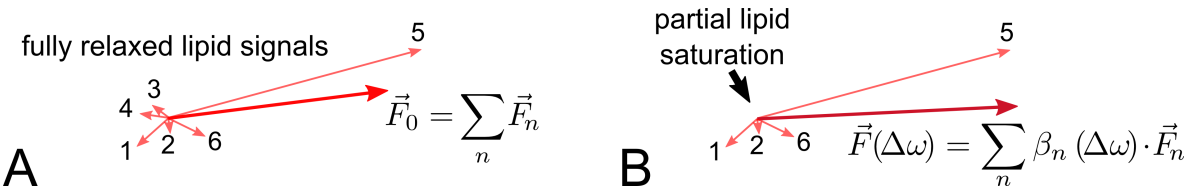

Figure 4.2: The phase relations of lipid signals in the xy-plane with and without saturation are depicted schematically. **A**: The individual lipid resonances, $\vec{F}_n$ are dephased at readout. They sum up to $\vec{F}_0$. **B**: The cumulative fat signal after partial lipid saturation, $\vec{F}(\Delta\omega)$, is changed in phase and amplitude compared to the fully relaxed fat signal, $\vec{F}_0$.

In a CEST experiment, the amplitude of the water signal $\vec{W}_0$ decreases, its phase is however conserved. Hence, the CEST effect at the frequency offset $\Delta\omega$ can be described by the scalar α:

$$\vec{W}(\Delta\omega) = \alpha(\Delta\omega) \cdot \vec{W}_0 \tag{4.4}$$

[1]For simplicity, R_2^* relaxation is neglected, since $TE \ll T_2$.

with $\alpha(\Delta\omega) \in [0,1]$. If the frequency offset $\Delta\omega$ during CEST coincides with lipid resonances, fat saturation occurs. The partial lipid saturation can be described by the scaling $\beta_n(\Delta\omega) \in [0,1]$. Consequently, the saturation of lipids will alter both, phase and amplitude of the collective fat signal:

$$\vec{F}(\Delta\omega) = \sum_{n=1}^{N} \beta_n(\Delta\omega) \cdot \vec{F}_n \tag{4.5}$$

This is schematically depicted in Figure 4.2 B. The acquired saturated image $\vec{S}(\Delta\omega)$ is again the sum of water (Eq. 4.4) and fat signals (Eq. 4.5):

$$\vec{S}(\Delta\omega) = \vec{W}(\Delta\omega) \quad + \quad \vec{F}(\Delta\omega) \tag{4.6}$$

$$= \alpha(\Delta\omega) \cdot \vec{W}_0 + \sum_{n=1}^{N} \beta_n(\Delta\omega) \cdot \vec{F}_n \tag{4.7}$$

Therefore, the phase and magnitude of the measured signal $\vec{S}(\Delta\omega)$ changes compared to the unsaturated $\vec{S}_0$. This change of orientation is illustrated in Figure 4.3.

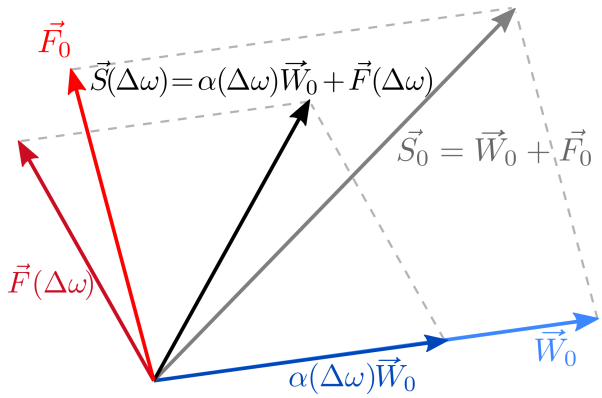

Figure 4.3: The phase relations of MR signals in the xy-plane with and without saturation are depicted schematically. The detected signal is a sum of water and lipid signals. The phase and magnitude of the pre-saturated image, $\vec{S}(\Delta\omega)$, change compared to the fully relaxed image $\vec{S}_0$.

Conventionally, a Z-spectrum is acquired by the normalization of an image acquired after pre-saturation by an unsaturated one:

$$Z_{conv}(\Delta\omega) = \frac{\left|\vec{S}(\Delta\omega)\right|}{\left|\vec{S}_0\right|} = \frac{\left|\alpha(\Delta\omega) \cdot \vec{W}_0 + \vec{F}(\Delta\omega)\right|}{\left|\vec{W}_0 + \vec{F}_0\right|} \tag{4.8}$$

It is apparent that the equation above does not yield the desired CEST effect α. The conventional normalization is instead affected by fat signal contribution, which leads to a well-known artifact in the spectral region of exchange-relayed nuclear Overhauser effects (rNOE, cf. Sec. 3.1.4): The Larmor frequency of the large methylene peak ($\delta\omega \approx -3.4\,\text{ppm}$) coincides with rNOE signals. The partial saturation of the methylene will decrease $\vec{F}(\Delta\omega = -3.4\,\text{ppm})$ significantly, leading to a dip in the Z-spectrum. This has been identified as the source of so-called *pseudo rNOE artifacts* in the upfield Z-spectrum by Lu *et al.* [20]. An exemplary Z-spectrum exhibiting a prominent pseudo rNOE artifact is shown in Figure 4.4.

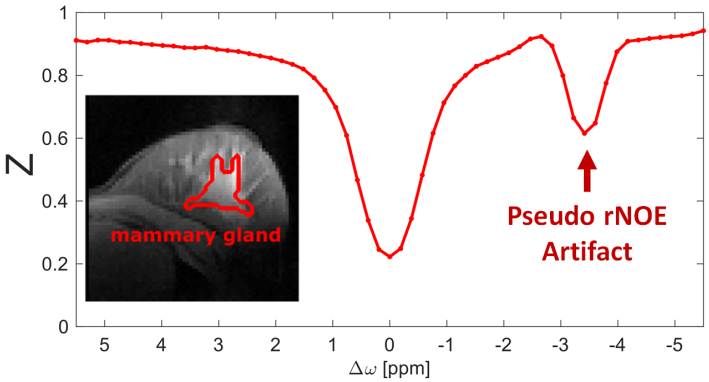

Figure 4.4: Exemplary Z-spectrum averaged in the gland of a healthy volunteer to demonstrate the pseudo rNOE artifact.

Zhang *et al.* investigated the influence of the echo time on the Z-spectrum appearance [63]. They demonstrated that not only the pseudo artifacts are influenced by the choice of TE, but also the direct water saturation (*DS*, i.e. at $\Delta\omega = 0\,\text{ppm}$). Both, the source of the pseudo rNOE artifact and the dependence on TE, is explainable by the derived general vector notation of MR signals and their phase relations during the CEST experiment. The understanding of the origin of those artifacts is directly followed by the awareness, that the application of the asymmetry analysis (MTR_{asym}) itself is highly questionable, if CEST is applied to fat-containing tissues and organs.

4.2 A novel normalization correcting for fat-signal-induced artifacts

Based on three assumptions, a post-processing method will be introduced in the following enabling the correction of APT signal for fat signal contributions.
The duration of the saturation train in a CEST experiment is usually in the order of several seconds. If no magnetization recovers during the readout, the pre-saturation would yield complete water saturation at $\Delta\omega = 0\,\text{ppm}$. This can be expressed by:

Assumption 1: $\alpha(\Delta\omega = 0\,\text{ppm}) = 0$

The technical limitations of whole-body scanners require the application of a pulsed pre-saturation train instead of cw. Gaussian-shaped RF pulses ensure a frequency selective saturation. Although some lipid signals resonate close to the water, no resonance coincides with the water peak at $\delta\omega = 0\,\text{ppm}$. One can therefore assume that the direct water saturation does not partially saturate lipid signal. This can be formulated as:

Assumption 2: $\beta_n(\Delta\omega = 0\,\text{ppm}) = 1 \quad \forall\ n$

which is equivalent to $\vec{F}(\Delta\omega = 0\,\text{ppm}) = \vec{F}_0$. This allows the detection of $\vec{F}_0$ by the measured residual magnetization at the frequency offset $\Delta\omega = 0\,\text{ppm}$. The fully relaxed fat signal in each voxel is thereby:

$$\vec{S}(\Delta\omega = 0\,\text{ppm}) = \vec{F}_0 \tag{4.9}$$

By the knowledge of the fat-only image $\vec{F}_0$, the fat fraction FF can be estimated in a Z-spectrum acquired with an in-phase relation of $\vec{W}_0$ and $\vec{F}_0$. The parallel alignment simplifies

Equation 4.8 to:

$$Z_{\text{conv, in-phase}}(\Delta\omega = 0\,\text{ppm}) = \frac{\left|\alpha(0\,\text{ppm})\vec{W}_0 + \vec{F}(0\,\text{ppm})\right|}{\left|\vec{W}_0 + \vec{F}_0\right|} = \frac{F_0}{W_0 + F_0} =: FF \quad (4.10)$$

Or in other words: The fat fraction can be calculated by the normalization of the fat-only image $\vec{F}_0$ by the fully relaxed image $\vec{S}_0$. The fat fraction provides useful information for data interpretation.

The fully relaxed water-only image $\vec{W}_0$ can be calculated by transforming Equation 4.3:

$$\vec{W}_0 = \vec{S}_0 - \vec{F}_0 \quad (4.11)$$

Since no lipid signals resonate in the spectral region of amides (i.e. at frequency offsets around $\approx 3.5\,\text{ppm}$), a third expression can be made:

Assumption 3: $\beta_n(\Delta\omega \approx 3.5\,\text{ppm}) = 1 \quad \forall\ n$

or in other words: the collective fat signal at frequency offsets that does not coincide with lipid resonances is equal to the equilibrium and fully relaxed fat signal, $\vec{F}\,(\Delta\omega) = \vec{F}_0$. These formulations can be used to define a novel, fat-signal-corrected CEST normalization yielding the true CEST effect α:

$$Z_{corr}(\Delta\omega) = \frac{\left|\vec{S}(\Delta\omega) - \vec{S}(0\,\text{ppm})\right|}{\left|\vec{S}_0 - \vec{S}(0\,\text{ppm})\right|} = \frac{\left|\vec{W}(\Delta\omega)\right|}{\left|\vec{W}_0\right|} = \alpha \quad (4.12)$$

The equations above therefore allow a post-processing based correction of the acquired data. This correction method furthermore accounts for lipid signals of all resonances and does not require additional measurements. All information needed is obtained by the acquisition of the Z-spectrum. However, in order to retrieve the phase information and generally apply $Z_{corr}(\Delta\omega)$, complex-valued images are required.

It is worth mentioning that Equation 4.12 simplifies for an in-phase relation of $\vec{W}_0$ and $\vec{F}_0$:

$$Z_{corr,in-phase} = \frac{|S(\Delta\omega) - S(0\,\text{ppm})|}{|S_0 - S(0\,\text{ppm})|} = \frac{Z - Z(0\,\text{ppm})}{1 - Z(0\,\text{ppm})} = \alpha \quad (4.13)$$

which enables the correction of Z-spectra without the need for complex-valued image data and hence allows the use of magnitude images.

4.3 Challenges

In order to bring the novel correction method into *in vivo* application and to enable relaxation-compensated amide CEST MRI of the human breast, several challenges had to be overcome. They are shortly described in the following.

Phase-sensitive imaging

The analysis of CEST data is usually performed on magnitude image data stored in the DICOM standard (*Digital Imaging and Communications in Medicine*). Here, the obtained images are calculated by the sum-of-squares (SOS) coil combination and saved with 12 bit depth. In order to investigate the interplay of water and fat during a CEST experiment, the phase information of the measurements were required. Therefore, the workflow was changed to a raw data based analysis. This enabled the application of adaptive coil combination algorithms that preserved the phase information and increased the overall SNR (cf. Sec. 5.3).

Field mapping and T1 mapping of the human breast

Lipid signals contributing to MR images also affect quantitative measures such as field mapping and T1 mapping. Robust field mapping as well as T1 mapping is required for relaxation-compensated CEST MRI [18]. A post-processing approach was not feasible. Instead, fat saturation was chosen to overcome lipid signals. The GRE sequence itself provides an built-in option of fat saturation. It consists of one 90° sinc pulse played out before each k-space line, increasing the TR by 10 ms. This option, however, is SAR costly and the duration of k-space acquisition is significantly prolonged. To overcome this, an own fat saturation was developed.

Breast imaging at 7 T

The human breast is a deformable organ, which presents a challenge for MR acquisitions at high fields. An imaging protocol to reduce motion artifacts had to be developed. Most importantly, all *in vivo* examinations had to be synchronized to the breathing of the examined women.

5 | Materials and Methods

This chapter introduces the equipment and methods used for MR imaging and data analysis in this work. Furthermore, a comprehensive theory of the derived fat-corrected CEST normalization, which comprises the core of the thesis, is given.

5.1 MR imaging systems

All MR imaging experiments performed in this work were done on a 7 Tesla whole-body MR tomograph (MAGNETOM 7 T, Siemens Healthineers, Erlangen, Germany) at the German Cancer Research Center (DKFZ). The static magnetic field of $B_0 = 6.98\,\mathrm{T}$ results in a resonance frequency of $\nu_0 = 297.155\,\mathrm{MHz}$ for $^1\mathrm{H}$. Two coils were employed for imaging:

1. A 1Tx/16Rx bilateral diagnostic breast array by Rapid (Rapid Biomedical GmbH, Rimpar, Germany) for phantom experiments and *in vivo* examinations (Fig. 5.1).
2. A 1Tx/24Rx head coil by Nova Medical (Nova medical Inc., Wilmington, USA) for phantom experiments.

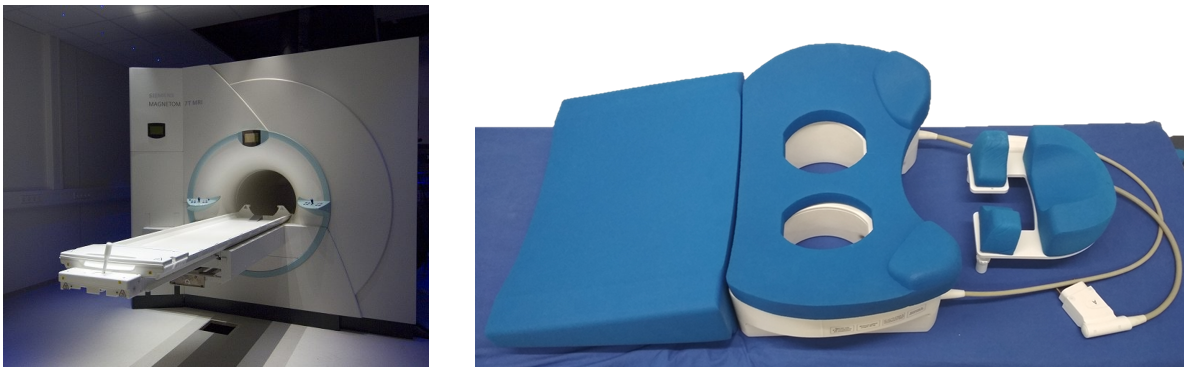

Figure 5.1: Left: Picture of the 7 Tesla whole-body MR tomograph at the German Cancer Research Center (DKFZ) (MAGNETOM 7 T, Siemens, Erlangen. Image from [71]). **Right:** A picture of the bilateral diagnostic breast array used in this work (1Tx/16Rx, Rapid Biomedical GmbH, Rimpar, Germany). The blue mattress provides padding and increases patient comfort.

5.2 The CEST sequence

The CEST sequence consists of a pre-saturation block and a subsequent image acquisition, which is based on a Siemens product sequence (Siemens Healthineers, Erlangen, Germany; [72]). Saturation is achieved by a series of n Gaussian-shaped RF-pulses. Each pulse has the duration t_p and a mean amplitude B_1. Its frequency offset $\Delta\omega$ is changed for each image for

the acquisition of a Z-spectrum. In between the pulses, the time delay t_d is used for gradient spoiling. The duty cycle (DC) is defined by:

$$DC = \frac{t_p}{t_p + t_d} \tag{5.1}$$

The complete saturation time t_{sat} is:

$$t_{sat} = n \cdot t_p + (n-1) \cdot t_d = (n-1) \cdot \frac{t_p}{DC} + t_p \tag{5.2}$$

A recovery time t_{rec} prior to the saturation pulse train can be set. In order to acquire a fully relaxed image, it was set to $t_{rec,M0} = 12\,\text{s}$. For the acquisition of pre-saturated images, the recovery time was set to $t_{rec} = 0\,\text{s}$. A GRE sequence followed the pre-saturation to acquire the water signal. In order to acquire a complete Z-spectrum, the saturation block was repeated for various $\Delta\omega$. A schematic illustration of the CEST sequence is given in Figure 5.2.

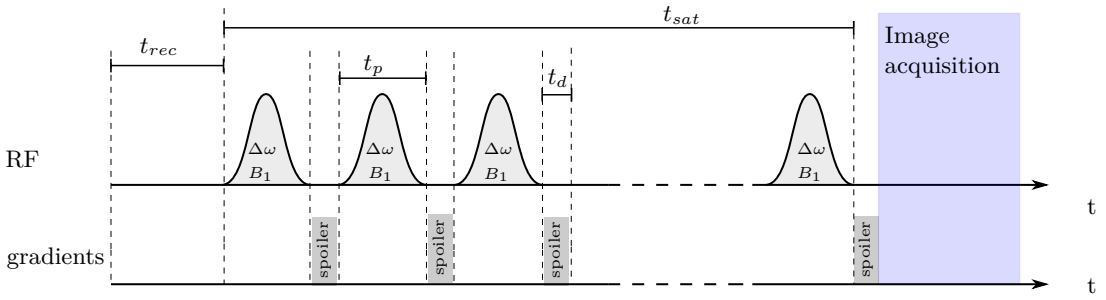

Figure 5.2: Schematic illustration of the CEST sequence. The saturation block consists of a series of Gaussian-shaped RF-pulses with the frequency offset $\Delta\omega$, duration t_p, and mean RF amplitude B_1. A spoiling is played out by the gradients in between the pulses for the duration t_d.

5.3 Image reconstruction

The phase information of the acquired MR images was required for the application of the novel CEST normalization (cf. Chapter 4). Therefore, images were reconstructed based on raw data. The MR signal obtained with multi-channel coils can be combined and reconstructed to a single image of complex-valued intensities. A Matlab-toolbox[1] providing an adaptive coil combination algorithm was utilized for the image reconstruction [73]. In comparison to the sum-of-squares technique, the reconstruction based on the adaptive combination algorithm increases the SNR [73]. An advancement of the adaptive combination algorithm incorporated phase information in the optimizing of the coil weightings, which resulted in unwrapped phases of the reconstructed, complex-valued images [74, 75]. The effect of both algorithms on the phase maps is demonstrated in Figure 5.3. The second, more advanced reconstruction provides smooth and steady phase maps (cf. Fig. 5.3 C). This optimized algorithm was therefore used for the reconstruction of all acquired data within this thesis.

[1]Kindly provided by Dr. Philipp Ehses, German Center for Neurodegenerative Diseases (DZNE), Bonn, Germany.

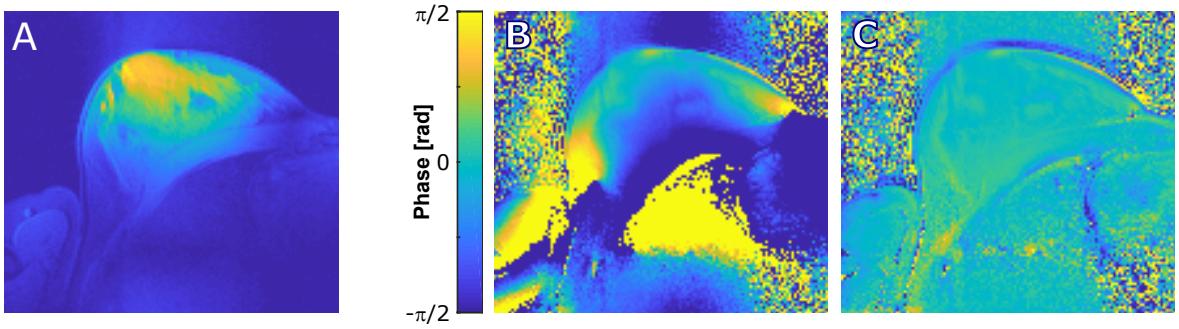

Figure 5.3: Fully relaxed image (A) and corresponding phase maps obtained by two sets of coil weightings. The phase map obtained by an adaptive combination algorithm by Walsh *et al.*[73] shows inhomogeneities (B). In contrast, the image reconstruction incorporating a phase unwrapping and phasing of the image provides smooth and even phase maps (C) [73–75].

5.4 Implementation of SAR and time-efficient fat saturation

The built-in fat-saturation option of the GRE sequence was inadequate for application due to the increased SAR and imaging acquisition time. Therefore, a SAR- and time-efficient fat saturation was developed for T1 and field mapping[2]. It consisted of five 90° Gaussian-shaped pulses prior to image acquisition. The pulses had a length of $t_p = 2.5\,\text{ms}$ and a power of $B_1 = 2.35\,\mu\text{T}$. A spoiling time of 2 ms was placed between the pulses. The center frequency was set to $\Delta\omega = -3.3\,\text{ppm}$. The complete fat saturation block had a length of 20.5 ms.

5.5 B_0 and B_1 field mapping

Field mapping was performed with the *water shift and* B_1 *mapping* (WASABI) method [3] [76]. The WASABI sequence consists of a rectangular preparation pulse with varying off-resonance that induces a sinc-like oscillation pattern in the frequency domain[4]. The acquired and normalized spectrum, $Z(\Delta\omega)$, is dependent on both transmit field power B_1 and the actual water frequency $\delta\omega$. Schuenke *et al.* suggested a rectangular pulse with a duration of $t_p = 5\,\text{ms}$ and amplitude $B_1 = 3.7\,\mu\text{T}$ for field mapping at 3 T [76]. To increase the spectral range of the oscillations, these settings were adapted to $t_p = 2.5\,\text{ms}$ and $B_1 = 7\,\mu\text{T}$. The standard sampling of Z-spectra consisted of 31 equally spaced offsets in the range of $\Delta\omega = \pm 4\,\text{ppm}$. The developed fat-saturation block was played out after the preparation pulse (see Sec. 5.4). The spectrum was fit according to:

$$Z(\Delta\omega) = \left| c - d \cdot \sin^2\left(\tan^{-1}\left(\frac{\gamma \cdot B_1}{\Delta\omega - \delta\omega}\right)\right) \cdot \sin^2\left(\sqrt{(\gamma \cdot B_1)^2 + (\Delta\omega - \delta\omega)^2} \cdot \frac{t_p}{2}\right)\right| \tag{5.3}$$

The parameters c and d are free and describe the amplitude and modulation of the oscillation. The B_0-shift map was calculated by $\Delta B_0 = \gamma \cdot \delta\omega$. To further stabilize the fit, phase information of the acquired images can be utilized to circumvent the calculation on positive magnitudes as

[2] MRI sequence programming was done within the Integrated Development Environment for MR Applications (IDEA, Siemens Healthcare, Erlangen, Germany).

[3] In this thesis, B_1 refers to the transmit field power. In the literature, the transmit field is sometimes referred as B_1^+.

[4] Only the pre-saturation block is changed, but the imaging is the same as in CEST measurements.

in Equation 5.3.

$$Z_{phase-corr.}\left(\Delta\omega\right) = \left|\vec{Z}\left(\Delta\omega\right)\right| \cdot sgn\left\{\Re\left(\vec{Z}(\Delta\omega) \cdot \exp\left(-i \cdot \angle\left(\vec{M}_0\right)\right)\right)\right\} \tag{5.4}$$

An alternative B_0 mapping approach used in this work was the internal water shift calculation in CEST experiments: The water shift was determined voxel-wise by the result of the center frequency of the Lorentzian fit. This approach was found to be more robust in *in vivo* examinations and avoided motion within the sequences.

5.6 T1 mapping

A T1-map of water is required for the calculation of relaxation-compensated CEST contrasts. A saturation recovery sequence preparation was used for the measurement: Three adiabatic half passage pulses of $\mu = 6, BW = 1200\,\text{Hz}$ and a length of $t_p = 8\,\text{ms}$ achieved complete signal saturation. After a delay (termed $t_{recover}$), five fat saturation pulses (cf. Sec. 5.4) were played out. The recovery was sampled at 17 different recovery times[5]. The descending order of recovery times supported the image reconstruction, which computes the coil weightings on the first acquired image of an experiment. The recovery of the longitudinal signal, M_z, was fitted by an exponential function in each voxel [77]:

$$M\left(t\right) = \left|M_0\left(1 - e^{-t/T_1}\right)\right| \tag{5.5}$$

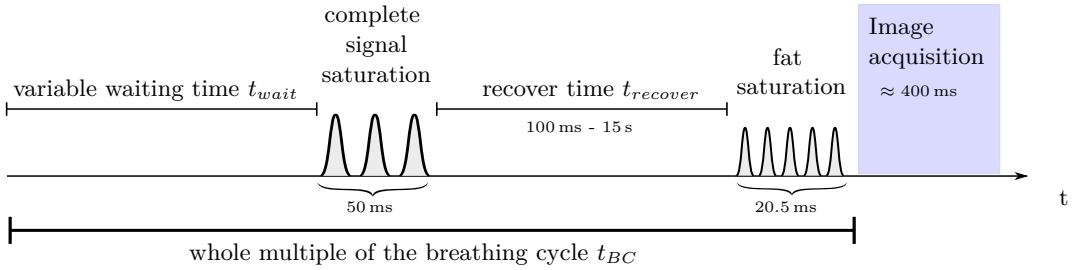

Figure 5.4: Schematic illustration of the saturation recovery sequence. The waiting time in the beginning ensures the synchronization of the sequence to the breathing of the subjects.

In order to maintain the synchronization of the sequence to the natural breathing rhythm of the women (cf. Sec. 5.9), a waiting time t_{wait} was introduced prior to the saturation recovery block. It was calculated for each recovery time such that the overall waiting time before image acquisition was a whole multiple of the breathing cycle duration, t_{BC}:

$$t_{wait} = N \cdot t_{BC} - t_{sat} - t_{recover} \tag{5.6}$$

$$\text{with} \quad N = \left\lceil \frac{t_{sat}+t_{recover}}{t_{BC}} \right\rceil \tag{5.7}$$

where t_{sat} denotes the time requirement of the fat saturation block and complete signal saturation before the recovery time ($t_{recover}$). The imaging time itself ($\approx 400\,\text{ms}$) was not accounted for in the calculation. A schematic illustration of the recovery sequence is depicted in Figure 5.4.

[5]The standard protocol consisted of the following recovery times: $t_{recover}$=15 000, 10 000, 5000, 4500, 4000, 3500, 3000, 2500, 2000, 1600, 1300, 1000, 800, 600, 400, 200, and 100 ms.

5.7 CEST evaluation

This section describes how the isolated CEST contrast is calculated on Z-spectra. Z-spectra are obtained by the voxel-wise normalization of pre-saturated images, with or without the developed fat correction (see Sec. 4).

5.7.1 Determination of Z_{lab} and Z_{ref}

To isolate CEST effects and apply the inverse metric, a model was fitted to the Z-spectra[6]. Fitting furthermore compensates noise and outliers in spectra. Each CEST pool n was approximated by a Lorentzian function $\mathcal{L}_n$:

$$\mathcal{L}_n(\Delta\omega) = A_n \frac{\frac{\Gamma_n^2}{4}}{\frac{\Gamma_n^2}{4} + (\Delta\omega - \delta_n)^2} \tag{5.8}$$

where δ_n represents the center (resonance frequency) with respect to water ($\delta_{water} = 0$), Γ_n the FWHM, and A_n its peak amplitude. The fit allowed the definition of the labeled Z-value, Z_{lab}, and the reference Z_{ref}. The complete fit serves as label Z_{lab}, while the Lorentzian pool of interest is excluded for the reference.

Z-spectra obtained *in vivo* in the human breast were fitted by a superposition of five Lorentzians [18, 66]. This five-pool model describes effects from the direct saturation of water, the semi-solid MT, amides, and amines. The lipid-signal-induced pseudo rNOE artifact as well as real signals of aliphatic rNOE were fit by a combining fifth pool for simplification. Thereby, the CEST effect of real rNOE signals could not be retrieved from the data, however, the overall robustness of the fit itself improved. The labeled Z-spectrum is:

$$Z_{lab}(\Delta\omega) = c - (\mathcal{L}_{water}(\Delta\omega) + \mathcal{L}_{MT}(\Delta\omega) + \mathcal{L}_{amide}(\Delta\omega) + \mathcal{L}_{amine}(\Delta\omega) + \mathcal{L}_{rNOE}(\Delta\omega)) \tag{5.9}$$

The offset c accounts for imperfect signal recovery. The start parameters were optimized for application in the human breast and are listed in Table 5.1.
Z-spectra obtained in the carnosine phantom were fitted by a single Lorentzian of the sole amide resonance and a second-order polynomial background:

$$Z_{lab}(\Delta\omega) = a \cdot (\Delta\omega)^2 + b \cdot \Delta\omega + c - \mathcal{L}_{amide}(\Delta\omega) \tag{5.10}$$

A table listing the start values as well as boundaries can be found in Appendix A.2.
The reference spectrum can be calculated by:

$$Z_{ref,\ n}(\Delta\omega) = Z_{lab}(\Delta\omega) + \mathcal{L}_n(\Delta\omega) \tag{5.11}$$

[6] All fit analysis was performed with Matlab 2017b (The MathWorks, Inc., Natick, Massachusetts, USA) utilizing a C/C++ implementation of the Levenberg-Marquardt non-linear least squares minimization algorithm [78].

Table 5.1: List of start parameters of the five-pool model used for fitting *in vivo* Z-spectra. A complete list with boundaries can be found in Appendix A.1.

Pool	Amplitude A	FWHM Γ [ppm]	frequency offset δ [ppm]
water	0.90	1.4	0
amide	0	1.4	3.5
amine	0	50	2.2
MT	0	1.40	−2.0
rNOE/fat	0	1	−3.5
offset c	1		

5.7.2 B_0 correction of Z-spectra

Spectral shifts of Z-spectra are observable in CEST MRI at high field strengths due to the increased B_0-inhomogeneities within the imaging plane. These shifts are particularly noticeable at the DS if its center frequency is not at $\Delta\omega = 0\,\text{ppm}$. In previous works, a B_0-correction was performed. The well-established *WASSR* algorithm by Kim *et al.* was utilized to correct Z-spectra [79]. It interpolates spectra to high spectral resolution and re-shifts to the actually used set of frequency offsets.

However, this method is not suitable for application to CEST data in the presence of fat. The interpolation of acquired data significantly smooths the data, potentially leading to artifacts of CEST contrasts. A B_0-correction of the investigated phase artifacts of the DS is especially error prone. In order to avoid data manipulation, the relative B_0-shift was instead accounted for in the determination of the label and reference spectra. Z_{lab} and Z_{ref} were calculated at the actual frequency offset $\Delta\omega$ on a voxel-by-voxel basis, by utilizing a ΔB_0-map:

$$\Delta\omega = \Delta\omega_{uncorr} + \Delta B_0 \tag{5.12}$$

$\Delta\omega_{uncorr}$ represents the nominal saturation offset affected by a B_0-shift. Non-B_0-corrected Z-spectra presented no obstacle in the fitting process itself. The robustness of the five-pool Lorentzian fit was verified for varying start parameters in the dissertation of Windschuh [28], which supports this alternative correction approach.

5.7.3 Calculation of the isolated amide contrast

With the knowledge of Z_{lab} and Z_{ref}, one can obtain the apparent exchange-dependent relaxation, the AREX contrast [16]:

$$AREX(\Delta\omega) = \frac{DC}{T_1} \cdot \left(\frac{1}{Z_{lab}(\Delta\omega)} - \frac{1}{Z_{ref}(\Delta\omega)} \right) \tag{5.13}$$

T1 is the longitudinal relaxation time obtained by a saturation recovery experiment and DC is the duty cycle of the pulsed saturation. $AREX_{amide}$ was calculated at $\Delta\omega = 3.5\,\text{ppm}$ and 3.16 ppm for analysis of *in vivo* spectra and the carnosine experiment, respectively. AREX maps of amine effects were calculated at $\Delta\omega = 2.2\,\text{ppm}$.

5.7.4 B_1 contrast correction

CEST effects depend strongly on the saturation amplitude B_1[18, 44]. Due to the breast coil design and the high field strength of 7 T, increased inhomogeneities of the transmit field are

expected in examinations of the human breast within a comparatively small volume. As a rule of thumb, deviations of up to ±40 % from the nominal B_1 can be observed within one breast. The correction method for B_1-inhomogeneities published by Windschuh *et al.* was employed (termed two-point contrast-B_1 correction [18]). A spline interpolation between isolated CEST contrast values determined in two consecutive experiments with varying saturation powers results in the final contrast. Usually, B_1 values were first set to $B_1 = 0.9\,\mu T$ and then lowered to $B_1 = 0.6\,\mu T$ in the subsequent examination. The reference voltage was not changed for the two experiments in order to keep the flip angle constant. The method is valid for each exchanging pool [18] and was applied on AREX contrast maps of amide and amine resonances. Contrasts were reconstructed to $B_{1,reconstr} = 0.8\,\mu T$.

5.8 Phantoms

The verification of the developed fat saturation for robust field and T1 mapping was performed in a cream containing phantom. The dairy product cream with a fat content of 30% is a cheap and easy to handle model solution for MR experiments. Four vials filled with cream were placed inside a MR compatible thermo flask (Coleman Jug, 1.8 l). The flask, completely filled with saline, served for temperature stabilization.

A carnosine model solution was prepared for the *in vitro*verification of the novel normalization (Sigma-Aldrich, Steinheim, Germany). The dipeptide carnosine (β-alanyl-L-histidine) has a single exchanging amide proton at the peptide bond. It was therefore used to prepare a one-pool CEST model solution [80]. A phosphate buffered carnosine solution (PBS, 1/15 M) with a pH of 8.06 and a concentration of $c_{carnosine} = 300\,mM$ was prepared and filled into a Nalgene 1L container. Sunflower oil was poured on top. In order to demonstrate how fat signal contribution affects the APT signal, the imaging plane for CEST measurements was set in the interface between the oil and carnosine solution and slightly tilted. Thereby, a fat fraction gradient was created along the image. This is schematically illustrated in Figure 5.5. Similar setups were used in [37] or [63]. The CEST experiment was performed at room temperature (T = 22 °C).

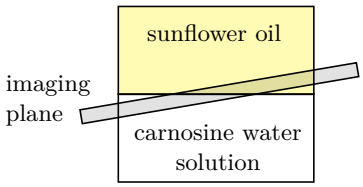

Figure 5.5: Schematic illustration of the carnosine-oil phantom setup. The tilted imaging plane created a fat fraction gradient in the images.

5.9 In vivo application

All examinations were approved by the local ethics committee of the Medical Faculty of the University of Heidelberg and are in accordance with the relevant guidelines and regulations. Written informed consent was received from all subjects prior to examinations. The examined women were not pregnant nor breastfeeding. They did not use hormonal contraceptives nor had implanted intrauterine contraceptive devices.

5.9.1 Healthy volunteers

CEST data of four healthy premenopausal women are shown within this thesis. The age of the examined volunteers was 31 (volunteer abbreviated as V1), 26 (V2), 23 (V3), and 23 (V4). Imaging and saturation parameters were mostly the same as in the stated protocol in Section 5.9.4 below. If parameters had to be adapted in order to address particular questions for the development of amide CEST MRI, they are listed in the Appendix.

Dependence of $AREX_{amide}$ on menstrual cycle

Breast parenchyma undergoes histologic and vascular [41–43] hormonally induced changes during the menstrual cycle. The guidelines from the European Society of Breast Imaging advise to perform a dynamic contrast enhanced breast MR examination between the 5^{th} and 12^{th} day of the menstrual cycle of premenopausal women [4]. Although diffusion weighted MRI appears to be unaffected by the menstrual cycle [5], it is unknown whether the amide CEST contrast underlies hormonal induced changes. To investigate a potential dependence, V1 was examined weekly for six times, beginning at the 10^{th} day of her menstrual cycle.

Furthermore, to explore this question within a small cohort of healthy volunteers, a clinical pilot study started in autumn of 2018 within a collaboration of the Department of Radiology (DKFZ) and the Department of Gynecology and Obstetrics (University Hospital Heidelberg)[7]. The study plans to examine 15 healthy women once in the follicular phase (between the 2^{nd} and 5^{th} day of the cycle) and a second time two weeks later (luteal phase, cf. Sec. 2.6.2). The volunteers V2,V3, and V4 were included in this pilot study and are presented within this thesis.

5.9.2 Patient cohort

The data of mamma carcinoma patients presented in this work are part of an ongoing clinical patient study initiated by the Departments of Radiology (DKFZ) and Gynecology and Ostetrics (University Hospital Heidelberg)[8]. The aim of this study is to investigate the feasibility of differentiating malignant from benign tissue by means of relaxation-compensated amide CEST MRI in the human breast and to compare the amide contrast to conventional clinical MR images. As a first step, twelve patients are planned to be examined by the established protocol and evaluated descriptively. In this work, three patients of this collective are presented and listed in Table 5.2. If required and orally approved by the patients, the TSE sequence was repeated with optimized shim and voltage settings after the CEST measurements.

Table 5.2: Data of the patient cohort presented in this work.

Patient abbrevation	Age	Locality	Type	Grading
P1	58	right	invasive mucinous carcinoma	G2
P2	31	left	invasive ductal carcinoma	G2
P3	43	right	invasive ductal carcinoma	G2

[7]Title: *Evaluation of menstrual cycle dependence of CEST MRI at 7T in pre-menopausal women*
[8]Title: *Chemical Exchange Saturation Transfer (CEST) MR mammography at 7T*

5.9.3 Breast imaging and breathing synchronization

All women were imaged in head-first prone position with their arms tight. Wearing scrubs during the examinations supported the breasts, which increased overall comfort and reduced motion artifacts. Unilateral and transversal imaging of only one breast improved shimming results and reduced the imaging time. If possible, imaging of the right breast was preferred in order to avoid flow artifacts of the heartbeat.

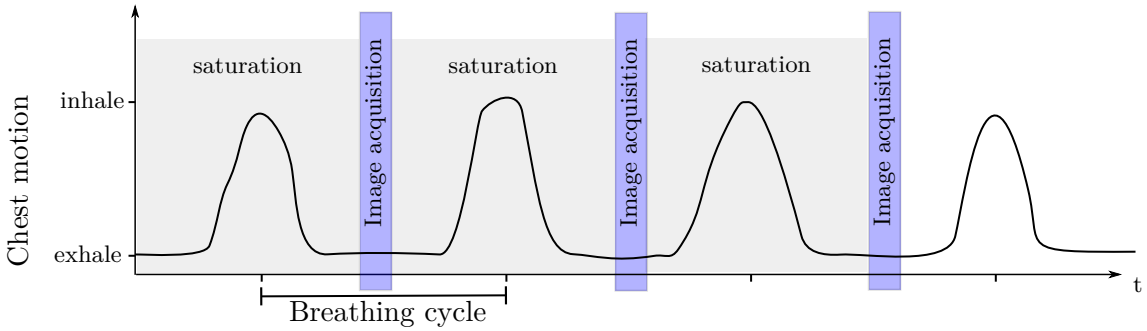

Figure 5.6: Schematic illustration of the breathing-induced chest motion during the CEST sequence. The saturation duration is adapted to synchronize the CEST sequence to the breathing cycle of the examined woman. Thereby, motion-induced artifacts as well as the non-rigid deformation of the imaged breast are avoided. Typically, one breathing cycle is 6 to 8 seconds long.

The subjects were asked to synchronize their breathing with the acoustic rhythm of the sequence in order to reduce motion artifacts. The motion of the chest during breathing and the timing of saturation and imaging is schematically illustrated in Figure 5.6. The tone of the pre-saturation is a deep and mumbling noise while the image acquisition sounds like a horn for only 0.4 s. The examined women therefore aimed to breathe freely during saturation and having finished exhalation before the start of image acquisition. This proceeding was preferred, since the exhaled state is more reproducible and an almost free breathing over the course of the whole examination was feasible.

5.9.4 In vivo examination protocol

Breast examinations were performed using the 2D GRE CEST sequence in single-slice mode (cf. Sec. 5.2). Acquisition parameters can be found in Table 5.3. The standard CEST protocol is listed below.

- **Localizer**: Images can be obtained with built-in fat suppression if the SAR limit is not exceeded.
- **Anatomical images**: A multi-slice T2-weighted turbo-spin-echo (TSE) sequence for breast morphology.
- **Slice positioning**:
  - Patient measurement: tumor localization with the help of a radiologist.
  - Volunteer measurement: the slice should intersect the mammilla to enable repeatable slice positioning.
- **Shimming**: Set the adjustment volume within the gland/tumor and expand it to only just cover the mammary gland with as little adipose tissue as possible. Avoid including

the pectoral muscle. An exemplary definition of the adjustment volume is depicted in Figure 5.7. During the shimming, the subjects should hold their breath for 25 s.

- **Estimation of breathing rhythm**: The natural breathing cycle induces periodic changes of the water frequency. The periodicity can be estimated by manually tracking the interactive shim for three to five respiratory cycles.
- **Adjustment of reference voltage amplitude**: Optimize B_1 iteratively using a fat saturated flip angle map (Siemens WIP sequence). The optimal voltage is usually overestimated by approximately 10 % in the presence of fat.
- **Test run of a CEST sequence**: Test the synchronization of the sequence to the breathing for about ten images.
- **CEST** with a nominal saturation amplitude of $B_1 = 0.9\,\mu\text{T}$
- **CEST** with a nominal saturation amplitude of $B_1 = 0.6\,\mu\text{T}$
- **T1 mapping**
- **WASABI**

The CEST measurements consisted of 75 unevenly sampled frequency offsets[9]. Saturation was achieved by 297 Gaussian-shaped pulses of duration $t_p = 15\,\text{ms}$ and $DC = 80\,\%$. The total saturation time was 5.6 s, leading to a total duration of 6 s per offset including imaging. This matched the breathing cycle of the majority of the examined women. In some cases of a longer period, a recovery time prior to the saturation pulse train was set to enable synchronization (i.e. $t_{rec} > 0\,\text{s}$). The total measurement time including positioning and shimming was approximately 40 min.

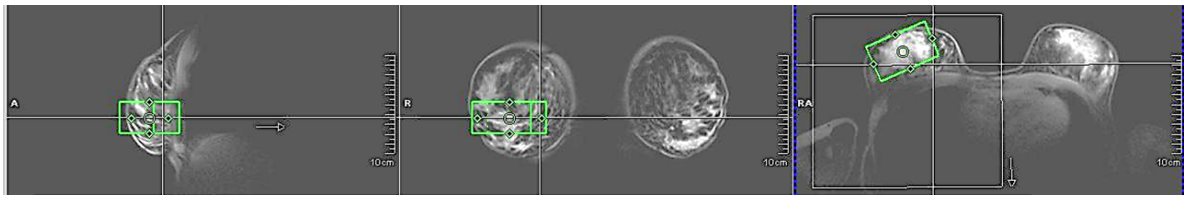

Figure 5.7: screenshot of the positioning of the adjustment volume (green). It should cover as little adipose tissue as possible and not cross the thorax.

[9] $\Delta\omega$ = 295, 300, 290, 100, 50, 20, 12, 8, 6.25, 5.25, 4.7, 4.4, 4.25, 4.1, 3.95, 3.8, 3.7, 3.6, 3.5, 3.4, 3.3, 3.2, 3.1, 3, 2.9, 2.75, 2.6, 2.45, 2.3, 2.15, 2, 1.85, 1.7, 1.55, 1.4, 1.25, 1.1, 0.95, 0.80, 0.70, 0.60, 0.50, 0.40, 0.30, 0.225, 0.15, 0.075, 0, −0.075, −0.15, −0.225, −0.30, −0.40, −0.50, −0.60, −0.70, −0.80, −0.95, −1.1, −1.4, −1.7, −2.2, −2.7, −3.0, −3.3, −3.7, −4, −4.7, −5.5, −7, −12, −20, −50, −100, and 300 ppm.

Table 5.3: Acquisition parameters of the 2D GRE sequence used for the standard *in vivo* CEST protocol.

matrix size	128 x 116 pixel
field of view	196 x 174 mm^2
slice thickness	5 mm
slice orientation	transversal
phase encoding direction	anterior - posterior
acquisition bandwidth	1220 $\frac{Hz}{pix}$
k-space ordering	centric out
RF pulse type	fast
gradient mode	fast
repetition time (TR)	3.7 ms
echo time (TE)	2.04 ms

5.10 Post-processing workflow

The post-processing workflow and data analysis had to be adapted due to the methodological developments. For clarity, it is listed in the following:

1. Save the raw data files of the CEST, WASABI, and T1 sequences.
2. Reconstruct the images employing an adaptive combination algorithm (cf. Sec. 5.3). The reconstruction incorporated a phase-unwrapping algorithm that resulted in a phasing of $\vec{S}_0$. The optimal set of coil weightings was calculated on the first acquired image and applied to all offsets within one experiment. Thereby, the phase of the water signal was kept constant for all frequency offsets $\Delta\omega$ and Equation 4.4 holds.
3. Perform a fit on WASABI and T1 sequence to obtain the field maps and the T1 map.
4. Normalize the CEST data conventionally to obtain Z-spectra (Eq. 4.8).
5. Apply the novel normalization (cf. Sec. 4.2):
   - Compute $\vec{F}_0$ in each voxel (Eq. 4.9). This can be achieved in two ways in order to account for B_0-inhomogeneities:
     - Determine $\vec{F}_0 = \vec{S}(\Delta\omega_{B_0})$ with $\Delta\omega_{B_0} = 0\,\text{ppm}$ utilizing a B_0 map. The map can be retrieved internally from a multi-pool fit of the conventional Z-spectrum or from a WASABI measurement.
     - Determine $\vec{F}_0 = \vec{S}(\Delta\omega_{min})$ at the frequency offset where the real part of the acquired images around the direct water saturation (DS) is minimal:

$$\Delta\omega_{min} = \underset{\Delta\omega\in[-1,1]\text{ppm}}{\arg\min} \; \Re\left(\vec{S}(\Delta\omega)\right) \tag{5.14}$$

   - Perform the fat-corrected CEST normalization (Eq. 4.12).
   - Calculate the fat fraction *FF* (Eq. 4.10). Knowledge of the FF supports data interpretation and can be utilized for a semi-automated segmentation of the gland.
6. CEST evaluation (cf. Sec. 5.7):
   - The signals of exchanging amide (and amine) protons fulfill *assumption 3*. CEST signals are isolated by the multi-pool fit.

- Calculation of the relaxation-compensated contrast, $AREX_{amide}$, and correction for B_1-inhomogeneities.

Segmentation of the mammary gland

Breast morphology varies in each woman. Two approaches were followed to segment the gland from adipose tissue:

1. Manual segmentation.
2. Semi-automated segmentation: First, the breast is pre-segmented manually from background and the pectoral muscle. Then, voxels exceeding a fat fraction of 40 % were excluded. Furthermore, voxels in regions of high B_1-inhomogeneities were excluded (i.e. ±40 %).

Regions of interests (ROI) were drawn manually or, in the contrast analysis of healthy women, in an automated approach. Here, the thresholds for the above mentioned segmentation were lowered to 30 % and ±30 %, respectively, and the mask dilated by 1 pix.

6 | Results

The main results of this thesis are presented in the following chapter. First, the development of robust field and T1 mapping of the human breast is shown. Then, the development of the novel fat-corrected CEST normalization is demonstrated, enabling, for the first time, relaxation-compensated amide contrast in the breast. Finally, the findings of three patient examinations are presented.

6.1 Robust field and T1 mapping of the human breast at 7T

The goal of field mapping and determination of T1 is to perform relaxation compensation and to correct for transmit field inhomogeneities. Therefore, fat saturation was chosen to suppress lipid signals in the MR images. However, the built-in fat suppression of the GRE sequence was insufficient due to high SAR and scan time. This led to the development of a new fat suppression sequence, played out directly before image acquisition. Figure 6.1 compares a fully relaxed in-phase image ($|\vec{S}_0|$) with two fat-saturated ones acquired in the breast of a healthy woman. Fat appears bright in GRE images, which prohibits an easy identification of the mammary gland in the unsaturated case (Fig. 6.1A). Although fat tissue is sufficiently suppressed by the built-in fat saturation, the image quality and sharpness is reduced by induced stripe artifacts (Fig. 6.1B). These artifacts vanish if the developed fat saturation pulses are played out prior to image acquisition (Fig. 6.1C). The mammary gland is easily recognizable. This self-developed fat saturation outperforms the conventional technique and does not require changes of imaging parameters.

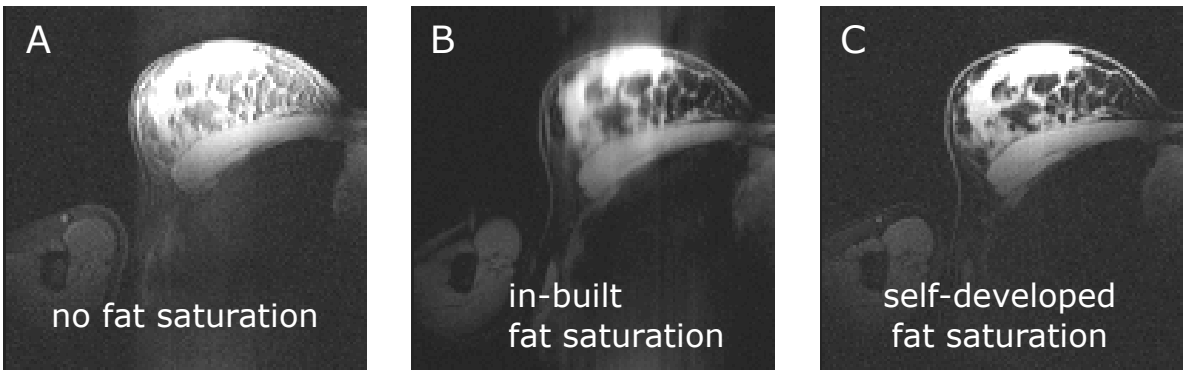

Figure 6.1: Fully relaxed images acquired in the right breast of a healthy volunteer are shown. (A): No fat saturation is applied. Due to the in-phase echo time and bright appearing fat signal, glandular tissue is not easily identifiable. (B): The standard built-in fat saturation sufficiently suppresses fat signal by the cost of an increased TR and SAR. Induced stripe artifacts reduce sharpness and image quality. (C): The developed fat saturation is superior to the standard one. Glandular tissue is clearly identifiable.

The interplay of water and fat signals in MR images is highly dependent on imaging parameters, especially the echo time (TE). Ideally, field mapping and T1 quantification should be independent on both the phase relation of water and fat as well as the fat fraction (FF). In the following, robust field mapping and T1 mapping with fat saturation is validated *in vitro* and *in vivo*.

6.1.1 Field mapping with fat saturation

The WASABI sequence enabled simultaneous mapping of B_0 and B_1. The same GRE imaging as the CEST measurements ensured comparability and avoided the need for registration.

In vitro verification

A phantom experiment with cream was perform to investigate the interplay of water and fat after preparation in a WASABI sequence. Cream has a fat content of roughly 30 % and its lipid resonances are comparable to human fat in the breast (cf. Figure 4.1).

The comparison of highly resolved WASABI spectra with and without fat saturation (see Figure 6.2) demonstrates the necessity for fat saturation. The measurements were repeated for various TE, covering one full cycle of water and fat. The spectra were averaged in regions of low and nominal B_1 (upper and lower row, respectively). Non-fat-saturated spectra (Fig. 6.2 A&C) show a strong dependence on the chosen TE and do not appear symmetric, thus prohibiting a reliable fit. High deviations are observable at $\Delta\omega = 0\,\text{ppm}$ as well as around $\Delta\omega \approx -3.5\,\text{ppm}$,

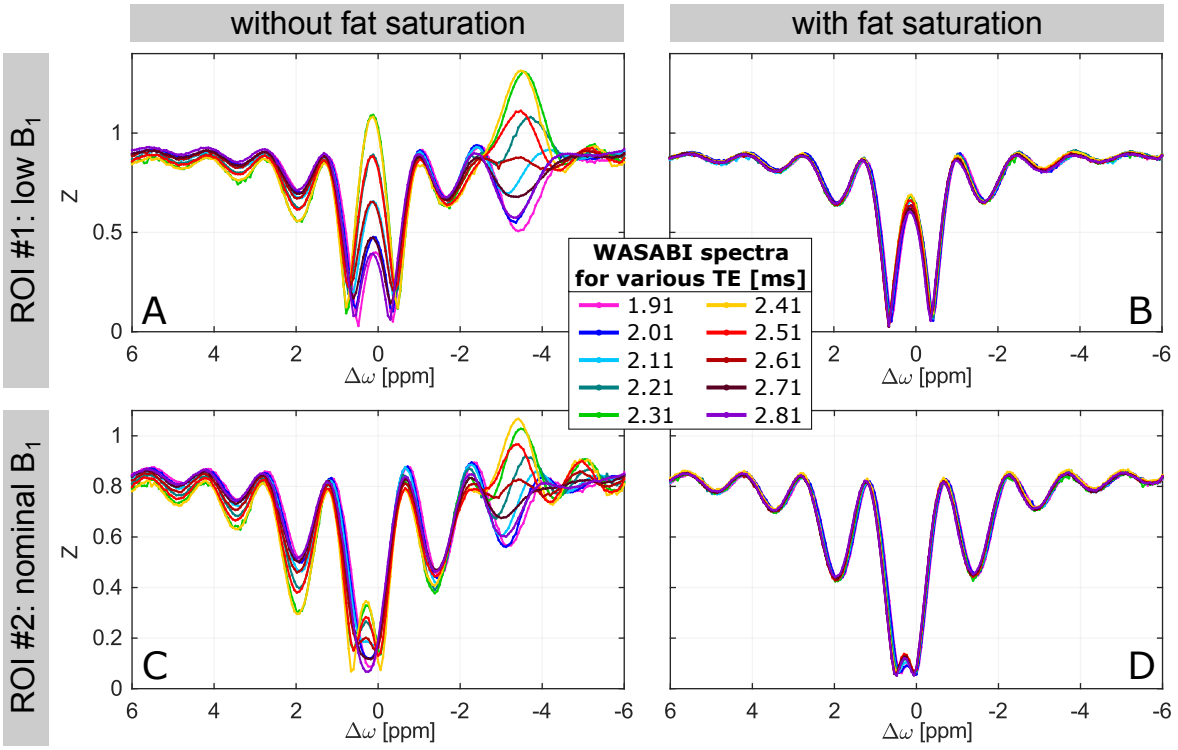

Figure 6.2: Comparison of highly resolved WASABI spectra with and without fat saturation. The spectra were obtained in cream (30 % fat content) with varying TE. Spectra were averaged in regions of low (A&B) and nominal (C&D) B_1 (cf. Fig. 6.3 A for ROI definition). The non-fat-saturated spectra depend strongly on TE. WASABI spectra are symmetric and overlay, if the fat saturation pulses were played out.

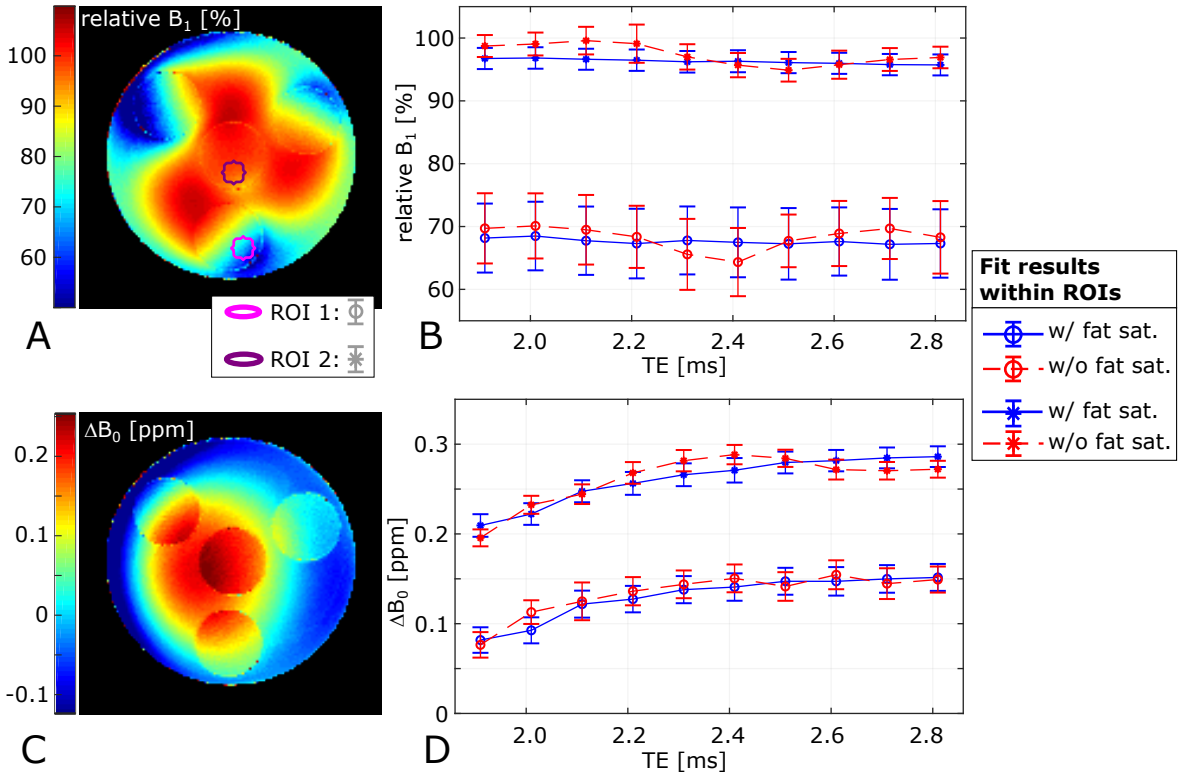

Figure 6.3: Exemplary field maps obtained with fat saturation (TE = 1.91 ms, (A): relative B_1 map, (C): ΔB_0-map). The fit results of relative B_1 are shown in (B). As expected from the TE-dependence of WASABI spectra (Fig. 6.2), the fit results depend on TE as well, if no fat saturation is applied. The effect is less prominent for ΔB_0 (D), as the symmetry axis of the WASABI spectra is less affected by superposing oscillations. The observed ΔB_0-drift is explainable by the long measurement time of the whole experiment (several hours).

where the dominant methylene (CH_2) peak resonates. For opposed-phase TE, Z-values above 1 occur. After fat saturation, all spectra overlay and no overlaying oscillations are observable (Fig. 6.2 B&D), thus enabling a robust fit.

All spectra were fitted in order to compare the influence of the lipid induced deviations on the field maps (Fig. 6.3). This smooth fat-saturated B_1 map shows the ROI definition used in the previous figure (Fig. 6.2). The outcomes for the relative B_1 values are independent of TE after fat saturation, but non fat saturated spectra result in B_1-deviations of roughly $\pm 5\,\%$(Fig. 6.3 B). The difference in ΔB_0 results obtained with and without fat saturation are only noticeable in a region of higher B_1. The position of the symmetry axis of WASABI spectra, i.e. ΔB_0, is less affected by superposing lipid signals. Additionally, a ΔB_0-drift is observed in Figure 6.3 D. It is explainable by the long measurement time of the whole experiment (several hours) and an actual drift of the scanner frequency.
The developed fat saturation sufficiently suppresses lipid signals enabling robust field mapping *in vitro*, despite B_1-inhomogeneities and the high fat fraction. It is furthermore independent on the phase of water and fat.

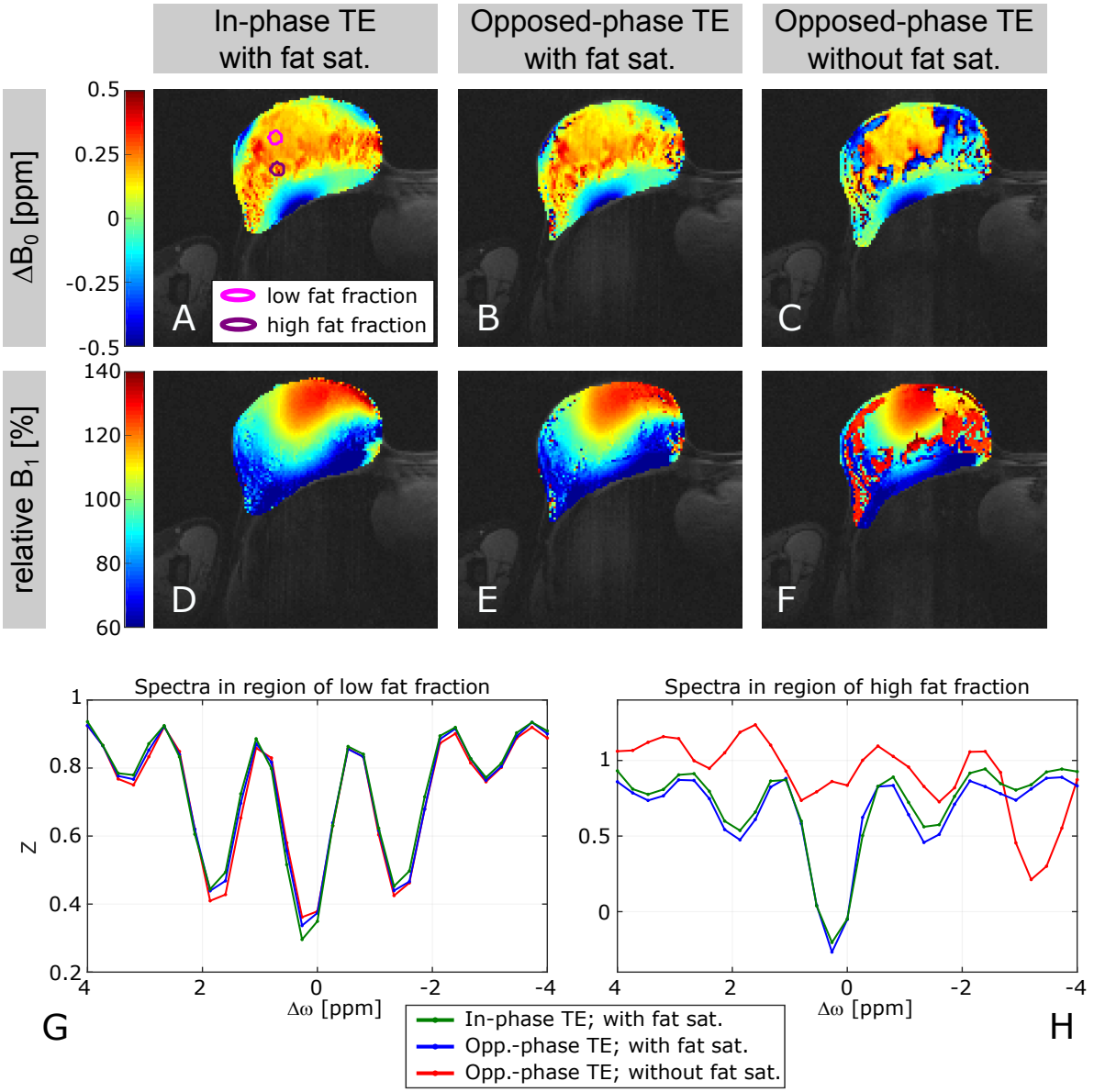

Figure 6.4: Field maps obtained in the right breast of a healthy volunteer for the special cases of in- and opposed-phase echo times (upper row: ΔB_0, lower row: relative B_1). Robust field mapping of the whole breast is enabled, if the fat saturation is applied. High deviations are observable in the non-fat saturated case (C&F). Due to the low fat content in the gland of the healthy volunteer, these deviations are mainly observable outside the gland (G&H).

In vivo verification

In order to verify the applicability of a fat saturated WASABI sequence, the two special cases of in- and opposed-phase TE were tested in a healthy volunteer with fat saturation applied. Additionally, one measurement without fat saturation was performed for the opposed-phase case. In order to match the breathing rhythm of the volunteer, the recovery time was adjusted to 5.6 s (see Sec. 5.9). This ensured sufficient synchronization of the sequence and only minor movements were observable within the images. Fat saturated B_1 and ΔB_0 maps closely resemble each other for both in- and opposed phase maps (Fig. 6.4 A&B and D&E, respectively). The field maps can be obtained in the whole breast despite high fat fractions. The non-fat-saturated maps show high deviations, mainly in fat dominant voxels, but yield

comparable results in the center of the gland (Fig. 6.4 C&F). This result is explainable by a look in the actual acquired spectra: Due to low fat content within the gland, spectra of all three measurements overlay (Fig. 6.4 G). However, in fat dominant regions only the fat saturated spectra overlay, while the unsaturated WASABI spectrum is strongly affected by lipid signal (Fig. 6.4 H). These results verify the applicability of fat saturated field mapping in the human breast by means of a WASABI sequence.

6.1.2 T1 mapping with fat saturation

This fat saturation method was programmed modularly and was therefore also combinable with a saturation recovery sequence. Its suitability for robust T1 mapping in the human breast is demonstrated in the following sections.

In vitro verification

The same cream-containing phantom was used to test the influence of TE on the measured T1 relaxation times. T1 maps of homogeneous phantoms were acquired with and without fat saturation (Fig. 6.5). The relaxation times in the four cream containing vials are equal, despite the B_1-inhomogeneities in the container (cf. Fig. 6.3 A). Furthermore, the obtained T1 values are independent of TE (blue curve in Fig. 6.5 B). In contrast, T1 values obtained without fat saturation depend strongly on TE (red curve). Deviations are maximal when lipid signals oppose the water signal.

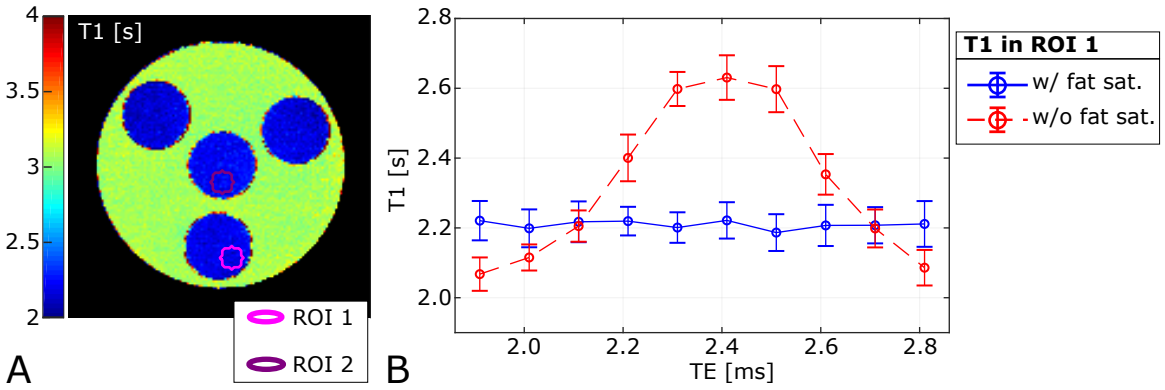

Figure 6.5: Comparison of T1-mapping with and without fat saturation in cream. (A): The T1 map obtained with fat saturation in the phantom is homogeneous. (B): The observed relaxation time depends strongly on the chosen TE, if no fat saturation is applied. The fat saturation enabled robust T1 mapping despite B_1-inhomogeneities and is independent of TE.

In vivo verification

Magnetization was measured at varying recovery times after complete signal saturation in a saturation recovery experiment. Hence, the whole sequence is not rhythmical, prohibiting a proper synchronization of the subjects' breathing to the sequence. Image acquisition occurs at different states of inhalation, causing a deformation and translation of the breast in the images. As described in Section 5.6, a waiting time was introduced prior to complete signal saturation. The introduction of a waiting time prolonged the acquisition time by a minute, but reduced motion of the breast significantly. The T1 map was measured in one patient with and without breathing synchronization and the gland's centroid position was tracked

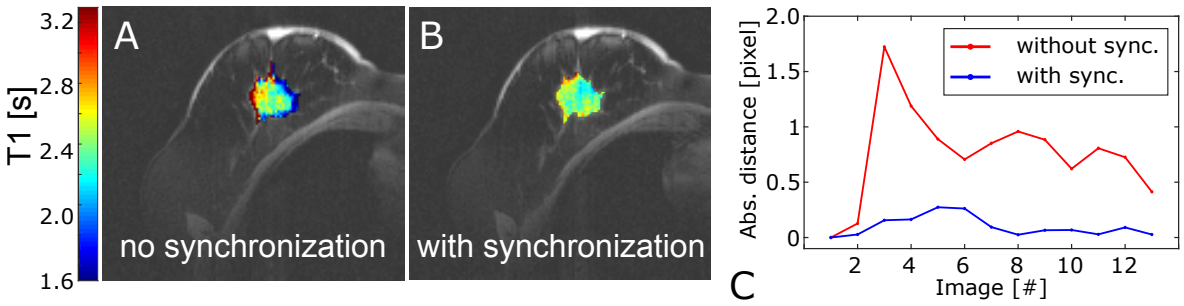

Figure 6.6: T1 maps acquired with and without synchronization of the sequence to the breathing of the examined patient (B and A, respectively). (C): The centroid of the gland was tracked for both cases. The introduced waiting time prior to signal recovery minimized the movement of the breast and ensured optimal T1 mapping. A shift of about 2 pixels for the non-synchronized case explains the artifact in the edges of the T1 map (A).

(Fig. 6.6). A shift of almost 2 pixels (equals 3 mm, approximately 10 % of the segmented gland diameter) was observed during the non-synchronized sequence. Consequently, an incorrect determination of T1 occurred (Fig. 6.6 A). T1 values at the medial edges of the segmented gland are underestimated while the lateral side of the gland appears overestimated. By adapting to the patient's breathing rhythm, almost no motion or deformation of the breast was observed and the relaxation time was successfully determined in the whole segment (Fig. 6.6 B).

To investigate a possible influence of the chosen TE, the saturation recovery sequence with fat saturation was tested in the breast of a healthy volunteer for the two special cases of an in- and opposed-phase TE. The according T1 maps are displayed in Figure 6.7. Both maps resemble each other closely. Averaged within the displayed segmented mammary gland, the T1 values are $T_{1,\ in-phase} = (2.30 \pm 0.25)$ s and $T_{1,\ opp.-phase} = (2.33 \pm 0.30)$ s. T1 mapping of the human breast is therefore independent of TE.

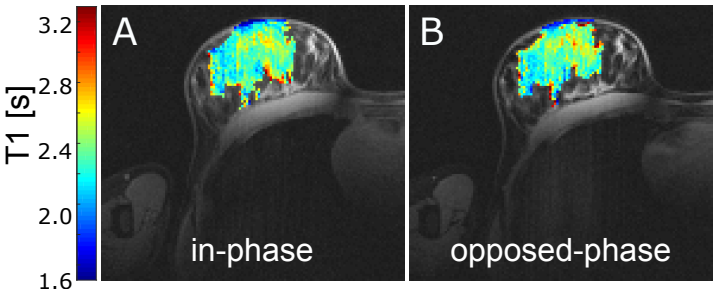

Figure 6.7: T1 maps acquired in the breast of a healthy volunteer. The images were acquired with fat saturation at an in-phase and opposed-phase echo time (A and B, respectively). The fat saturation enables robust T1 mapping in the human breast.

6.2 A novel normalization for CEST MRI to correct for fat-signal-induced artifacts

CEST MRI in the human breast is affected by the fat content in the fibroglandular tissue. Although the spectral region of amide proton resonances does not overlay with lipid resonances, the fat signals lead to an incorrect normalization of Z-spectra and thus to inaccurate CEST effects. A major part of this thesis was the development of a novel CEST normalization that corrects for fat signal contribution in the post-processing without the need for fat saturation schemes or water-fat separation. A comprehensive theory is given in chapter 4. The central points of the methods are:

- MR images detect a sum of the water and lipid signals ($\vec{S}_0 = \vec{W}_0 + \vec{F}_0$). This leads to an incorrect normalization in the conventional Z-spectrum:

$$Z_{conv}(\Delta\omega) = \frac{|\alpha(\Delta\omega) \cdot \vec{W}_0 + \vec{F}(\Delta\omega)|}{|\vec{W}_0 + \vec{F}_0|} \tag{6.1}$$

- The residual magnetization at $\Delta\omega = 0\,\text{ppm}$ represents the fully relaxed and collective fat signal, enabling to define a fat-only image:

$$\vec{F}_0 = \vec{S}(0\,\text{ppm}) \tag{6.2}$$

- Images obtained at offsets $\Delta\omega$ that do not coincide with lipid resonances can be corrected for fat signal contribution and the novel CEST normalization can be performed:

$$Z_{corr}(\Delta\omega) = \frac{|\vec{S}(\Delta\omega) - \vec{S}(0\,\text{ppm})|}{|\vec{S}_0 - \vec{S}(0\,\text{ppm})|} = \frac{|\vec{W}(\Delta\omega)|}{|\vec{W}_0|} = \alpha \tag{6.3}$$

Its experimental verification is provided in the following section.

6.2.1 In vitro verification

To verify the functionality of the proposed fat-corrected normalization, a carnosine model solution was prepared. Carnosine has a single exchanging amide proton resonating at around $\Delta\omega = 3.2\,\text{ppm}$. A steadily increasing FF was created by filling oil on top of the solution and placing the MR image slightly tilted at the interface. Five ROIs with increasing FF were defined and used for the further analysis (Fig. 6.8). The area marked by the overlaying white rectangle was used for the display of contrast maps shown in Figure 6.9. In this figure, Z-spectra and amide contrast maps that were obtained by the conventional calculation as well as by the novel method are compared (left and right column, respectively).

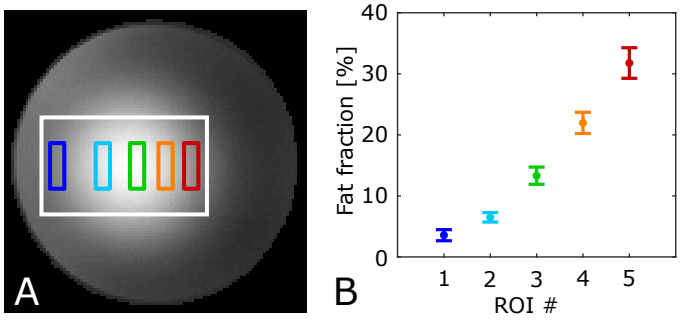

Figure 6.8: (A) MR image acquired in the oil-carnosine phantom. The tilted imaging plane created a fat fraction gradient. The defined five ROIs provide a steadily increasing fat fraction (B). The white rectangle represents the region used for illustration of contrast maps in Figure 6.9.

The evaluation for the special case of an in-phase relation of water $\vec{W}_0$ and fat $\vec{F}_0$ is illustrated in Figure 6.9 A-D. The amplitude of the amide resonance exhibits a strong FF dependence in conventionally obtained Z-spectra (Fig. 6.9 A). The amide signal decreases with increasing FF, while the residual magnetization at direct water saturation (DS, $\Delta\omega = 0\,\text{ppm}$) increases. This demonstrates that the amide signal is dependent on fat signal contribution, although no lipids resonate in the spectral region of the APT. This dependency vanishes in Z-spectra calculated by the novel normalization (Fig. 6.9 B). The amplitudes of the amide signal are independent of the FF. Per definition (Eq. 6.3), Z-spectra overlay at DS. The pseudo rNOE artifacts in the upfield spectrum at around $\Delta\omega = -3.5\,\text{ppm}$ can, however, not be corrected. Here, partial lipid saturation changes the phase and amplitude of $\vec{F}\,(\Delta\omega)$, which is a violation

of Assumption 3 (see Sec. 4). The remaining differences of fat-corrected spectra can be assigned to B_1-inhomogeities within the imaging slice. The amide resonance was isolated by a Lorentzian fit and compensated for relaxation and the $AREX_{amide}$ contrast was corrected for B_1-inhomogeneities. The contrast maps show a similar dependency on the FF (Fig. 6.9 C&D). While the conventionally obtained $AREX_{amide}$ values decrease with increasing FF, the fat-corrected $AREX_{amide}$ map appears homogenous.

For the second special case of an anti-parallel alignment of $\vec{W}_0$ and $\vec{F}_0$, the above described artifacts are even more prominent (Fig. 6.9 E-H). Amide signal dependence of amide signal on the FF is more pronounced, but increases with increasing FF. This effect is directly reproduced in the contrast map. Uncorrected Z-spectra further exhibit phase artifacts around $\Delta\omega = 0\,\text{ppm}$, where the residual magnetization flips and increases with FF. This is explainable by the underestimated denominator in the opposed-phase case of the CEST normalization (Eq. 6.1, [20, 63]). This underestimation also explains the pseudo rNOE artifact, which flips to Z-values greater than 1. On the contrary, spectra at $\Delta\omega = 0\,\text{ppm}$ and around the amide resonance overlay almost completely. The final $AREX_{amide}$ map is homogeneous (Fig. 6.9 H). Again, pseudo rNOE artifacts cannot be corrected.
The fat-corrected $AREX_{amide}$ values are not exactly the same (Fig. 6.9 J). This is thought to be caused by the long measurement time of several hours. However, the standard deviation within the ROIs is significantly decreased and for all FF of the same order. The amide contrast averaged within the ROIs based on conventional and corrected Z-spectra are listed in Table 6.1 and compared for the two above presented cases.
In order to prove the general applicability of the fat-correction approach for arbitrary phase relations of $\vec{W}_0$ and $\vec{F}_0$, the measurements have been repeated for various TE. Figure 6.9 I&J shows the comparison of the amide contrasts obtained from conventionally (I) and fat-corrected Z-spectra (J). The uncorrected $AREX_{amide}$ is dependent on both, TE and FF. The highest deviations among the ROIs are observed for the opposed-phase case (i.e. $TE_{opp.-phase} = 2.55\,\text{ms}$), which was analyzed in detail above. In contrast to the conventional approach, the developed fat-corrected normalization enables robust $AREX_{amide}$ quantification for up to 40 % FF and arbitrary phases between the water $\vec{W}_0$ and the lipid signals $\vec{F}_0$.

Table 6.1: Comparison of mean $AREX_{amide}$ values in carnosine with and without fat correction [10^{-2} Hz].

	conventional	fat-corrected
in-phase	3.51 ± 0.58	4.20 ± 0.08
opposed-phase	5.7 ± 1.6	4.50 ± 0.06

Figure 6.9: Z-spectra and amide contrast maps of the phantom experiment are compared for in- and opposed-phase echo times (TE = 2.04 ms & 2.55 ms, respectively. $B_1 = 0.8\,\mu\text{T}$). Left column: Conventional Z-spectra calculation (Eq. 4.8). The isolated amide signal and contrast decreased with increasing fat fraction (FF) for the in-phase case (A,C), but increases with FF for $\vec{W}_0$ and $\vec{F}_0$ being anti-parallel (E,G). After correction (right column, Eq. 4.12), the amide signal overlays in the Z-spectra and as well as at $\Delta\omega = 0\,\text{ppm}$ (B,F). The amide signal is independent on FF. The fat-corrected $AREX_{amide}$ maps are homogeneous (D,H). The experiment was repeated for various phase relations of water and fat by varying TE (I): The contrast depends strongly on TE and FF when calculated on conventionally obtained Z-spectra. After fat correction, the amide contrast is independent on both, phase of $\vec{W}_0$ and $\vec{F}_0$ and the FF.

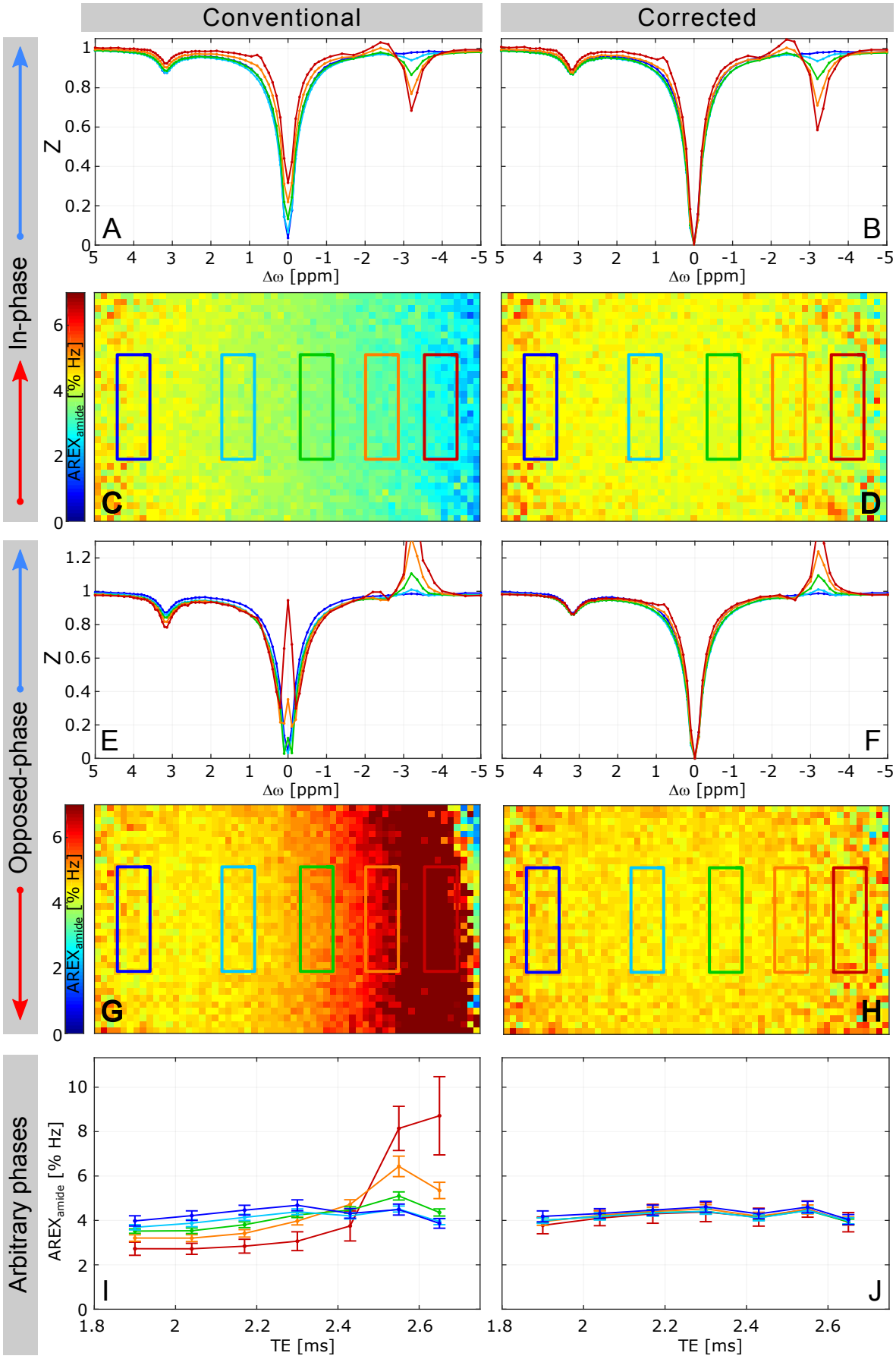

Figure 6.9: In vitro verification of the novel fat-corrected CEST normalization. Description on the previous page.

6.2.2 In vivo verification

In order to validate the correction approach for APT-CEST MRI of the human breast, a healthy volunteer was examined. Two complete CEST protocols were conducted subsequently with an in- and opposed-phase TE.

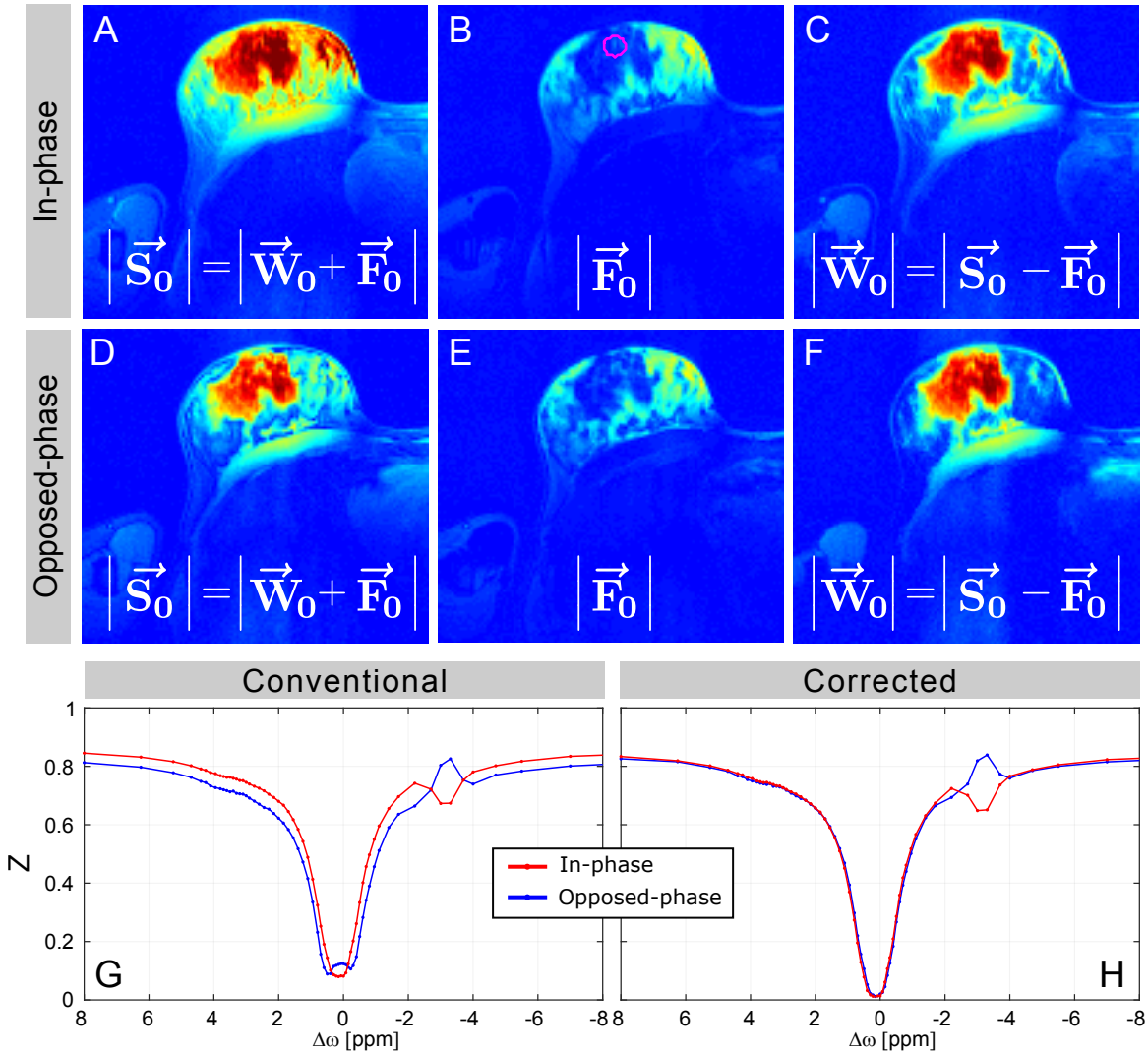

Figure 6.10: Magnitude of total ($|\vec{S}_0|$, A,D), fat-only ($|\vec{F}_0|$, B,E) and water-only images ($|\vec{W}_0|$, C,F) obtained in a breast of a healthy volunteer for the special cases of in- and opposed-phase TE (upper and middle row, respectively). Although the two $|\vec{S}_0|$ images differ, the calculated fat and water-only images resemble each other closely. Conventional Z-spectra (G, $B_1 = 0.6\,\mu T$) show the expected deviations in the spectral region of the APT and the direct water saturation (ROI definition in B). The fat-corrected Z-spectra (H) overlay in the spectral region of APT and the direct water saturation, thus verifying the applicability of the novel CEST normalization for *in vivo* examinations.

The $\vec{S}_0$ images show the expected differences of intensities: fat tissue appears darker in the opposed-phase case and regions of signal cancellation are observable (Fig. 6.10 A&D). As expected from the carnosine experiment, conventional Z-spectra averaged within the displayed ROI (Fig. 6.10 B) differ noticeably in the spectral region of the APT by an offset of the in-phase Z-spectrum (Fig. 6.10 G). Again, the DS ($\Delta\omega = 0\,\text{ppm}$) and the pseudo rNOE artifacts show the previously described TE dependent phase artifacts. Although the conventional Z-spectra differ at $\Delta\omega = 0\,\text{ppm}$, the fat-only images ($|\vec{F}_0|$) retrieved from the not-normalized image data

resemble each other closely (Fig. 6.10 B&E). The fat signal within the mammary gland is comparatively low, which is in line with expectations for a young and healthy woman. The calculated water-only images are very similar as well (Fig. 6.10 C&F). In addition, Z-spectra calculated by the novel normalization overlay in the spectral region of the APT and the DS (Fig. 6.10 H), demonstrating the general applicability of the method for *in vivo* examinations. As seen in the phantom experiment, pseudo rNOE artifacts are still present in both cases.

In order to obtain isolated amide contrast maps, a five-pool Lorentzian fit was performed on the in-phase data set. It was not, however, performed on opposed-phase spectra, as the phase artifacts of the DS and the pseudo rNOE prohibit a reliable fit. Conventional and corrected Z-spectra within a voxel in the gland are compared for two saturation powers (Fig. 6.11, B_1=0.6 µT & 0.9 µT). Z-values at $\Delta\omega = 0$ ppm do not drop to zero in both conventional spectra, independent on the saturation power (Fig. 6.11 A&C), indicating a FF of about 8 % within that particular voxel.
A clear amide signal as well as additional contributions from exchanging amine protons and MT from semi-solid structures are identified by the fit. The CEST effects resonate with respect to the water pool at around $\Delta\omega = 3.5$ ppm, $\Delta\omega = 2.2$ ppm, and $\Delta\omega = -2$ ppm, respectively. The fifth pool was fitted to the pseudo rNOE artifact, but represents rather a simplification to stabilize the overall fit ($\Delta\omega \approx -3.5$ ppm). A retrospective distinction between true rNOE effects and lipid signal induced artifacts is not possible. After the fat correction is performed, Z-spectra again go to zero (Fig. 6.11 B&D). The amide signal differs only slightly, which is expected due to the low fat fraction in that voxel. The increased saturation power leads and increased width and amplitude of the identified pools ($B_1 = 0.9$ µT, cf. Fig. 6.11 C&D), primarily the width of the water pool and the amplitude of MT. This is in line with the expectations from the CEST theory (cf. Sec. 3.2).

A closer look at the DS reveals a B_0-shift of the Z-spectra. As described in Section 5.7.2, no direct B_0-correction of spectra was performed within this work, as it would unnecessarily smoothen the data. B_0-inhomogeneities were however taken account for in each voxel by the application of the inverse metric. For *in vivo* CEST data presented in this thesis, an internal B_0 map was calculated from the center frequency of the water pool. This was preferred to the use of a B_0 map from the WASABI sequence in order to avoid potential displacement between CEST measurements and the WASABI due to subject movement.

The fat-corrected $AREX_{amide}$ maps were calculated for both saturation powers and displayed in the mammary gland (Fig. 6.12 A&B). Contrast obtained at a saturation power of 0.9 µT is increased compared to 0.6 µT and shows a correlation with B_1-inhomogeneities (the relative B_1map of the examination is shown in Fig. 6.4). Ventral AREX values near the mammilla are almost a two-fold increased from those of dorsal intensities. By interpolating between the two displayed contrast by utilizing the relative B_1 map, the contrast correction for B_1-inhomogeneities was performed (Fig. 6.12 C, see Sec. 5.7.4). This displayed contrast is homogenous and does not correlate to the B_1 map.

The impact of the developed fat correction becomes clear by comparing the final contrast maps (i.e. after B_1 correction), based on conventional and fat-corrected Z-spectra: The overall contrast intensity is slightly lower in the conventionally calculated contrast (Fig. 6.12 D). Contrast intensities decrease namely at the transition from glandular to adipose tissue, which can be explained by the higher fat content in those regions. The differences in the inner gland, with only little fat signal contribution, are competitively small.

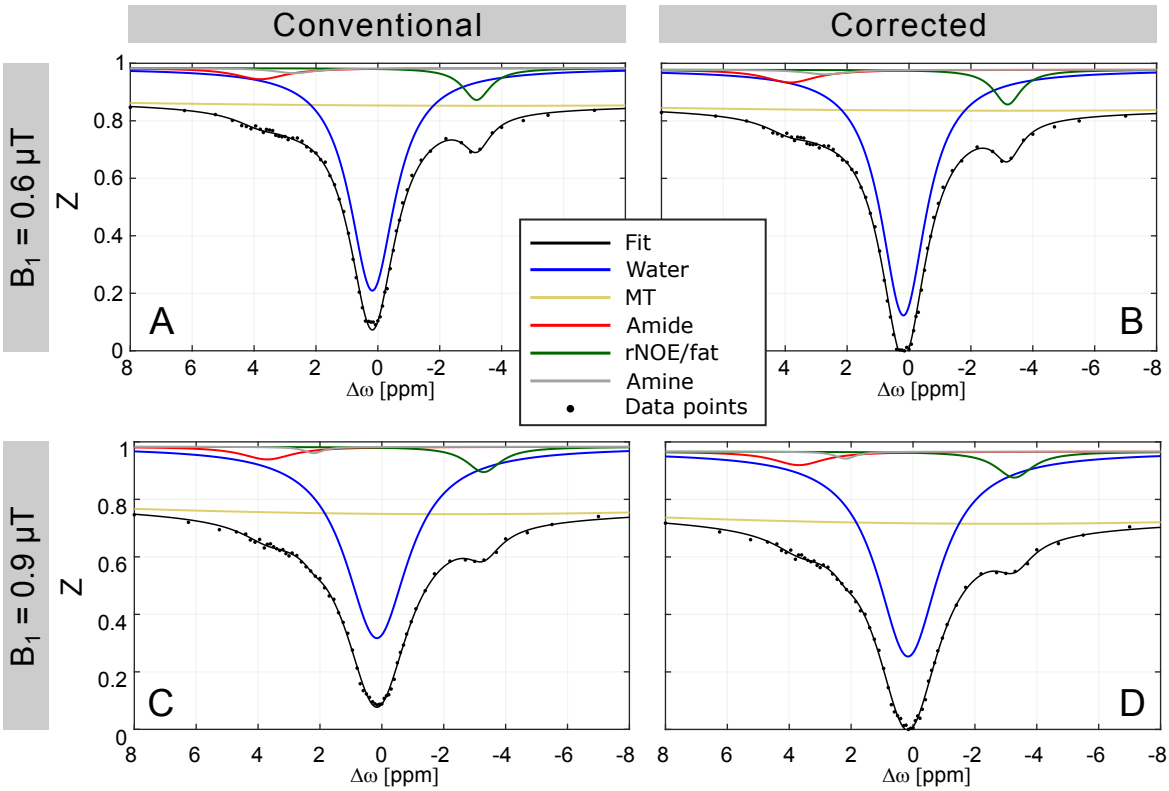

Figure 6.11: Conventional (A,C) and fat-corrected (B,D) Z-spectra are shown for two saturation powers (upper row: $B_1 = 0.6\,\mu T$, lower row: $B_1 = 0.9\,\mu T$). The spectra show the results of an exemplary voxel of an in-phase measurement (cf. Fig. 6.10, upper row). The results of the five-pool Lorentzian fit analysis is superposed in solid colored lines. Conventionally obtained Z-spectra show a residual magnetization of roughly 8 % due to fat signal contributions.

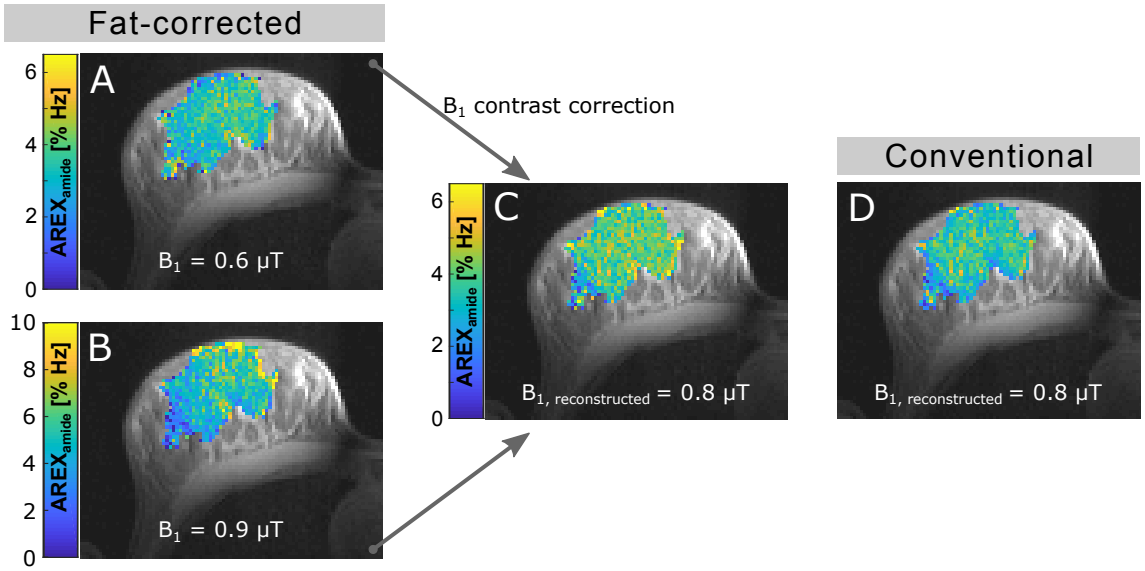

Figure 6.12: Visualization of the B_1-contrast correction in a healthy volunteer. The $AREX_{amide}$ maps of different saturation powers ((A): $B_1 = 0.6\,\mu T$, (B): $B_1 = 0.9\,\mu T$) were calculated on fat-corrected Z-spectra (cf. Fig. 6.11). The contrast appears homogeneous after application of the B_1 correction (C), especially when compared to the conventionally obtained CEST contrast (D), where the contrast decreases at the transition from glandular to adipose tissue.

6.2.3 Further optimization of saturation parameters and reproducibility

The novel fat-correction was successfully verified for *in vivo* examinations. The further optimization and test of reproducibility is described in the following.

Determination of the fat-only image $\vec{F}_0$

The core component of the novel CEST normalization is the post-processing based determination of a fat-only image $\vec{F}_0$ from CEST data itself, which enables the correction of the acquired MR images. As described in Section 4, the $\vec{F}_0$ can be obtained in two ways: the fat signal is either determined by a minimum approach in each voxel or by the utilization of a B_0 map. To investigate a possible influence on the the final contrasts, the data set presented in figures 6.10&6.12 was completely evaluated for both methods. To compare the post-processing itself, the B_0 map was calculated internally (cf. Sec. 5.5). The according $\vec{F}_0$ images, i.e. $|\vec{F}_{0,B_0}|$ and $|\vec{F}_{0,min}|$, look almost identical (Fig. 6.13 A&B, respectively). However, in some voxels intensity values of $|\vec{F}_{0,min}|$ are minimally lower (as expected, as it is a minimum based approach). This is also displayed in a map of a relative deviation overlaid in the gland ($|\frac{\vec{F}_{0,B_0}-\vec{F}_{0,min}}{\vec{F}_{0,B_0}}|$, Fig. 6.13 C). However, a small region of higher relative deviations can be identified. An effect on the final contrast, i.e. after fat and B_1 correction, is hardly visible (Fig. 6.13 D&E). The absolute difference shows no structure or any correlation to obtained maps or morphology (Fig. 6.13 F). Only some randomly distributed voxels are different. However, with respect to the mean intensity within the displayed segment, the overall contrast is about 2 % (i.e. $1 \cdot 10^{-3}$ Hz) higher in the AREX map based on $|\vec{F}_{0,B_0}|$. However, as this is within the detection limit, both methods for the determination of $\vec{F}_0$ are equivalent. Within this thesis, all displayed (other than in Fig. 6.13) and calculated contrast values are based on the minimum approach and $\vec{F}_{0,min}$.

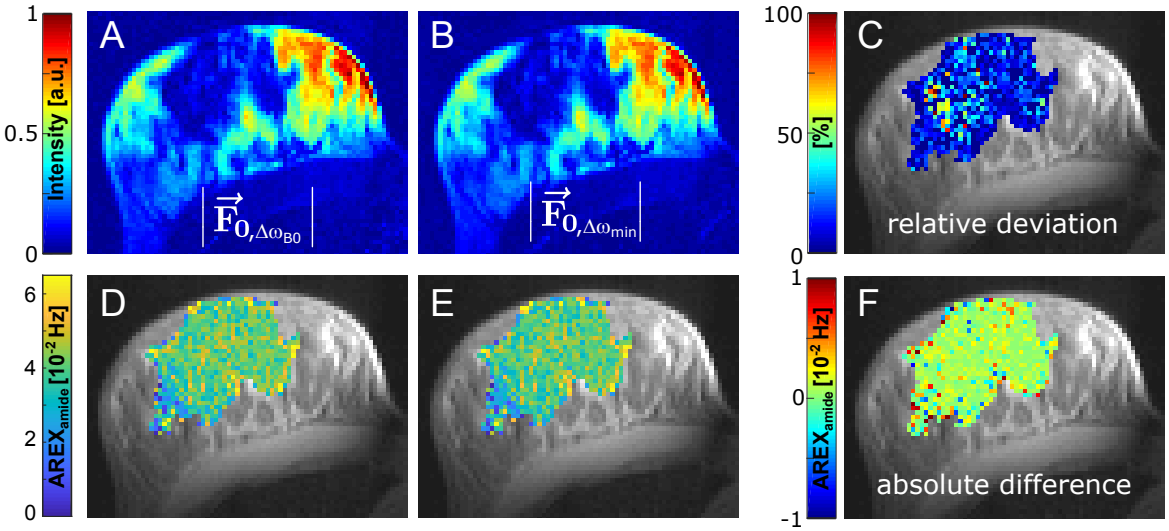

Figure 6.13: Effect of the determination of $\vec{F}_0$ on the final contrast. The fat-only images obtained by utilizing a B_0 map and by a minimum approach are almost identical (A&B), but relative deviations are observable (C). The final contrast maps generated by using $\vec{F}_{0,B_0}$ and $\vec{F}_{0,min}$ resemble each other (D&E, respectively). The absolute difference between the two contrast reveals no correlation to obtained field maps or morphology.

Effect of saturation pulse length in Z-spectra

It is known that saturation parameters such as the pulse length t_p influence Z-spectra and the CEST contrast [28, 44]. To find optimal settings for APT-CEST in the human breast, one healthy volunteer was examined with two different pulse lengths by keeping the DC constant (15 and 100 ms, Fig. 6.14 A). The shorter pulses provide a higher saturation efficiency and the Z-spectrum is minimally lower in regions of the APT, DS as well as at the pseudo rNOE artifact. Furthermore, the width of the DS appears broader. As the whole correction method depends on the residual magnetization at $\Delta\omega = 0$ ppm, the influence on the DS was investigated in more detail in another examination of high spectral sampling for various pulse lengths. Z-spectra of $t_p = 15$ ms, 25 ms and 100 ms show differences in the saturation profile (Fig. 6.14 B). Additional oscillations are superposed on the DS for shorter t_p, leading to deviations from an ideal Lorentzian line shape. Theoretically, optimal saturation transfer is yielded for $\gamma B_1 t_p \approx 180°$, which is fulfilled for the shorter pulses of $t_p = 15$ ms, which can explain an increased saturation efficiency. Furthermore, shorter pulses, are spectrally broader and introduce a kind of saturation plateau (Fig. 6.14 B). It is worth mentioning that differences in residual magnetization in the spectra can mainly be assigned to displacement/motion within the sequences. The assumption of complete water saturation at DS (cf. Sec. 4, *assumption 1*) should be independent of t_p and holds. The effects of pulse length on the amide contrast was included in the following reproducability study.

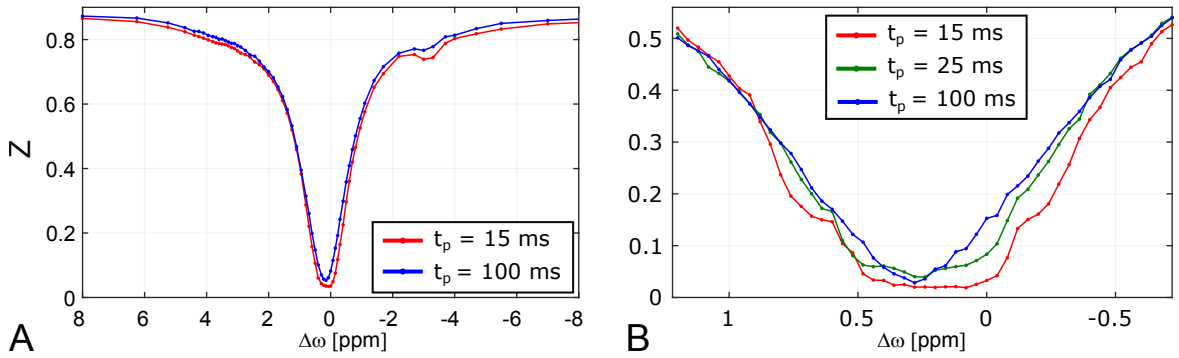

Figure 6.14: Effect of different saturation pulse lengths on Z-spectra. (A): The length of $t_p = 15$ ms shows a higher saturation efficiency than $t_p = 100$ ms. (B): Highly sampled Z-spectra around 0 ppm for varying pulse lengths t_p. Shorter saturation pulses are superposed by additional oscillations, but saturate with a broader spectral width.

Reproducibility study in a healthy woman

One healthy woman was repeatedly examined in order to test the reproducibility of the CEST protocol. The saturation pulse length was set to 100 ms. In four of the six examinations, the CEST sequences were repeated with $t_p = 15$ ms (cf. previous paragraph). Although the imaging plane was set intersect the mammilla as a reference point, repeated imaging of the exact same slice was prohibited (Fig. 6.15 A). Hormonal-induced morphological changes as well non-rigid deformations due to the positioning in the scanner caused the mammary to gland appear different in each examination. However, the fat-corrected amide contrast show reproducible values within the standard deviations. The four data points obtained with smaller pulses yielded slightly increased contrast values. Therefore, the pulse length was set to $t_p = 15$ ms for all further measurements.
The observed T1 values agree within their standard variations, but a slight increase over the course of measurements was observed (Fig. 6.15 C).

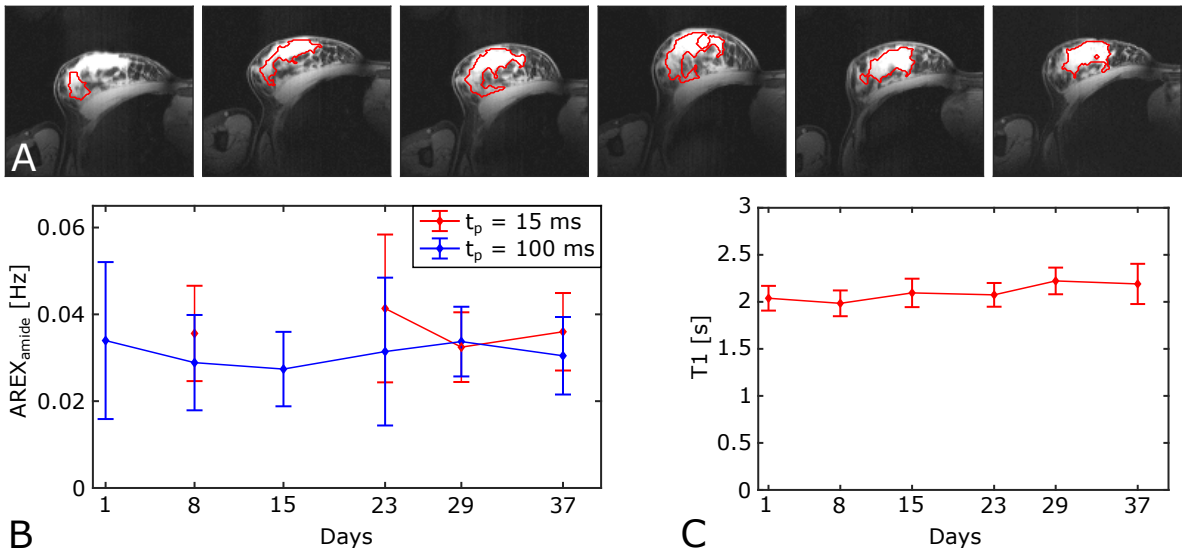

Figure 6.15: Reproducibility study of the CEST protocol in a healthy volunteer. The same volunteer was examined once a week for six times. Due to morphological changes of the breast as well as non-rigid deformation, repeated imaging of the exact same slice was prohibited (A). Nevertheless, the observed fat-corrected CEST contrast shows reproducible results (B). In four examinations, the CEST measurement was repeated with $t_p = 15\,\text{ms}$. $\text{AREX}_{\text{amide}}$values were slightly increased using the smaller saturation pulse width. Observed T1-values increase minimally over the course of the examinations (C).

6.3 Dependence of amide contrast on menstrual cycle

Breast parenchym undergoes hormonal induced changes during menstrual cycle (cf. Sec. 5.9.1). It is unknown whether periodic hormonal changes affect the amide CEST contrast, which could be indicated by the blue curve in Figure 6.15 B. A clinical study was initiated to investigate this question, for which the defined examination protocol is a result of the thus far presented developments.

So far, three healthy volunteers were examined and the fat-corrected, relaxation-compensated amide contrast obtained. Figure 6.16 A shows the amide contrasts averaged within the mammary gland. Although this represents only a snapshot of the whole study, no correlation of $\text{AREX}_{\text{amide}}$with the phase of the menstrual cycle (i.e. luteal and follicular phase) was found yet. The data acquired in the reproducability study (cf. Fig. 6.15 B, red curve) was also included. Contrast values agree within their standard variations. Thus, a reference value for the amide contrast in healthy, premenopausal women was defined. The mean amide contrast averaged over the ten data points over both hormonal phases is:

$$AREX_{amide,\ healthy} = (3.74\ \pm\ 0.46) \cdot 10^{-2}\text{Hz} \tag{6.4}$$

Also, no change in T1 between the two phases was detected in the three enrolled volunteers (Fig. 6.16 B). However, relaxation times determined in V1 are smaller and appear to not to be constant over the cycle.

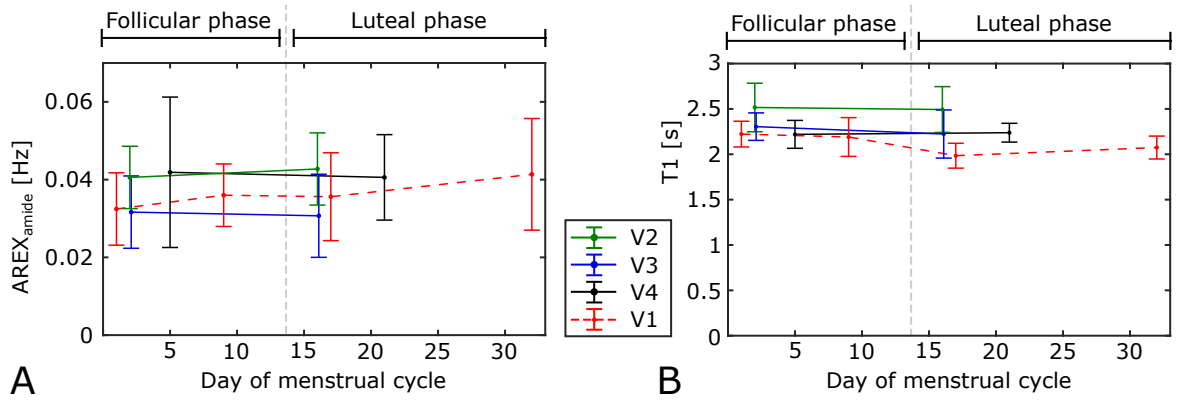

Figure 6.16: Dependence of the amide contrast on menstrual cycle (A). Three healthy women were examined twice in different hormonal phases. Additionally, the data set shown in Figure 6.15 was included. No clear correlation of CEST contrast with the examination day is observable. (B): Mean T1 values obtained in the small volunteer cohort.

6.4 Examinations of mamma carcinoma patients

For the first time, relaxation-compensated amide CEST was investigated in mamma carcinoma patients. In the following, the results of three patients that were examined by the developed CEST protocol within a clinical pilot study are presented.

Patient 1

In the first patient measurement no healthy tissue was present, as tumorous tissue covered the whole gland within the imaging slice. This is also visible in the anatomical image (i.e. T2-weighted, Fig. 6.17 D). The fat- and water-only images reveal that the tumor is embedded in adipose tissue (Fig. 6.17 A-C). The FF in the tumor is about 8 %, as suggested by the residual signal at DS in the conventional Z-spectrum (Fig. 6.17 E). Here, prominent CEST signals of amide and amine protons are identified by the multi-pool fit. The amplitudes are minimally increased by application of the fat-corrected normalization. Peak amplitudes are higher compared to Z-spectra obtained in healthy women (cf. Fig.6.11). As expected, the fat-corrected amide contrast is increased as well (Fig. 6.17 G&H). Averaged over the displayed gland, the final contrast is $AREX_{amide} = (8.8 \pm 2.4) \cdot 10^{-2}$Hz. An intra-subject comparison to healthy tissue is not possible. However, compared to the mean value obtained in healthy women, AREX$_{\text{amide}}$ is increased by a factor of 2.4.

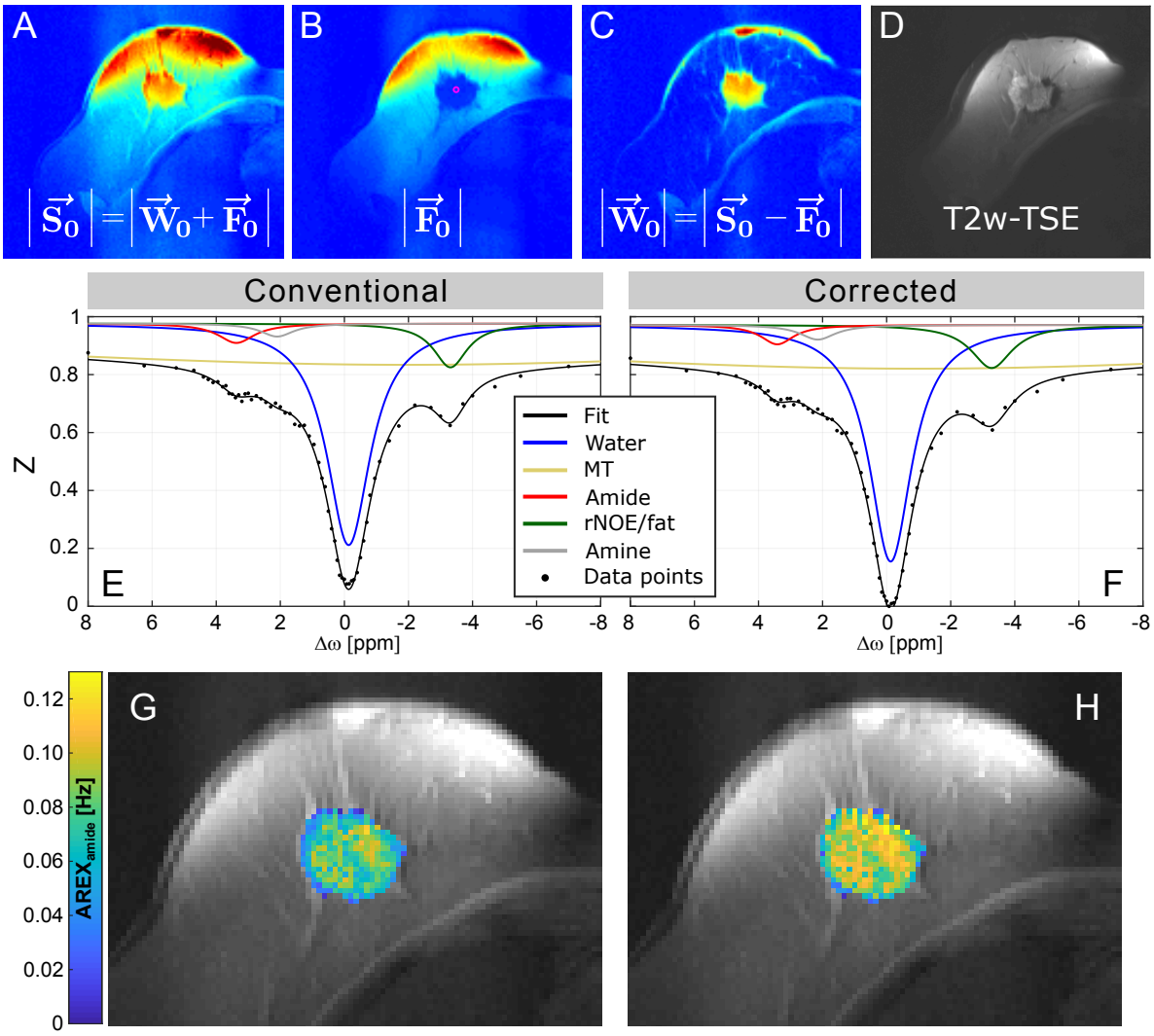

Figure 6.17: First application of relaxation-compensated amide CEST in a mamma carcinoma patient. (A)-(C): Magnitude of total ($|\vec{S}_0|$), fat-only ($|\vec{F}_0|$) and water-only images ($|\vec{W}_0|$), respectively. (D): Anatomical, T2-weighted image. A fat fraction of 8 % in the tumor is seen in the conventional Z-spectrum ((E), $B_1 = 0.6\,\mu T$, voxel marked in (B)). F: corresponding fat-corrected Z-spectrum. Conventional (G) and fat-corrected (H) AREX$_{amide}$ maps. Although a direct comparison is prohibited as the tumor covered the entire gland, an increase by a factor of 2.4 compared to the group of young healthy women was observed.

Patient 2

In the second patient examination, the tumor is clearly distinguishable from healthy glandular tissue. The breast showed only little signal fat contribution (Fig. 6.18 A-D). This is also visible in the conventional Z-spectrum that almost drops to 0 at DS (approximately 2 % fat fraction within the tumor, Fig. 6.18 E)). Hence, the conventional and fat-corrected AREX$_{amide}$ maps resemble each other closely, with only a minor increase of intensity in the corrected map (Fig. 6.18 H&I). The healthy tissue is in the order of the mean AREX$_{amide}$ determined in healthy women. Averaged within the two manually drawn ROIs, the obtained contrast values are $AREX_{amide,healthy} = (2.8 \pm 0.9) \cdot 10^{-2}$Hz and $AREX_{amide,tumor} = (8.4 \pm 0.9) \cdot 10^{-2}$Hz (blue and red ROI in Fig. 6.18 D, respectively). Within the examined breast, the observed amide contrast is three-fold increased in the tumor and increased by a factor of 2.4 when

compared to the group of healthy women. Furthermore, a prominent amine resonance was identified in tumorous tissue. The amine amplitude in the healthy mammary gland was comparable to the examinations in healthy women. Hence, the tumor is also clearly visible in the relaxation-compensated $\mathrm{AREX}_{\mathrm{amine}}$ map (Fig. 6.18 J). Although easily identifiable in the anatomical image, no contrast is seen in the T1 map of the examined breast (Fig. 6.18 D&F). Unfortunately, due to SAR restrictions within the measurement, the reference voltage of the scanner could not be further increased. This resulted in low relative B_1 values within the comparatively small breast (Fig. 6.18 G). However, the B_1 contrast correction worked in the region displayed in the CEST maps.

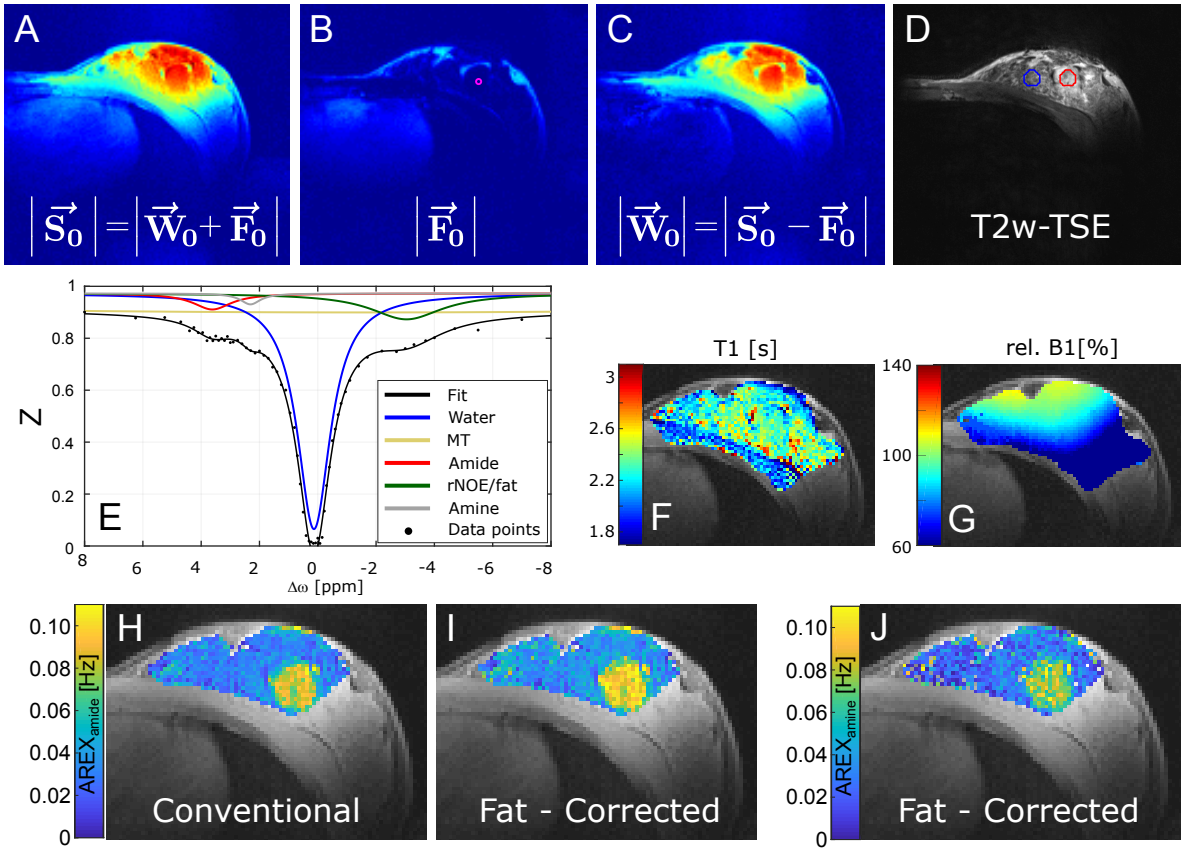

Figure 6.18: Patient 2 with an invasive ductal carcinoma in the left breast, clearly distinguishable from surrounding healthy tissue. Due to a low fat signal, the conventional Z-spectrum almost drops to 0 at $\Delta\omega = 0\,\mathrm{ppm}$ (E; exemplary voxel marked in fat-only image, B). Hence, conventional and fat-corrected amide contrast are very alike (H&I). $\mathrm{AREX}_{\mathrm{amide}}$ values in the tumor are a three-fold increased compared to the surrounding healthy tissue (red and blue ROI in D). Interestingly, relatively strong signals of amine resonances were identified, leading to a clear distinction of the tumor in the $\mathrm{AREX}_{\mathrm{amine}}$ map (J).

Patient 3

The mammary gland examined in the third patient showed varying fat content (Fig. 6.19 A-C). Connective regions with fat fractions of about 20 to 30 % are present in the FF map (Fig. 6.19 E). In the conventional amide map, an apparent structure of increased intensity is present, although not as differentiated as in patient 2. The fat-corrected $\mathrm{AREX}_{\mathrm{amide}}$ map however shows less heterogeneity (Fig. 6.19 G). The apparent contrast in the conventional case was induced by fat-signal contribution.

Based on the clinical report, the tumor is located in the lower left with respect to the imaged slice. A distinctive segmentation solely based on the T2-weighted image (Fig. 6.19 D) is not possible without further clinical MR images, diagnostics from mammography, and/or support by a professional radiologist. Also, the final amide maps shows no distinctive structure, prohibiting a safe contrast comparison of healthy and tumorous tissue. However, the overall $\mathrm{AREX}_{\mathrm{amide}}$ is increased compared to healthy women, approximately by a factor of 2. This examination demonstrates that the developed correction method might improve the specificity of amide CEST in tissues with varying fat content, as the fat signal induced artifacts could be misinterpreted otherwise.

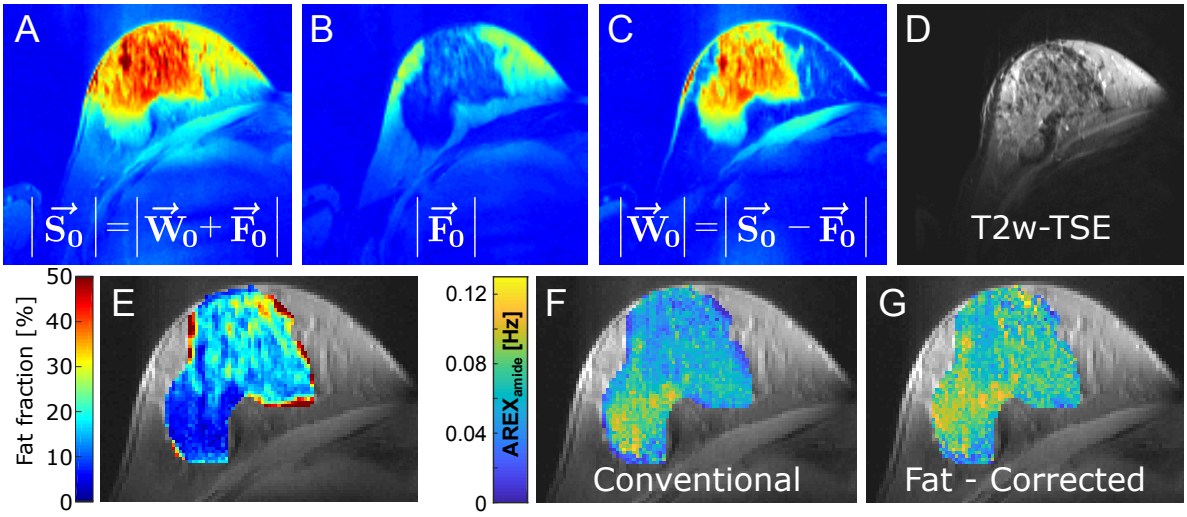

Figure 6.19: Varying fat signal contribution was present in the mammary gland of patient 3, leading to increased fat fractions (E). The apparent structure of increased intensity in the conventional $\mathrm{AREX}_{\mathrm{amide}}$ map (F) becomes less heterogeneous after fat correction is applied (G). A distinctive tumor segmentation based on the TSE-image (D) is not possible without further clinical data. The overall contrast is however increased compared to healthy tissue.

7 | Discussion

CEST MRI is an emerging field with increasing interest for application in other organs than the human brain. Application in the human breast appears especially promising, as it may correlate to chemotherapy response [14, 64, 81, 82] or tumor histology [15, 65, 83]. However, no studies have been performed in the human breast that have isolated CEST effects by correcting for known biases, such as spillover, T1 relaxation, and inhomogeneities of the saturation profile. Therefore, the aim of this thesis was to enable relaxation-compensated CEST MRI in the human breast.

MR imaging of the mammary gland is affected by lipid signal contribution of adipose tissue, consequently leading to an incorrect CEST normalization and misleading artifacts in the Z-spectrum [20, 63]. In this work, a general description explaining the interplay of water and lipid signals, hence the origin of fat-signal-induced artifacts in Z-spectra, is formulated. A novel normalization was developed to allow the correction of fat signals in post-processing, hence the isolation of amide CEST signals. The development of robust field and T1 mapping enabled — for the first time — relaxation-compensated amide CEST imaging of the human breast to be corrected for field inhomogeneities. An examination protocol was set up to investigate fat-corrected amide CEST in a clinical context.

7.1 Breast imaging at 7T

The human breast is a deformable organ, which presents a challenge for MR acquisitions at high fields. Three aspects were introduced to ensure a successful run of the examination protocol:

First, examined women wore scrubs during the examinations. The fabric provided support and prevented a free hanging of the breast into the "open bucket" breast coil array. This increased the overall comfort for the women and significantly reduced motion and deformation. Some studies utilized a mattress for this purpose [67] or benefited from a cup-like coil design [68].

Second, the unilateral imaging of only one breast improved two things: The B_0-shimming improved significantly when performed on a single mammary gland, leading to an increase in SNR. Furthermore, the field of view was reduced and thus image acquisition shortened to 400 ms. This is especially advantageous for CEST MRI, as the initial magnetization ($|\vec{S}(\Delta\omega)|$) recovers to an imaging steady state during acquisition, hence diminishing the CEST contrast for longer acquisition duration [84]. Unilateral breast imaging was also preferred in previous CEST studies [64, 67, 68].

Third, synchronization of the sequence to the subject's breathing cycle. Breathing-induced chest motion presented the main obstacle. Repeated breath-holds were unacceptable, as

the acquisition of about 200 images during the CEST protocol was too demanding. Here, the solution was the synchronization of the sequences to the natural breathing rhythm, which increased the overall measurement time to about 20 min. The duration of the overall measurement protocol is still similar to recent CEST MRI examinations of the brain at 3 T [85]. The breathing synchronization worked well and only minimal deformations of the breast were observed. Spatial displacements between the sequences were also minor, in some cases in the order of ≈ 1 pix. Next to imaging artifacts, the chest motion induces periodic changes of B_0 [86]. Fluctuations of up to ± 60 Hz per breathing cycle were observed (i.e. ≈ 0.2 ppm at B_0=7 T). The synchronization ensured that these B_0 changes did not affect the phase-sensitive imaging and occurred only during the CEST preparation. Although this proceeding still requires a cognitively demanding cooperation, it was perceived acceptably by patients and healthy volunteers. In the future, a respiratory belt might be deployed in order to achieve an even more robust synchronization that is independent of subject cooperation [87].

7.2 Field and T1 mapping with fat saturation

The TE-dependent interplay of water and fat signals effects MR images and thereby falsifies quantitative measurements of T1 relaxation time as well as field mapping sequences. The AREX contrast scales linearly with the longitudinal relaxation time of water and is thereby directly affected by uncertainties in the determination of T1. Therefore, robust and generally applicable T1 mapping was a prerequisite for the relaxation-compensation of the determined CEST contrast. Equivalently, as CEST effects depend on the irradiation amplitude and are thereby affected by inhomogeneities of B_1, robust B_1 mapping was required for the contrast correction. To achieve this, a fat-saturation-based approach was chosen. However, the built-in fat saturation of the GRE sequence itself was not applicable, as it prolonged the image acquisition by one second, increased the SAR, and induced blurring. The self-developed fat saturation block, consisting of five spoiled Gaussian-shaped 90° pulses, was played out directly before the image acquisition. It outperformed the built-in fat saturation in image quality, acquisition duration, and SAR. Due to the centric-reordered image acquisition, lipid signals have to be already saturated before the first k-space line acquisition. Lipid saturation was sufficiently ensured by the fat saturation block, although it mainly suppressed the dominant methylene peak ($\Delta\omega = -3.4$ ppm).

Robust and TE-independent T1 mapping was feasible for both *in vitro* and *in vivo* application. With respect to *in vivo* application, the overall importance of breathing synchronization is emphasized. Due to the arrhythmical succession of the saturation sequence, considerable motion and deformation of breast tissue was observed prior to synchronization. The introduced waiting time ensured the synchronization of the saturation recovering sequence to the breathing.

The WASABI sequence presented the best candidate for field mapping as it provides mapping of both B_0 and B_1 and finds more and more application in the CEST field [85, 88, 89]. In combination with the fat saturation, robust and TE-independent results were ensured. However, effectively only the B_1 map was used for calculations. The B_0-corrected AREX calculation utilized an internally calculated B_0 map. This post-processing-based approach was preferred, as it avoids a potential displacement between the CEST and the WASABI sequences. B_0 maps obtained in the human breast are heterogeneous and a small displacement might cause artifacts in the CEST contrast [89]. Motion correction and image registration would circumvent this displacement, but were not feasible for the single-slice approach applied in this thesis. On the other hand, B_1 maps appear smooth and are less affected by tissue composition than by the

coil setup itself [19]. Thereby, a minimal displacement between the measurements was not as impactful on the final CEST contrast.
The duration of the WASABI measurement was approximately 4 min. The sequence could be replaced by shorter B_1 mapping methods in the near future. A fat-saturated dual refocusing echo acquisition mode (DREAM) sequence represents a good candidate [90] and would take less than half a minute. Another approach was suggested by van Rijssel *et al.*, in which B_1 is estimated by the use of a generic template for field-mapping of the human breast at 7 T[19]. Both methods would, however, require a 3D CEST imaging and image registrations.

7.3 Isolated amide CEST MRI of the human breast at 7T

CEST MRI in the presence of fat leads to an incorrect normalization, thus pseudo CEST effects [20] (cf. Fig. 4.4). Zhang *et al.* showed that Z-spectra are dependent on the TE and FF and explained fat-signal-induced artifacts in the MTR_{asym} contrast metric [63]. Within this thesis, it was demonstrated that amide signals in conventional Z-spectra are also affected by lipid signals and incorrect normalization (cf. Sec. 6.2). Furthermore, the isolated $AREX_{amide}$ contrast is dependent on the FF and TE. A framework was derived describing the interplay of water and lipid signals for arbitrary TE, hence arbitrary phases of water and fat (cf. Chapter 4). This framework allowed the definition of a novel CEST normalization that includes a fat-signal correction. The collective fat signal can be retrieved at the DS in Z-spectra in the post-processing. No additional measurements are needed for this approach. Lorentzian fitting enables the isolation of amide signals, which can then be corrected for T1 relaxation and B_1-inhomogeneities by the obtained field maps.

A novel normalization correcting for fat-signal-induced artifacts

The key finding of this novel normalization is that a fat-only image, $\vec{F}_0$, can be retrieved from the Z-spectra at the spectral position of the DS. $\vec{F}_0$, i.e. the collective sum of lipid signals of all ten resonances[1], facilitates the calculation of water-only images, $\vec{W}_0$. Other studies of CEST MRI of the human breast have applied fat saturation [14, 64] or water excitation [65, 67, 68] to reduce fat artifacts. Both these approaches eliminate the signal of the main lipid peak originating from methylene groups (CH_2, $\delta\omega = -3.4$ ppm). The lipid resonance at $\delta\omega = 0.6$ ppm and other peaks closer to the water resonance might be wrongly attributed as water signal. A potential impact on the amide contrast is conceivable. Zhang *et al.* was the first to combine a 3pt-Dixon water-fat-separation with CEST MRI of the human breast [15]. However, an asymmetry contrast metric (i.e. MTR_{asym}) was applied. As explained in Chapter 4, the partial saturation of lipids at $\Delta\omega = -3.5$ ppm leads to a misalignment of $\vec{F}_0$ and $\vec{F}(\Delta\omega)$. Consequently, there is potential bias on the MTR_{asym} contrast.

This proposed novel normalization presents a SAR- and time-efficient alternative to fat saturation or water excitation schemes and does not require additional measurements (e.g. the acquisition of several echoes). All information needed is already obtained in the conventionally acquired Z-spectrum. Furthermore, the utilization of image-phase information provides general applicability for arbitrary phases of water and fat signals. Therefore, this approach is robust against field inhomogeneities.

This novel normalization is based on three assumptions (cf. Section 4.2): *Assumption 1* is complete water saturation at the spectral position of the DS. This is fulfilled by the long

[1] Ten lipid resonances were identified in ^{1}H-spectroscopy of the human breast at 7 T [31].

saturation of several seconds. Additionally, the relaxation of water is long compared to the image acquisition (about 2.3 s vs. 0.4 s, respectively). Water signal recovery during the short readout is thereby negligible and *Assumption 1* holds.

Assumption 2 is no partial lipid saturation at $\Delta\omega = 0$ ppm. This is only justified due to the low saturation power ($B_1 < 1.5\,\mu T$). If higher saturation amplitudes were chosen, partial saturation of lipids resonating close to the water could occur. Furthermore, the spectral width of the saturation pulses was small (≈ 0.2 ppm for $t_p = 15$ ms at B_0=7 T). A spectral broadening of breathing-induced fluctuations of B_0, which is up to ≈ 0.2 ppm per breathing cycle, would still not lead to a partial saturation of the prominent peak resonating around 0.6 ppm, which makes up to 10 % of the complete fat signal[2]. The second assumption is therefore also justified. However, caution is advised for the combination of high-power CEST approaches and this fat-correction approach. Using these two assumptions, one can determine the collective fat signal $\vec{F_0}$ by the residual magnetization at $\Delta\omega = 0$ ppm.

Assumption 3 is no partial lipid saturation in the evaluated spectral region of interest. This is fulfilled for the downfield and, in particular, for amide and amine resonances. Yet, this does not hold true for frequency offsets coinciding with lipid resonances. Under the third assumption, one can correct images for fat-signal-contribution by subtracting $\vec{F_0}$. However, pseudo rNOE artifacts cannot be corrected by this fat correction since *Assumption 3* is violated.

This method can be applied for fat fractions of up to approximately 40 %. The main limiting factor for higher FF is the reduction of SNR in fat-dominant voxels. Yet, this is no drawback: the CEST contrast mechanism is solely dependent on the water signal, which supports the exclusion of fat-dominant voxels from the analysis in the mammary gland.

Optimization and parameter choices

An in-phase TE was chosen for all quantitative examinations, although the general formulation of the fat-corrected normalization allowed arbitrary TE. The multi-pool fit showed a better performance with in-phase Z-spectra, particularly at the DS and the pseudo rNOE peaks. Furthermore, the overall SNR increased due to the parallel alignment of water $\vec{W_0}$ and fat $\vec{F_0}$. It is worth mentioning that an in-phase TE already minimizes the lipid-induced artifacts in the conventionally calculated $\mathrm{AREX_{amide}}$ contrast (cf. Fig. 6.9). Application of the novel CEST normalization is nevertheless advised due to a high inter-subject variability of the FF. Moreover, the in-phase condition does not hold in the whole gland due to field inhomogeneities (cf. Fig. 2.6), which are particularly increased in larger breasts with high amounts of fat. The novel CEST normalization accounts for B_0 inhomogeneities by a voxel-wise determination of $\vec{F_0}$and is robust for arbitrary phase relations of water and fat signals.

Shorter saturation pulses ($t_p = 15$ ms) were preferred to longer ones ($t_p = 100$ ms), since they provided a higher saturation efficiency. Theoretically, optimal saturation transfer is yielded with $\gamma B_1 t_p \approx 180°$ saturation pulses, which is fulfilled for the shorter pulses of $t_p = 15$ ms at the chosen $B_1 \approx 0.8\,\mu T$, thus explaining the increased saturation efficiency. A train of shorter and spectrally broader RF pulses is also advantageous as it overcomes effects of breathing-induced B_0-fluctuations [67]. However, the 15 ms pulses introduce a kind of saturation plateau (see Fig. 6.14 B). In the future, the multi-pool fit could be adapted to account for this by introducing a constant plateau into the Lorentzian line of the water [85, 91]. This will, however,

[2]The amplitude of the downfield lipid peak makes up to 10 % of the overall lipid signal in highly resolved ^{1}H spectra of cream (cf. Fig. 4.1).

have no or only a negligible effect on the reference Z-spectra in the spectral region of amide resonances, nor is it considered to affect the fat correction itself.

The novel CEST normalization is based on the fat-only image $\vec{F_0}$, which is then subtracted from all acquired images (cf. Eq. 4.12). $\vec{F_0}$ can be determined either by the utilization of a B_0 map or via a minimum approach. Both approaches yield comparable results and are considered equivalent. However, in order to obtain the B_0 map, an additional fit on conventional Z-spectra is required. As mentioned above, a fit could be unstable if phase artifacts of the DS or the pseudo rNOE artifacts are present, e.g. in the opposed-phase case or due to high B_0-inhomogeneities. The minimum approach is considered generally applicable and was therefore chosen for all evaluations.

Relaxation-compensation

CEST MRI of the human breast benefits from the high field strength of 7 T by an increased spectral resolution, despite the accompanying field inhomogeneities and associated challenges. Due to the high spectral resolution, CEST effects were successfully isolated via a five-pool Lorentzian fit. The AREX calculation requires a steady-state-like saturation, which was ensured by the increased saturation duration due to breathing synchronization ($t_{sat} = 5.6\,\mathrm{s} \approx 2.5 \cdot T_1$). Together, this enabled — for the first time — acquisition of a relaxation-compensated amide contrast of the human breast. Moreover, a contrast correction for B_1-inhomogeneities could be performed. This is of special importance, as inhomogeneities of B_1 are prevalent in breast imaging.

7.4 Examinations of mamma carcinoma patients

Recent patient studies indicated the potential of CEST MRI as a diagnostic tool for mamma carcinoma. Other studies have found a correlation of CEST contrast metrics to chemotherapy response [14, 64] and to tumor histology [15, 65]. One goal of this thesis was to define the examination and evaluation protocol for a clinical study of mamma carcinoma patients. Prospectively, a small cohort will be evaluated by the end of the year (n=12). For the first time, a correlation between histopathological features and the relaxation-compensated amide contrast can be investigated (e.g. proliferation index Ki-67 or estrogen receptor ER). The analysis of three patients was included in this work (cf. 6.4).

The first shown case presents the first amide contrast acquired in the human breast at 7 T to be corrected for spillover, T1 relaxation, B_1-inhomogeneities, and fat-signal contribution (Fig. 6.17). This examination also proved the applicability of the whole examination protocol as well as the novel fat correction. The multi-pool fit clearly identified amide and amine resonances and the fat-corrected $\mathrm{AREX_{amide}}$ contrast in the examined patient was significantly higher than in healthy women by a factor of 2.4.
The second patient shown gives an example of a mammary gland with extremely low fat content in both healthy and tumorous tissue (Fig. 6.18). This case demonstrates that the fat correction method does not overcompensate in cases with a low FF. The tumor was clearly distinguishable in the $\mathrm{AREX_{amide}}$ map by a distinct border and, again, an increased contrast. Surrounding healthy tissue showed contrast values in the order of the value obtained in young healthy women. The clear differentiation of tumorous from healthy tissue in the contrast maps points out the potential of CEST MRI as a non-invasive diagnostic tool. Interestingly, this case showed a prominent amine resonance in the tumor, which was not as present in healthy women or other patient examinations. Desmond *et al.* found that the amine resonance performed particularly

well in the distinction of tumor necrosis and/or apoptosis from healthy tissue in mice that were inoculated with a human breast cancer cell line [83]. Krikken *et al.* fit MT, water, and amide signals to CEST MRI of breast cancer patients, but neglected amine resonances [14]. Additional diagnostic utilizing of the amine resonance will hopefully be elucidated in future studies.

The third patient represents an exemplary examination of a mammary gland with varying FF (Fig. 6.19). In this patient, significant fat-signal artifacts presented as increased contrast, which could be mis-identified as a lesion or tumor. After the fat correction this contrast was reduced, but the overall $\mathrm{AREX}_{\mathrm{amide}}$ increased. The visible structures in the amide map are not clearly assignable to tumor or healthy tissue without the help of a radiologist and further clinical data. Also, the T2-weighted image provides no clear distinction. Here, the increased $\mathrm{AREX}_{\mathrm{amide}}$ might indicate tumor infiltration or progression. This patient examination demonstrates the importance of the fat-signal correction. A high size variety of the mammary gland as well as varying fat fractions within are expected for a larger patient and volunteer cohort.

The breast cancer patient examinations revealed an increased $\mathrm{AREX}_{\mathrm{amide}}$ contrast, despite morphological and tumor-pathological variance. In a recent brain tumor study, an increased amide contrast correlated to the overall survival of the patients [12]. Moreover, hyperintense relaxation-compensated amide contrasts spatially correlated to regions of decreased ADC values [12]. With respect to breast DWI, tumors appear in general hypointense in ADC maps, which is explained by the increased cellularity of tumorous tissue [5]. The relaxation-compensated amide contrast of the breast may potentially provide further clinical value, as it probes the biochemical tumor environment.

In order to develop CEST MRI as a diagnostic tool for the human breast, three dimensional imaging is required. This will allow the examination of the whole mammary gland rather than just a single slice. The best candidate is the recently published spiral-centric-reordered 3D GRE sequence (dubbed snapshot-CEST [84]). However, the acquisition time of this sequence is prolonged compared to the current 2D approach (approx. 3 s compared to 0.4 ms). This leads to a recovery of the magnetization during readout and subsequently, non-zero Z-values at $\Delta\omega = 0\,\mathrm{ppm}$ [84]. A direct application of the novel normalization is thereby prohibited. To overcome recovery during readout, a variable-flip-angle approach could be implemented [92, 93]. 3D imaging will also allow the registration of different measurements of a CEST examination. Furthermore, registration to other clinical MR data can be performed. Non-rigid registration procedures are challenging, especially in combination with varying image intensities. The algorithm presented by Wech & Köstler, who used a low-rank approximation of Z-spectra to correct the non-rigid motion of the thigh muscle [94], might applicable to the human breast.

7.5 Examinations of healthy volunteers

The human breast undergoes morphological and physiological changes during the menstrual cycle. Hormonal-induced variations of the water content of the breast parenchyma as well as the vascularity alter the perfusion properties and thereby affect dynamic contrast-enhanced (DCE) MRI [41, 43, 95, 96]. The *Guidelines from the European Society of Breast Imaging* therefore suggest a breast examination between the 5^{th} and 12^{th} day after the beginning of the cycle [4]. Diffusion-weighted breast MRI provides information about cell density, but is not found to be correlated with the menstrual cycle [5]. CEST MRI provides biochemical insights, but whether or not hormonal variations lead to a change of CEST signals was hitherto not investigated. Within this work, a potential correlation of hormonal changes with the isolated

amide contrast was explored. So far, no change of $\mathrm{AREX}_{\mathrm{amide}}$ between has been observed between the follicular and the luteal phase (i.e. shortly after the beginning of the cycle and after ovaluation). This observation allowed the determination of a reference value of amide contrast in healthy women ($AREX_{amide,\ healthy} = (3.74 \pm 0.46) \cdot 10^{-2}\mathrm{Hz}$). A comparison with CEST studies performed in the human breast is not appropriate, as this is the first application of relaxation-compensation. In another study of relaxation-compensated CEST in the human brain at 7 T, an average value for amide contrast in normal appearing white matter (nWM) is given by $AREX_{amide,\ nWM} = (5.0 \pm 0.4) \cdot 10^{-2}\mathrm{Hz}$ [3][17]. The obtained $\mathrm{AREX}_{\mathrm{amide}}$ value in the breast is in the same order of magnitude, but significantly lower than the reference value of nWM. The tissue density of healthy breast parenchyma is not as high as human brain tissue. Hence, the differences in amide contrast could be explained by a lower protein concentration. The observed T1 relaxation times are close to the reported value of $T_1 = (2265 \pm 65)\,\mathrm{ms}$ [32]. No hormonal-induced change of T1 could be determined. This is in line with a previously reported study in which an observed non-significant change of T1 was assigned to inter-subject variability [43]. Both aspects, menstrual cycle dependency of the amide contrast and T1 relaxation, are currently being investigated in a clinical pilot study. The data presented here shows, rather, a snapshot (n=4), and any statistical significance is as of yet inconclusive. However, the following can be assumed: hormonal-induced changes of the relaxation-compensated amide contrast of healthy breast tissue are minimal and with regard to tumor imaging, negligible.

[3] The value was read out from Fig. 5 f in Zaiss *et al.* [17].

8 | Summary

Breast cancer is the most common cancer in women, and its early detection is associated with better prognosis and mortality. The aim of this thesis was to provide a mammography modality by means of relaxation-compensated amide CEST MRI. To achieve this, novel CEST methods were successfully implemented and applied to examinations of healthy women and mamma carcinoma patients.

To enable relaxation-compensated amide CEST MRI of the breast, a fat correction method is required. For this purpose, a general theoretical description was derived explaining the interplay of the water and fat signal in the CEST experiment and thus, the origin of artifacts in Z-spectra. Phase information necessary for the fat correction was obtained by a newly implemented rawdata-based analysis. It was demonstrated that the collective fat signal of all lipid resonances can be retrieved by the Z-spectrum at the spectral position of the direct water saturation. This allowed the definition of a novel CEST normalization that corrects for fat-signal-induced artifacts in Z-spectra with a post-processing algorithm. This method presents a SAR and time-efficient approach compared to other CEST MRI, as this method does not require any further MR signal manipulation or additional measurements. The novel CEST normalization was verified *in vitro* and its applicability was shown *in vivo*.

To apply the before mentioned methods *in vivo*, further problems had to be solved. First, a profound interpretation of the amide signal *in vivo* requires the isolation from the background of multiple CEST signals. The isolation of CEST effects was achieved by adapting the established Lorentzian five-pool fitting routines and applied them to fat-signal-corrected and highly sampled Z-spectra. Second, the application of the inverse contrast metric yielded isolation and compensation for T2 water relaxation. Finally, a fat saturation was developed that outperformed the manufacturer-provided one, and enabled robust B_1 field and T1 mapping.

The developed methods were finally incorporated in a sophisticated imaging protocol for the examinations of patients. This enabled — for the first time — the examinations of mamma carcinoma patients using relaxation-compensated amide CEST MRI. Breathing induced non-rigid deformation of the breast could be largely avoided by a synchronization of the MR sequences to the breathing of the examined women. In this work, the findings of three patient examinations are presented. The observed $\mathrm{AREX}_{\mathrm{amide}}$ contrast was significantly increased in the tumor with respect to healthy glandular tissue. The reference value of $AREX_{amide,\ healthy} = (3.74 \pm 0.46) \cdot 10^{-2}\mathrm{Hz}$ was obtained as an average in four healthy volunteers. No change of the amide CEST contrast was distinguishable in the two different phases of the menstrual cycle.

With the methods established in this thesis, it is now possible to provide novel insights into the biochemical environment of breast cancer. Furthermore, the developed methods could also

potentially be applied to other fat containing entities, e.g. CEST imaging of the prostate or kidney. The forthcoming studies in larger patient cohorts will evaluate improvements of the specificity of the relaxation-compensated amide contrast and by this, the clinical impact of the developed methods.

9 | Appendix

Acquisition of proton spectra of fat-containing samples

In order to find suitable MR model solutions mimicking the *in vivo* fat composition, proton spectra of various fat-containing substances were acquired at 14.1 T: lard, cream, sunflower oil and egg yolk. They are displayed in Figure 4.1. Spectra were acquired on a $\nu_0 = 600.13$ MHz spectrometer (AVANCE II NMR spectrometer, 14.1 T, Bruker, Karlsruhe-Rheinstetten, Germany) using a 5 mm probe equipped with a z-axis gradient (Bruker, normal configuration QNP 13C, 31P, 19F/1H probe). A complete FID was recorded after a short 90° pulse.
The *in vivo* proton spectrum was acquired at 7 T in the breast of a healthy volunteer (V3) using a single-voxel semi-LASER sequence[97]. In comparison to the full LASER sequence [98], two pairs of adiabatic refocusing pulses following a conventional slice selection ensured the localization of the volume.

Start parameters of the multi pool fit

Table .1: Fit parameters 5-pool Lorentzian fit

	Offset	Water			amides			MT			amines			rNOE/fat		
	Z_{base}	A	Γ	δ	A	Γ	δ	A	Γ	δ	A	Γ	δ	A	Γ	δ
lower boundary	0.5	0.02	0.3	−1.0	0	1	3.0	0	4.0	−4.0	0	0.75	1.7	0	0.75	−4.0
start value	1	0.9	1.4	0	0	1.4	3.5	0.1	50	−2.0	0	1	2.2	0	1	−3.5
upper boundary	1.0	1	10	1	0.1	2.0	4.0	1	90	0	0.15	2.0	2.7	0.4	3	−2.8

Table .2: Fit parameters Lorentzian and Carnosine

	amides			polynomial		
	A	Γ	δ	a	b	c
lower boundary	0	0.25	3.0	−10	−10	0.8
start value	0.01	0.3	3.2	0	0	0.98
upper boundary	0.3	0.4	3.4	10	10	1.2

Acquisition parameters cream phantom

Table .3: Acquisition parameters of the 2D GRE sequence used for field-mapping and T1 mapping in cream. Coil: 1Tx/24Rx head coil. The WASABI and the T1 was repeated with varying TE twice, once with and once without the developed fat saturation prior to imaging.

matrix size	128 x 128 pixel
field of view	128 x 128 mm^2
slice thickness	5 mm
slice orientation	transversal
repetition time (TR)[ms]	4.7 ms
echo time (TE)[ms]	1.91:0.1:2.81 ms
WASABI - settings	
$t_{recover}$	3 s
$t_{recover,\ M_0}$	15 s
sampling	201 offsets equally spaced between $\Delta\omega = \pm 6$ ppm
T1 - settings	
recovery times $t_{recover}$	16, 14, 12, 10, 9, 8, 7, 6.5, 6, 5.5, 5, 4.5, 4, 3.8, 3.7, 3.6, 3.5, 3.4, 3.3, 3.2, 3.1, 3, 2.9, 2.8, 2.7, 2.6, 2.4, 2.3, 2.2, 2.1, 2.0, 1.9, 1.8, 1.6, 1.4, 1.2, 1.0, 0.8, 0.6, 0.4, 0.25, and 0.1 s

Acquisition parameters carnosine phantom experiment

Table .4: Acquisition parameters of the 2D GRE sequence used for the carnosine-oil phantom. Coil: 1Tx/16Rx breast coil array. The CEST experiment was repeated for various echo times.

CEST - settings	
number of pulses	95
pulse duration	100 ms
DS	95 %
Saturation amplitude B_1	0.6 µT & 0.8 µT
sampling of $\Delta\omega$	300, 150, 75, 25, 8, 5.5, 5.0, 4.8, 4.6, 4.4, 4.25, 4.1, 4.0, 3.9, 3.8, 3.7, 3.6, 3.5, 3.4, 3.3, 3.2, 3.1, 3, 2.9, 2.75, 2.6, 2.45, 2.3, 2.15, 2, 1.85, 1.7, 1.55, 1.4, 1.25, 1.1, 0.95, 0.80, 0.70, 0.60, 0.50, 0.40, 0.30, 0.20, 0.10, 0, −0.10, −0.20, −0.30, −0.40, −0.50, −0.60, −0.70, −0.80, −0.95, −1.1, −1.4, −1.7, −1.95, −2.2, −2.4, −2.6, −2.8, −3.0, −3.2, −3.35, −3.5, −3.65, −3.8, −4.0, −4.3, −4.6, −5, −5.5, −15, −75, −150, and −300 ppm
Imaging parameters	
matrix size	128 x 128 pixel
field of view	141 x 141 mm^2
slice thickness	3 mm
slice orientation	coronal
repetition time (TR)[ms]	4.4 ms
echo time (TE)[ms]	1.9, 2.04 (in phase), 2.17, 2.43, 2.55 (opposed phase), 2.65

Acquisition parameters of in vivo examinations

The standard examination protocol is provided in Chapter 5. If the examination protocol was changed, it is provided here.

- Fig. 6.1:
  - Volunteer: V1;
  - FoV: 128x128
  - Subfigures (A): TE: 3.7 ms; TR: 2.05 ms; (B): TE = 1.63 ms; TR = 17 ms; (C): TE = 3.07; TR = 3.3 ms
- Figures 6.4, 6.7, 6.10, 6.11, 6.13:
  - Volunteer V1;
  - $TE_{\text{in-phase}} = 2.04\,\text{ms}$; $TE_{\text{opp-phase}} = 2.55\,\text{ms}$; TR = 4.2 ms
- Fig. 6.14 A & Fig. 6.15:
  - Volunteer V1;
  - $t_p = 15\,\text{ms}$ &100 ms
- Fig. 6.14 B:
  - Volunteer V2;
  - $t_p = 15\,\text{ms}, 25\,\text{ms}$ & 100 ms;
  - $\Delta\omega = [-1.2 : 0.04 : 1.2]$ ppm;
  - B_1= 0.6 µT
- Fig. 6.19:
  - Patient P3;
  - The CEST-measurement at B_1= 0.6 µT had to be repeated with a shorter offset list (60 instead of 75, $\Delta\omega$ = 295, 300, 290, 100, 50, 20, 12, 8, 6.25, 5.25, 4.7, 4.4, 4.25, 4.1, 3.95, 3.8, 3.7, 3.6, 3.5, 3.4, 3.3, 3.2, 3.1, 3, 2.9, 2.75, 2.6, 2.45, 2.3, 2.15, 2, 1.85, 1.7, 1.55, 1.4, 1.25, 1.1, 0.95, 0.80, 0.70, 0.60, 0.50, 0.40, 0.30, 0.225, 0.15, 0.075, 0, −0.075, −0.15, −0.225, −0.30, −0.40, −0.50, −0.60, −0.70, −0.80, −0.95, $-1.1, and$ −1.4 ppm).
  - The multi-pool fit was adapted by discarding the fifth pool for rNOE/fat. Amide resonances were robustly identified.

Bibliography

1. Institut, R. K. *Krebs in Deutschland für 2013/2014 [Cancer in Germany in 2013/2014]* 2017.
2. Oeffinger, K. C. *et al.* Breast cancer screening for women at average risk: 2015 guideline update from the American Cancer Society. *Jama* **314,** 1599–1614 (2015).
3. Saslow, D. *et al.* American Cancer Society guidelines for breast screening with MRI as an adjunct to mammography. *CA: a cancer journal for clinicians* **57,** 75–89 (2007).
4. Mann, R. M., Kuhl, C. K., Kinkel, K. & Boetes, C. Breast MRI: guidelines from the European society of breast imaging. *European radiology* **18,** 1307–1318 (2008).
5. Partridge, S. C., Nissan, N., Rahbar, H., Kitsch, A. E. & Sigmund, E. E. Diffusion-weighted breast MRI: Clinical applications and emerging techniques. *Journal of magnetic resonance imaging* **45,** 337–355 (2017).
6. Bickelhaupt, S., Jaeger, P. F., *et al.* Radiomics Based on Adapted Diffusion Kurtosis Imaging Helps to Clarify Most Mammographic Findings Suspicious for Cancer. *Radiology* **287,** 761–770 (2018).
7. Bickelhaupt, S., Tesdorff, J., *et al.* Independent value of image fusion in unenhanced breast MRI using diffusion-weighted and morphological T2-weighted images for lesion characterization in patients with recently detected BI-RADS 4/5 x-ray mammography findings. *European radiology* **27,** 562–569 (2017).
8. McMahon, M. T., Gilad, A. A., Bulte, J. W. & Van Zijl, P. C. *Chemical exchange saturation transfer imaging: advances and applications* (CRC Press, 2017).
9. Goerke, S., Zaiss, M., Kunz, P., Klika, K. D., Windschuh, J. D., Mogk, A., Bukau, B., Ladd, M. E. & Bachert, P. Signature of protein unfolding in chemical exchange saturation transfer imaging. *NMR in Biomedicine* **28,** 906–913 (2015).
10. Goerke, S., Milde, K. S., *et al.* Aggregation-induced changes in the chemical exchange saturation transfer (CEST) signals of proteins. *NMR in Biomedicine* **30,** e3665 (2017).
11. Paech, D., Windschuh, J., *et al.* Assessing the predictability of IDH mutation and MGMT methylation status in glioma patients using relaxation-compensated multipool CEST MRI at 7.0 T. *Neuro-oncology* **20,** 1661–1671 (2018).
12. Paech, D., Dreher, C., *et al.* Relaxation-compensated amide proton transfer (APT) MRI signal intensity is associated with survival and progression in high-grade glioma patients. *European radiology,* 1–11 (2019).
13. Schmitt, B., Zamecnik, P., Zaiss, M., Rerich, E., Schuster, L., Bachert, P. & Schlemmer, H.-P. *A new contrast in MR mammography by means of chemical exchange saturation transfer (CEST) imaging at 3 Tesla: preliminary results* in *RöFo-Fortschritte auf dem Gebiet der Röntgenstrahlen und der bildgebenden Verfahren* **183** (2011), 1030–1036.

14. Krikken, E., Khlebnikov, V., Zaiss, M., Jibodh, R. A., van Diest, P. J., Luijten, P. R., Klomp, D. W., Van Laarhoven, H. W. & Wijnen, J. P. Amide chemical exchange saturation transfer at 7 T: a possible biomarker for detecting early response to neoadjuvant chemotherapy in breast cancer patients. *Breast Cancer Research* **20,** 51 (2018).

15. Zhang, S., Seiler, S., Wang, X., Madhuranthakam, A. J., Keupp, J., Knippa, E. E., Lenkinski, R. E. & Vinogradov, E. CEST-Dixon for human breast lesion characterization at 3 T: A preliminary study. *Magnetic resonance in medicine* **80,** 895–903 (2018).

16. Zaiss, M., Xu, J., Goerke, S., Khan, I. S., Singer, R. J., Gore, J. C., Gochberg, D. F. & Bachert, P. Inverse Z-spectrum analysis for spillover-, MT-, and T1-corrected steady-state pulsed CEST-MRI–application to pH-weighted MRI of acute stroke. *NMR in biomedicine* **27,** 240–252 (2014).

17. Zaiss, M., Windschuh, J., *et al.* Relaxation-compensated CEST-MRI of the human brain at 7 T: unbiased insight into NOE and amide signal changes in human glioblastoma. *Neuroimage* **112,** 180–188 (2015).

18. Windschuh, J., Zaiss, M., Meissner, J.-E., Paech, D., Radbruch, A., Ladd, M. E. & Bachert, P. Correction of B1-inhomogeneities for relaxation-compensated CEST imaging at 7 T. *NMR in biomedicine* **28,** 529–537 (2015).

19. Van Rijssel, M. J., Pluim, J. P., Luijten, P. R., Gilhuijs, K. G., Raaijmakers, A. J. & Klomp, D. W. Estimating B1+ in the breast at 7 T using a generic template. *NMR in Biomedicine* **31,** e3911 (2018).

20. Lu, J., Zhou, J., Cai, C., Cai, S. & Chen, Z. Observation of true and pseudo NOE signals using CEST-MRI and CEST-MRS sequences with and without lipid suppression. *Magnetic resonance in medicine* **73,** 1615–1622 (2015).

21. Haacke, E. M., Brown, R. W., Thompson, M. R., Venkatesan, R., *et al. Magnetic resonance imaging: physical principles and sequence design* (Wiley-Liss New York: 1999).

22. De Graaf, R. A. *In vivo NMR Spectroscopy: Principles and Techniques: 2nd Edition.* (John Wiley & Sons, 2007).

23. Bernstein, M. A., King, K. F. & Zhou, X. J. *Handbook of MRI pulse sequences* (Elsevier, 2004).

24. Zeeman, P. On the Influence of Magnetism on the Nature of the Light Emitted by a Substance. *Astrophysical Journal* **5,** 332. doi:10.1086/140355 (1897).

25. Ehrenfest, P. Bemerkung über die angenäherte Gültigkeit der klassischen Mechanik innerhalb der Quantenmechanik. *Zeitschrift für Physik A Hadrons and Nuclei* **45,** 455–457 (1927).

26. Bohr, N. Über die serienspektra der elemente. *Zeitschrift für Physik A Hadrons and Nuclei* **2,** 423–469 (1920).

27. Bloch, F. Nuclear induction. *Physical review* **70,** 460 (1946).

28. Windschuh, J. *Isolation of Unbiased Chemical Exchange Saturation Transfer Effects at 7 T and Application to Brain Tumors* PhD Thesis (Ruprecht-Karls University Heidelberg, 2016).

29. Book, G. Compendium of chemical terminology. *International Union of Pure and Applied Chemistry* **528** (2014).

30. Szczepaniak, L. S., Babcock, E. E., Schick, F., Dobbins, R. L., Garg, A., Burns, D. K., McGarry, J. D. & Stein, D. T. Measurement of intracellular triglyceride stores by H spectroscopy: validation in vivo. *American Journal of Physiology-Endocrinology And Metabolism* **276,** E977–E989 (1999).

31. Dimitrov, I. E., Douglas, D., Ren, J., Smith, N. B., Webb, A. G., Sherry, A. D. & Malloy, C. R. In vivo determination of human breast fat composition by 1H magnetic resonance spectroscopy at 7 T. *Magnetic resonance in medicine* **67,** 20–26 (2012).

32. Haddadin, I. S. *et al.* Metabolite quantification and high-field MRS in breast cancer. *NMR in Biomedicine: An International Journal Devoted to the Development and Application of Magnetic Resonance In vivo* **22,** 65–76 (2009).

33. Hauger, O., Dumont, E., Chateil, J.-F., Moinard, M. & Diard, F. Water excitation as an alternative to fat saturation in MR imaging: preliminary results in musculoskeletal imaging. *Radiology* **224,** 657–663 (2002).

34. Bydder, G. M., Pennock, J., Steiner, R., Khenia, S., Payne, J. & Young, I. R. The short TI inversion recovery sequence—an approach to MR imaging of the abdomen. *Magnetic resonance imaging* **3,** 251–254 (1985).

35. Dixon, W. T. Simple proton spectroscopic imaging. *Radiology* **153,** 189–194 (1984).

36. Wang, Y., Li, D., Haacke, E. M. & Brown, J. J. A three-point Dixon method for water and fat separation using 2D and 3D gradient-echo techniques. *Journal of Magnetic Resonance Imaging* **8,** 703–710 (1998).

37. Reeder, S. B., Pineda, A. R., Wen, Z., Shimakawa, A., Yu, H., Brittain, J. H., Gold, G. E., Beaulieu, C. H. & Pelc, N. J. Iterative decomposition of water and fat with echo asymmetry and least-squares estimation (IDEAL): application with fast spin-echo imaging. *Magnetic Resonance in Medicine: An Official Journal of the International Society for Magnetic Resonance in Medicine* **54,** 636–644 (2005).

38. Krombach, G. A. & Mahnken, A. H. *Radiologische Diagnostik Abdomen und Thorax: Bildinterpretation unter Berücksichtigung anatom. Landmarken u. klin. Symptome* (Georg Thieme Verlag, 2015).

39. Schmidt, R. F., Lang, F. & Heckmann, M. *Physiologie des Menschen: mit Pathophysiologie* (Springer-Verlag, 2011).

40. Gätje, R., Eberle, C., Scholz, C., Lübke, M. & Solbach, C. *Kurzlehrbuch Gynäkologie und Geburtshilfe* (Georg Thieme Verlag, 2015).

41. Weinstein, S. P., Conant, E. F., Sehgal, C. M., Woo, I. P. & Patton, J. A. Hormonal variations in the vascularity of breast tissue. *Journal of ultrasound in medicine* **24,** 67–72 (2005).

42. Vogel, P. M., Georgiade, N., Fetter, B., Vogel, F. & McCarty Jr, K. The correlation of histologic changes in the human breast with the menstrual cycle. *The American journal of pathology* **104,** 23 (1981).

43. Delille, J.-P., Slanetz, P. J., Yeh, E. D., Kopans, D. B. & Garrido, L. Physiologic changes in breast magnetic resonance imaging during the menstrual cycle: perfusion imaging, signal enhancement, and influence of the T1 relaxation time of breast tissue. *The breast journal* **11,** 236–241 (2005).

44. Zaiss, M. & Bachert, P. Chemical exchange saturation transfer (CEST) and MR Z-spectroscopy in vivo: a review of theoretical approaches and methods. *Physics in Medicine & Biology* **58,** R221 (2013).

45. Liu, G., Song, X., Chan, K. W. & McMahon, M. T. Nuts and bolts of chemical exchange saturation transfer MRI. *NMR in Biomedicine* **26,** 810–828 (2013).

46. Meissner, J.-E. *Quantitative pulsed CEST MR imaging* PhD Thesis (Ruprecht-Karls University Heidelberg, 2017).

47. Liepinsh, E. & Otting, G. Proton exchange rates from amino acid side chains—implications for image contrast. *Magnetic resonance in medicine* **35,** 30–42 (1996).

48. Solomon, I. Relaxation processes in a system of two spins. *Physical Review* **99,** 559 (1955).

49. McConnell, H. M. Reaction rates by nuclear magnetic resonance. *The Journal of Chemical Physics* **28,** 430–431 (1958).

50. Friedman, J. I., Xia, D., Regatte, R. R. & Jerschow, A. Transfer Rate Edited experiment for the selective detection of Chemical Exchange via Saturation Transfer (TRE-CEST). *Journal of Magnetic Resonance* **256,** 43–51 (2015).

51. Zhou, J. & Van Zijl, P. C. Chemical exchange saturation transfer imaging and spectroscopy. *Progress in Nuclear Magnetic Resonance Spectroscopy* **48,** 109–136 (2006).

52. Zhou, J., Payen, J.-F., Wilson, D. A., Traystman, R. J. & Van Zijl, P. C. Using the amide proton signals of intracellular proteins and peptides to detect pH effects in MRI. *Nature medicine* **9,** 1085 (2003).

53. Goerke, S., Zaiss, M. & Bachert, P. Characterization of creatine guanidinium proton exchange by water-exchange (WEX) spectroscopy for absolute-pH CEST imaging in vitro. *NMR in Biomedicine* **27,** 507–518 (2014).

54. McNaught, A. D. & McNaught, A. D. *Compendium of chemical terminology* (Blackwell Science Oxford, 1997).

55. Van Zijl, P. C. & Yadav, N. N. Chemical exchange saturation transfer (CEST): what is in a name and what isn't? *Magnetic resonance in medicine* **65,** 927–948 (2011).

56. Liu, D., Zhou, J., Xue, R., Zuo, Z., An, J. & Wang, D. J. Quantitative characterization of nuclear overhauser enhancement and amide proton transfer effects in the human brain at 7 tesla. *Magnetic resonance in medicine* **70,** 1070–1081 (2013).

57. Xu, J., Yadav, N. N., Bar-Shir, A., Jones, C. K., Chan, K. W., Zhang, J., Walczak, P., McMahon, M. T. & Van Zijl, P. C. Variable delay multi-pulse train for fast chemical exchange saturation transfer and relayed-nuclear overhauser enhancement MRI. *Magnetic resonance in medicine* **71,** 1798–1812 (2014).

58. Görke, S. *Einfluss von Entfaltung und Aggregation auf den 1H-Magnetisierungstransfer zwischen Proteinen und freiem Wasser* PhD thesis (2015).

59. Jin, T. & Kim, S.-G. *In vivo saturation transfer imaging of nuclear Overhauser effect from aromatic and aliphatic protons: implication to APT quantification* in *Proceedings of the 21st Annual Meeting ISMRM* (2013).

60. Zaiss, M. & Bachert, P. Exchange-dependent relaxation in the rotating frame for slow and intermediate exchange–modeling off-resonant spin-lock and chemical exchange saturation transfer. *NMR in Biomedicine* **26,** 507–518 (2013).

61. Trott, O. & Palmer III, A. G. *R1ρ relaxation outside of the fast-exchange limit* 2002.

62. Meissner, J.-E., Goerke, S., Rerich, E., Klika, K. D., Radbruch, A., Ladd, M. E., Bachert, P. & Zaiss, M. Quantitative pulsed CEST-MRI using Ω-plots. *NMR in Biomedicine* **28,** 1196–1208 (2015).

63. Zhang, S., Keupp, J., Wang, X., Dimitrov, I., Madhuranthakam, A. J., Lenkinski, R. E. & Vinogradov, E. Z-spectrum appearance and interpretation in the presence of fat: Influence of acquisition parameters. *Magnetic resonance in medicine* **79,** 2731–2737 (2018).

64. Dula, A. N., Arlinghaus, L. R., Dortch, R. D., Dewey, B. E., Whisenant, J. G., Ayers, G. D., Yankeelov, T. E. & Smith, S. A. Amide proton transfer imaging of the breast at 3 T: establishing reproducibility and possible feasibility assessing chemotherapy response. *Magnetic resonance in medicine* **70,** 216–224 (2013).

65. Zaric, O., Farr, A., Rodriguez, E. P., Mlynarik, V., Bogner, W., Gruber, S., Asseryanis, E., Singer, C. F. & Trattnig, S. 7T CEST MRI: A potential imaging tool for the assessment of tumor grade and cell proliferation in breast cancer. *Magnetic resonance imaging* (2019).

66. Desmond, K. L., Moosvi, F. & Stanisz, G. J. Mapping of amide, amine, and aliphatic peaks in the CEST spectra of murine xenografts at 7 T. *Magnetic resonance in medicine* **71,** 1841–1853 (2014).

67. Klomp, D. W. *et al.* Amide proton transfer imaging of the human breast at 7T: development and reproducibility. *NMR in biomedicine* **26,** 1271–1277 (2013).

68. Dula, A. N., Dewey, B. E., Arlinghaus, L. R., Williams, J. M., Klomp, D., Yankeelov, T. E. & Smith, S. Optimization of 7-T chemical exchange saturation transfer parameters for validation of glycosaminoglycan and amide proton transfer of fibroglandular breast tissue. *Radiology* **275,** 255–261 (2014).

69. Reeder, S. B., Wen, Z., Yu, H., Pineda, A. R., Gold, G. E., Markl, M. & Pelc, N. J. Multicoil Dixon chemical species separation with an iterative least-squares estimation method. *Magnetic Resonance in Medicine: An Official Journal of the International Society for Magnetic Resonance in Medicine* **51,** 35–45 (2004).

70. Yu, H., Shimakawa, A., McKenzie, C. A., Brodsky, E., Brittain, J. H. & Reeder, S. B. Multiecho water-fat separation and simultaneous R estimation with multifrequency fat spectrum modeling. *Magnetic Resonance in Medicine: An Official Journal of the International Society for Magnetic Resonance in Medicine* **60,** 1122–1134 (2008).

71. (DKFZ), G. C. R. C. `https://www.dkfz.de/en/medphysrad/workinggroups/ultrahighfieldmr/ultrahighfieldmr.html`.

72. Schmitt, B., Zaiß, M., Zhou, J. & Bachert, P. Optimization of pulse train presaturation for CEST imaging in clinical scanners. *Magnetic resonance in medicine* **65,** 1620–1629 (2011).

73. Walsh, D. O., Gmitro, A. F. & Marcellin, M. W. Adaptive reconstruction of phased array MR imagery. *Magnetic Resonance in Medicine: An Official Journal of the International Society for Magnetic Resonance in Medicine* **43,** 682–690 (2000).

74. Griswold, M., Walsh, D., Heidemann, R. M., Haase, A. & Jakob, P. The Use of an Adaptive Reconstruction for Array Coil Sensitivity Mapping and Intensity Normalization. *Proceedings of the 10th Meeting of the International Society for Magnetic Resonance in Medicine* **43,** 2410 (2002).

75. Inati Souheil J, Hansen, M. S. & Kellman, P. A solution to the phase problem in adaptive coil combination. *Proceedings of the 21th Annual Meeting of ISMRM, Salt Lake City, USA* **16,** 2672 (2013).

76. Schuenke, P., Windschuh, J., Roeloffs, V., Ladd, M. E., Bachert, P. & Zaiss, M. Simultaneous mapping of water shift and B1 (WASABI)—Application to field-Inhomogeneity correction of CEST MRI data. *Magnetic resonance in medicine* **77,** 571–580 (2017).

77. Bernstein, M. A., King, K. F. & Zhou, X. J. *Handbook of MRI pulse sequences* (Elsevier, 2004).

78. Lourakis, M. I. *et al.* A brief description of the Levenberg-Marquardt algorithm implemented by levmar. *Foundation of Research and Technology* **4,** 1–6 (2005).

79. Kim, M., Gillen, J., Landman, B. A., Zhou, J. & Van Zijl, P. C. Water saturation shift referencing (WASSR) for chemical exchange saturation transfer (CEST) experiments. *Magnetic Resonance in Medicine: An Official Journal of the International Society for Magnetic Resonance in Medicine* **61,** 1441–1450 (2009).

80. Bodet, O., Goerke, S., Behl, N. G., Roeloffs, V., Zaiss, M. & Bachert, P. Amide proton transfer of carnosine in aqueous solution studied in vitro by WEX and CEST experiments. *NMR in Biomedicine* **28,** 1097–1103 (2015).

81. Klein, J., Lam, W. W., Czarnota, G. J. & Stanisz, G. J. Chemical exchange saturation transfer MRI to assess cell death in breast cancer xenografts at 7T. *Oncotarget* **9,** 31490 (2018).

82. Chan, K. W., Jiang, L., Cheng, M., Wijnen, J. P., Liu, G., Huang, P., van Zijl, P. C., McMahon, M. T. & Glunde, K. CEST-MRI detects metabolite levels altered by breast cancer cell aggressiveness and chemotherapy response. *NMR in biomedicine* **29,** 806–816 (2016).

83. Desmond, K. L., Moosvi, F. & Stanisz, G. J. Mapping of amide, amine, and aliphatic peaks in the CEST spectra of murine xenografts at 7 T. *Magnetic resonance in medicine* **71,** 1841–1853 (2014).

84. Zaiss, M., Ehses, P. & Scheffler, K. Snapshot-CEST: Optimizing spiral-centric-reordered gradient echo acquisition for fast and robust 3D CEST MRI at 9.4 T. *NMR in Biomedicine* **31,** e3879 (2018).

85. Goerke, S., Soehngen, Y., *et al.* Relaxation-compensated APT and rNOE CEST-MRI of human brain tumors at 3 T. *Magnetic Resonance in Medicine* (2019).

86. Boer, V. O., vd Bank, B. L., van Vliet, G., Luijten, P. R. & Klomp, D. W. Direct B0 field monitoring and real-time B0 field updating in the human breast at 7 Tesla. *Magnetic resonance in medicine* **67,** 586–591 (2012).

87. Platt, T. *et al.* In vivo self-gated 23Na MRI at 7 T using an oval-shaped body resonator. *Magnetic resonance in medicine* **80,** 1005–1019 (2018).

88. Meissner, J.-E., Korzowski, A., *et al.* Early response assessment of glioma patients to definitive chemoradiotherapy using chemical exchange saturation transfer imaging at 7 T. *Journal of Magnetic Resonance Imaging* (2019).

89. Zaiss, M., Herz, K., Deshmane, A., Kim, M., Golay, X., Lindig, T., Bender, B., Ernemann, U. & Scheffler, K. Possible artifacts in dynamic CEST MRI due to motion and field alterations. *Journal of Magnetic Resonance* **298,** 16–22 (2019).

90. Nehrke, K., Versluis, M. J., Webb, A. & Börnert, P. Volumetric B1+ mapping of the brain at 7T using DREAM. *Magnetic resonance in medicine* **71,** 246–256 (2014).

91. Deshmane, A., Zaiss, M., Lindig, T., Herz, K., Schuppert, M., Gandhi, C., Bender, B., Ernemann, U. & Scheffler, K. 3D gradient echo snapshot CEST MRI with low power saturation for human studies at 3T. *Magnetic resonance in medicine* **81,** 2412–2423 (2019).

92. Kunth, M., Döpfert, J., Witte, C., Rossella, F. & Schröder, L. Optimized use of reversible binding for fast and selective NMR localization of caged xenon. *Angewandte Chemie International Edition* **51,** 8217–8220 (2012).

93. Mugler III, J. P., Epstein, F. H. & Brookeman, J. R. Shaping the signal response during the approach to steady state in three-dimensional magnetization-prepared rapid gradient-echo imaging using variable flip angles. *Magnetic resonance in medicine* **28,** 165–185 (1992).

94. Wech, T. & Köstler, H. Robust motion correction in CEST imaging exploiting low-rank approximation of the z-spectrum. *Magnetic resonance in medicine* **80,** 1979–1988 (2018).

95. Kuhl, C. K., Bieling, H. B., Gieseke, J., Kreft, B. P., Sommer, T., Lutterbey, G. & Schild, H. H. Healthy premenopausal breast parenchyma in dynamic contrast-enhanced MR imaging of the breast: normal contrast medium enhancement and cyclical-phase dependency. *Radiology* **203,** 137–144 (1997).

96. Fowler, P., Casey, C., Cameron, G., Foster, M. & Knight, C. Cyclic changes in composition and volume of the breast during the menstrual cycle, measured by magnetic resonance imaging. *BJOG: An International Journal of Obstetrics & Gynaecology* **97,** 595–602 (1990).

97. Scheenen, T. W., Klomp, D. W., Wijnen, J. P. & Heerschap, A. Short echo time 1H-MRSI of the human brain at 3T with minimal chemical shift displacement errors using adiabatic refocusing pulses. *Magnetic Resonance in Medicine: An Official Journal of the International Society for Magnetic Resonance in Medicine* **59,** 1–6 (2008).

98. Garwood, M. & DelaBarre, L. The return of the frequency sweep: designing adiabatic pulses for contemporary NMR. *Journal of magnetic resonance* **153,** 155–177 (2001).

99. Jia, G., Wei, W., Yang, X., Flanigan, D. C., Keupp, J., Zhou, J. & Knopp, M. V. *Improving mobile protein level detection using mDIXON-based APT-MRI in bone marrow edema* in *Proc 20th Annual Meeting ISMRM; Melbourane, Australia* (2012), 3373.

100. Windschuh, J., Zaiss, M., Ehses, P., Lee, J.-S., Jerschow, A. & Regatte, R. R. Assessment of frequency drift on CEST MRI and dynamic correction: application to gagCEST at 7 T. *Magnetic resonance in medicine* **81,** 573–582. doi:10.1002/mrm.27367 (2018).

101. Zimmermann, F., Korzowski, A., Schuenke, P., Breitling, J., Zaiss, M., Paech, D., Ladd, M. E. & Goerke, S. *Fat corrected APT-CEST in the human breast* in *Proceedings of the 7th International Workshop on Chemical Exchange Saturation Transfer Imaging 2018* (2018).

102. Lide, D. R. *CRC handbook of chemistry and physics* (CRC press, 2004).

103. Sun, P. Z., Van Zijl, P. C. & Zhou, J. Optimization of the irradiation power in chemical exchange dependent saturation transfer experiments. *Journal of magnetic resonance* **175,** 193–200 (2005).

104. Le, Y., Kroeker, R., Kipfer, H. D. & Lin, C. Development and evaluation of TWIST Dixon for dynamic contrast-enhanced (DCE) MRI with improved acquisition efficiency and fat suppression. *Journal of Magnetic Resonance Imaging* **36,** 483–491 (2012).

List of Figures

List of Tables

List of scientific contributions

Parts of this work appeared in the following conference contributions:

- Talk:
  Zimmermann, Ferdinand; Korzowski, Andreas; Schuenke, Patrick; Breitling, Johannes; Zaiss, Moritz; Paech, Daniel; Ladd, Mark Edward; Goerke, Steffen. *Fat corrected APT-CEST in the human breast.* At: 7$^{\text{th}}$ International Workshop on Chemical Exchange Saturation Transfer Imaging, Beijing, China (2018).

- Poster:
  Meissner, Jan-Eric; Breitling, Johannes; **Zimmermann, Ferdinand**; Goerke, Steffen; Korzowski, Andreas; Zaiss, Moritz; Ladd, Mark E.; Bachert Peter. *FullHD CEST imaging in the human brain at 7T.* At: 7$^{\text{th}}$ International Workshop on Chemical Exchange Saturation Transfer Imaging, Beijing, China (2018).

- Traditional poster:
  Zimmermann, Ferdinand; Korzowski, Andreas; Schuenke, Patrick; Breitling, Johannes; Ladd, Mark Edward; Bachert, Peter; Goerke, Steffen. *A novel normalization to correct APT-CEST in the presence of fat.* At: 26$^{\text{th}}$ Annual Meeting of the International Society for Magnetic Resonance in Medicine, Paris, France (2018).

- Electronical Poster:
  Zimmermann, Ferdinand; Goerke, Steffen; Breitling, Johannes; Klopries, Kerstin; Windschuh, Johannes; Schlemmer, Heinz-Peter; Ladd, Mark Edward; Paech, Daniel; Bachert, Peter. *Correction of fat artifacts for unbiased CEST-MRI of the human breast at 7T.* At: 25$^{\text{th}}$ Annual Meeting of the International Society for Magnetic Resonance in Medicine, Honolulu, USA (2017).

Three abstracts were accepted for the upcoming 27$^{\text{th}}$ Annual Meeting of the International Society for Magnetic Resonance in Medicine, Montreal, Canada (2019):

- Power-Pitch and Poster:
  Zimmermann, Ferdinand; Korzowski, Andreas; Loi, Lisa C.; Breitling, Johannes S.; Meissner, Jan-Eric; Zaiss, Moritz; Bickelhaupt, Sebastian; Schlemmer, Heinz-Peter; Ladd, Mark E.; Bachert, Peter; Paech, Daniel; Schott, Sarah; Goerke, Steffen. *Fat corrected APT-CEST in the human breast at 7 Tesla: application to mamma carcinoma and dependency on menstrual cycle.*

- Poster:
  Franke, Vanessa; **Zimmermann, Ferdinand**; Magill, Arthur W.; Ladd, Mark E.; Bachert, Peter; Korzowski, Andreas. *Functional 31P Magnetic Resonance Spectroscopy of the Human Visual Cortex using Repeated Short-Term Stimulation at 7T.*

- Poster:
  Boyd, Philip S; Breitling, Johannes; **Zimmermann, Ferdinand**; Korzowski, Andreas; Zaiss, Moritz; Schuenke, Patrick; Weinfurter, Nina; Schlemmer, Heinz-Peter; Ladd, Mark E.; Bachert, Peter; Paech, Daniel; Goerke, Steffen. *Acquisition protocol for glucoCESL MRI in the human brain at 7T with reduced motion-induced artifacts.*

Complete list of scientific contributions

Journal contributions

Goerke, Steffen; Soehngen, Yannick; Deshmane, Anagha; Zaiss, Moritz; Breitling, Johannes; Boyd, Philip S.; Herz, Kai; **Zimmermann, Ferdinand**; Klika, Karel D; Schlemmer, Heinz-Peter; Paech, Daniel; Ladd, Mark E.; Bachert, Peter. *Relaxation-compensated APT and rNOE CEST-MRI of human brain tumors at 3T.* Magnetic Resonance in Medicine (2019), 1–11; doi: 10.1002/mrm.27751.

Dokic, Ivana; Mairani, Andrea; Niklas, Martin; **Zimmermann, Ferdinand**; Chaudhri, Naved; Krunic, Damir; Tessonnier, Thomas; Ferrari, Alfredo; Parodi, Katia; Jäkel, Oliver; Debus, Jürgen; Haberer, Thomas; Abdollahi, Amir. *Next generation multi-scale biophysical characterization of high precision cancer particle radiotherapy using clinical proton, helium-, carbon-and oxygen ion beams.* Oncotarget (2016), 7(35), 56676; doi: 10.18632/oncotarget.10996.

Niklas, Martin; **Zimmermann, Ferdinand**; Schlegel, Julian; Schwager, Christian; Debus, Jürgen; Jäkel, Oliver; Abdollahi, Amir; Greilich, Steffen. *Registration procedure for spatial correlation of physical energy deposition of particle irradiation and cellular response utilizing cell-fluorescent ion track hybrid detectors.* Physics in Medicine & Biology (2016), 61(17), N441-N460; doi: 10.1088/0031-9155/61/17/N441.

Dokic, Ivana; Niklas, Martin; **Zimmermann, Ferdinand**; Mairani, Andrea; Seidel, Philipp; Krunic, Damir; Jäkel, Oliver; Debus, Jürgen; Greilich, Steffen; Abdollahi, Amir. *Correlation of Particle Traversals with Clonogenic Survival Using Cell-Fluorescent Ion Track Hybrid Detector.* Radiotherapy and Oncology (2015), 118, S33-S34; doi: 10.3389/fonc.2015.00275.

Conference contributions

Zimmermann, Ferdinand; Korzowski, Andreas; Loi, Lisa C.; Breitling, Johannes S.; Meissner, Jan-Eric; Zaiss, Moritz; Bickelhaupt, Sebastian; Schlemmer, Heinz-Peter; Ladd, Mark E.; Bachert, Peter; Paech, Daniel; Schott, Sarah; Goerke, Steffen. *Fat corrected APT-CEST in the human breast at 7 Tesla: application to mamma carcinoma and dependency on menstrual cycle.* In: Proceedings of the 27$^{\text{th}}$ Annual Meeting of the International Society for Magnetic Resonance in Medicine, Montreal, Canada (2019).

Franke, Vanessa; **Zimmermann, Ferdinand**; Magill, Arthur W.; Ladd, Mark E.; Bachert, Peter; Korzowski, Andreas. *Functional 31P Magnetic Resonance Spectroscopy of the Human Visual Cortex using Repeated Short-Term Stimulation at 7T* . In: Proceedings of the 27$^{\text{th}}$ Annual Meeting of the International Society for Magnetic Resonance in Medicine, Montreal, Canada (2019).

Boyd, Philip S.; Breitling, Johannes; **Zimmermann, Ferdinand**; Korzowski, Andreas; Zaiss, Moritz; Schuenke, Patrick; Weinfurter, Nina; Schlemmer, Heinz-Peter; Ladd, Mark E.; Bachert, Peter; Paech, Daniel; Goerke, Steffen. *Acquisition protocol for glucoCESL MRI in the human brain at 7T with reduced motion-induced artifacts.* In: Proceedings of the 27$^{\text{th}}$ Annual Meeting of the International Society for Magnetic Resonance in Medicine, Montreal, Canada (2019).

Zimmermann, Ferdinand; Korzowski, Andreas; Schuenke, Patrick; Breitling, Johannes; Zaiss, Moritz; Paech, Daniel; Ladd, Mark E.; Goerke, Steffen. *Fat corrected*

APT-CEST in the human breast. In: Proceedings of the 7th International Workshop on Chemical Exchange Saturation Transfer Imaging, Beijing, China (2018).

Meissner, Jan-Eric; Breitling, Johannes; **Zimmermann, Ferdinand**; Goerke, Steffen; Korzowski, Andreas; Zaiss, Moritz; Ladd, Mark E.; Bachert Peter. *FullHD CEST imaging in the human brain at 7T.* In: Proceedings of the 7th International Workshop on Chemical Exchange Saturation Transfer Imaging, Beijing, China (2018).

Zimmermann, Ferdinand; Korzowski, Andreas; Schuenke, Patrick; Breitling, Johannes; Ladd, Mark E.; Bachert, Peter; Goerke, Steffen. *A novel normalization to correct APT-CEST in the presence of fat.* In: Proceedings of the 26th Annual Meeting of the International Society for Magnetic Resonance in Medicine, Paris, France (2018).

Zimmermann, Ferdinand; Goerke, Steffen; Breitling, Johannes; Klopries, Kerstin; Windschuh, Johannes; Schlemmer, Heinz-Peter; Ladd, Mark E.; Paech, Daniel; Bachert, Peter. *Correction of fat artifacts for unbiased CEST-MRI of the human breast at 7T.* In: Proceedings of the 25th Annual Meeting of the International Society for Magnetic Resonance in Medicine, Honolulu, USA (2017).

Acknowledgments

An dieser Stelle möchte ich mich bei all denjenigen bedanken, die mich bei dieser Arbeit unterstützten.

Prof. Dr. Peter Bachert danke ich für die Möglichkeit, in seiner Arbeitsgruppe zu forschen. Vielen Dank für Ihr Vertrauen und Unterstützung während der ganzen Promotion, was es mir erlaubte, eigene Ideen umzusetzen.

Prof. Dr. Lothar Schad danke ich für die Bereitschaft zur Erstellung des Zweitgutachtens und interessante Gespräche in den Seminaren.

Prof. Dr. M. Ladd bin ich dankbar für die Ermöglichung der Promotion in seiner Abteilung und der Teilnahme an internationalen Konferenzen.

Steffen und Andi danke ich für die gute Betreuung der Arbeit und eure stete Hilfsbereitschaft! Ich habe viel von euch lernen können. Danke, Steffen, dass du damals auch die Weichen für den erfolgreichen Verlauf der Arbeit gestellt hast! Andi, dir danke ich für bereichernde Diskussionen und viel MR Praxis, die ich von dir lernen konnte.

Vielen Dank an Lisa Loi und Daniel Paech aus der Radiologie für die gute Zusammenarbeit und Patientinnenakquise.

Mein herzlicher Dank gebührt der gesamten Arbeitsgruppe! Danke an Jan, Sarah, Johannes, Boyd, Joe, Nam, Cornelius, Steffen, Andi, Vanessa, und auch ehemalige Mitglieder wie Patrick und Johnny. Mit euch macht's Spaß! Insbesondere danke ich für eure Unterstützung in den letzten Wochen und das Korrekturlesen. Vielen Dank an Jan und Johannes für viele konstruktive Gespräche. Danke Patrick für die Einführung ins Sequenzprogrammieren und die anfangs gemeinsame Programmierung der FancyGUI.

Thanks to Rachel High for proof reading! See you in Montreal :-)

Vielen Dank an Philipp Ehses (DZNE, Bonn) für die Bereitstellung der Matlab-toolbox für den Rohdaten-Import und adaptive-combine algorithm.

I enjoyed working with Karel Klika and am grateful for your support for many cell experiments performed on the spectrometer (which didn't make it into this thesis, unfortunately).

All den geduldigen Probandinnen, insbesondere V1a-k, V3a-f und V2a-d! Euer Mitmachen und Kooperation hat die Entwicklung der Methodik erheblich vorangebracht.

Der Akademischen Philharmonie Heidelberg e.V. und Jesko Sirvend bin ich dankbar für viele Jahre guter Musik, guten Zusammenhalt und Freundschaften. Das hat mir viel bedeutet.

Auf viele Freunde konnte ich auch abseits der Physik immer bauen. Danke an Julian, Daniela, Timmi, Macla, Torsten, Anna, Till, Martha, Conor, Elias, Martin, Oli, Chris, Cedi, Tilmi, ... Ihr seid großartig.

Bei meiner Familie und besonders bei meinen Geschwistern bedanke ich mich für die große Unterstützung während des gesamten Studiums und der Promotion. Lisa danke ich von ganzem Herzen. Schön, dass du stets an meiner Seite bist.

Explanation

I hereby assure, that I composed this work by myself and did not use any other than the listed resources.

Heidelberg, May 3rd 2019 .....

Ferdinand Zimmermann